Université de Strasbourg

Ecole Doctorale de Physique et Chimie-Physique

Thèse de Doctorat

présentée pour obtenir le grade de

Docteur en Sciences de l'Université de Strasbourg
(spécialité : Physique Nucléaire)

par

Christophe SAGE

Mesures des sections efficaces totale et (n,2n) sur ^{241}Am

Thèse soutenue le 27 novembre 2009, devant la commission d'examen :

P. DESSAGNE	Directeur de thèse
G. RUDOLF	Co-directeur de thèse
O. SEROT	Rapporteur
E. GONZALEZ	Rapporteur
A. J. M. PLOMPEN	Examinateur
F. GUNSING	Examinateur

Remerciements

Ce travail a été réalisé dans le cadre d'une collaboration entre l'Institute for Reference Materials and Measurements (IRMM) à Geel, l'Institut Pluridisciplinaire Hubert Curien (IPHC) à Strasbourg, ainsi que le Service de Physique Nucléaire (SPhN) de la Direction des Sciences de la Matière (DSM) et le Laboratoire d'Etudes Physiques (LEPh) de la Direction de l'Energie Nucléaire (DEN) du Commissariat à l'Energie Atomique (CEA) basés respectivement à Saclay et à Cadarache.

Je tiens donc à remercier tout d'abord les artisans de cette collaboration : mes premiers interlocuteurs à Cadarache, Olivier Bouland et Gilles Noguère, mes directeurs de thèse Gérard Rudolf et Philippe Dessagne, ainsi que mes deux responsables de Geel et Saclay, Arjan Plompen et Frank Gunsing. Un grand merci pour m'avoir suivi au cours de cette thèse, et pour l'avoir portée tout le long, tant par les nombreux conseils scientifiques que par les toutes aussi nombreuses signatures administratives.

Je remercie Peter Rullhusen et Michel Garçon pour leur accueil au sein de leurs laboratoires respectifs de l'IRMM et du SPhN.

J'exprime ma gratitude à tous ceux qui ont suivi et éclairé mon travail de leurs conseils des plus précieux. Merci tout d'abord à Valentina Semkova pour avoir partagé toute sa science sur les mesures d'activation avec une gentillesse incomparable, et merci à Ricardo Jaime pour leur mise en place sans faille. Merci à Peter Siegler, Stefan Kopecky et Peter Schillebeeckx pour leur parfaite initiation aux mesures de transmission et de capture. Enfin, un grand merci à toute l'équipe chargée du fonctionnement de GELINA et du Van de Graaff.

J'ai une pensée pour tous ceux qui ont rendu mon séjour en Belgique et à Saclay agréables. Merci à mes collègues thésards Sofie, Evert, Ivo et Carlos pour les bons moments passés en salle café ou autour d'une bière. Mulţumesc à la délégation roumaine de l'IRMM, Dana, Catalin, Andu, Cristian et Mihai, pour avoir prolongé les bons moments au-delà de l'enceinte du laboratoire. Un merci

Résumé

Des mesures de sections efficaces neutroniques des réactions ^{241}Am(n,2n)^{240}Am, ^{241}Am(n,tot) et ^{241}Am(n,γ) ont été réalisées à l'IRMM (Institute for Reference Materials and Measurements) à Geel, en Belgique, dans le cadre d'une collaboration entre ce laboratoire de la Commission Européenne et des laboratoires français du CEA et du CNRS. Des échantillons d'oxyde d'américium spécialement dédiés à ces mesures furent fabriqués au sein de l'ITU (Institute for TransUranium elements) à Karlsruhe à partir de matière première fournie par le CEA Marcoule. Concernant la mesure de la réaction (n,2n), les irradiations eurent lieu auprès de l'accélérateur Van de Graaff de l'IRMM en plusieurs sessions de février 2007 à mars 2008. Cet accélérateur fournit un faisceau de neutrons quasi-monoénergétiques à des énergies comprises entre 8.4 et 20.6 MeV via les réactions D(d,n)^{3}He et T(d,n)^{4}He. La section efficace fut déterminée relativement à celle de la réaction standard ^{27}Al(n,α)^{24}Na. Les résultats détaillés dans cette thèse présentent la première mesure expérimentale de cette section efficace au-delà de 15 MeV, ainsi que trois autres énergies en bon accord avec les expériences précédentes. Les mesures de section efficaces totale et de capture furent effectuées au sein de la source blanche de neutrons GELINA de l'IRMM. Ces mesures, effectuées entre mars 2007 et décembre 2008, se concentrent principalement sur les deux premières résonances de la section efficace de l'^{241}Am aux énergies 0.3 et 0.57 eV. Les résultats des mesures de transmission confirment les tendances des mesures intégrales vers une augmentation de la section efficace. Les mesures de capture furent effectuées dans la continuité de celles de transmission, mais leur analyse n'est pas incluse dans ce travail de thèse.

Contexte de l'étude

Ce travail de thèse s'inscrit dans le cadre de la transmutation des actinides mineurs qui dominent la radiotoxicité des déchets actuels au-delà de quelques centaines d'années. Pour ces noyaux lourds, leur transmutation passe par une incinération au moyen des réactions de fission ou de capture dans un réacteur de type innovant de par la composition de son combustible. La conception d'un tel réacteur et son

rendement reposent sur des calculs de neutronique complexes qui font appel aux bases de données nucléaires. Pour l'isotope d'américium étudié dans ce travail, ces données nucléaires sont encore mal connues, ou présentent d'importantes disparités. C'est pourquoi une campagne de mesures, à laquelle est rattachée cette thèse, fut lancée à travers une collaboration de laboratoires européens.

Mesure par activation de la section efficace de la réaction ^{241}Am(n,2n)^{240}Am

La mesure expérimentale directe des sections efficaces des réactions types (n,xn) est une tâche ardue de par la difficile différentiation entre les neutrons incidents et les neutrons émis par le noyau formé lors de l'interaction. L'^{241}Am est un des seuls actinides mineurs pour lequel la technique d'activation peut être utilisée. Le produit de la réaction, l'^{240}Am, a en effet une demi-vie de l'ordre de 50 h et émet deux intenses raies gamma, à 888.85 et 987.79 keV, facilement identifiables.

Cette mesure fut réalisée en 4 sessions d'une semaine chacune environ. Les temps d'irradiation, de l'ordre de deux jours pour correspondre à la demi-vie du produit de la réaction, ont permis d'effectuer trois mesures à différentes énergies par semaine. Lors de la première, une cible gazeuse de deutérium fut utilisée pour obtenir des neutrons aux énergies de 8.8 et 9.4 MeV, qui constituent les deux points à basse énergie de la figure 1. Les trois autres sessions furent dédiées aux points de plus haute énergie, avec des neutrons entre 13.3 et 20.6 MeV obtenus par la réaction d'un faisceau de deutérons sur une cible solide de Ti/T.

Le flux de neutrons en fonction de l'angle de détection et de l'énergie des deutérons fut déterminé dans les deux cas à l'aide du programme Energyset développé spécialement à cet effet à l'IRMM et basé sur les cinétiques des réactions de production des neutrons. Un long compteur BF$_3$ fut utilisé pour enregistrer le profil en temps du faisceau de neutrons au cours des deux jours d'irradiation afin de calculer les corrections induites par la fluctuation de l'intensité du faisceau. De plus, afin d'estimer la distribution en énergie des neutrons, différentes réactions de dosimétrie comme ^{115}In(n,n')^{115}In, ^{58}Ni(n,p)^{58}Co ou ^{27}Al(n,α)^{24}Na furent utilisées.

Directement après l'irradiation, l'activité induite de l'échantillon fut mesurée hors-ligne avec un détecteur germanium. Un blindage spécial fut placé autour du détecteur afin de s'affranchir de la forte activité naturelle de l'^{241}Am, et tout spécialement de l'intense rayonnement gamma de 60 keV. Ce dispositif permit de réduire le temps mort de détection à environ 10%. L'analyse des spectres obtenus fut réalisée à l'aide du logiciel Genie2000, et l'efficacité du système de détection fut déterminée par une simulation Monte Carlo à l'aide du code MCNP5, combiné

à une vérification expérimentale avec diverses sources standard de calibration.

Les sections efficaces furent calculées via la formule classique d'activation appliquée à l'irradiation de l'échantillon d'américium et aux feuilles d'aluminium, ce qui peut s'écrire dans notre cas :

$$\sigma_{\text{Am}} = \sigma_{\text{Al}} \frac{S_{\text{Am}}}{S_{\text{Al}}} \frac{\left[I \epsilon f_\Sigma f_r n \Phi_0\right]_{\text{Al}}}{\left[I \epsilon f_\Sigma f_r n \Phi_0\right]_{\text{Am}}} \cdot \prod_k \frac{C_{\text{k,Am}}}{C_{\text{k,Al}}}.$$

avec σ_{Am} et σ_{Al} les sections efficaces des réactions ^{241}Am(n,2n) et ^{27}Al(n,α), S_{Am} et S_{Al} les taux de comptage pour les deux réactions, I les probabilités d'émission, ϵ les efficacités absolues du détecteur, f_Σ et f_r les facteurs en temps prenant en compte la décroissance radioactive du produit de réaction aux temps de mesure, n les nombres de noyaux cibles, Φ_0 le flux de neutron et C_k les différents facteurs de correction.

Les corrections liées au processus de mesure de l'activité (absorption des gammas dans l'échantillon, gammas en coïncidence, etc.) furent incluses dans les simulations estimant l'efficacité du détecteur HPGe. Concernant les corrections relatives au processus d'irradiation, deux principaux facteurs de correction sont à prendre en compte. Tout d'abord, l'impact de la fluctuation du faisceau de neutrons au cours des deux jours d'irradiation est évalué en mesurant le spectre en temps du faisceau à l'aide d'un compteur BF$_3$. Si l'on divise le temps total d'irradiation t_r en m intervalles Δt, la contribution d'un de ces intervalles sera proportionnelle à $\Phi_i(1 - e^{-\lambda \Delta t})$, et la décroissance correspondante proportionnelle à $e^{-\lambda(m-i)\Delta t}$. Le facteur de correction C_{flux} est alors calculé comme suit :

$$C_{\text{flux}} = \frac{\bar{\Phi}(1 - e^{-\lambda t_r})}{\sum_{i=1}^m \Phi_i(1 - e^{-\lambda \Delta t})e^{-\lambda(m-i)\Delta t}}$$

avec $\bar{\Phi} = \sum \Phi_i/m$ le flux moyen durant l'irradiation.

Un second facteur de correction important concerne la contribution des neutrons de basse énergie provenant de réactions parasites. Pour cette estimation, un spectre en temps de vol fut mesuré au préalable, et l'intensité de chaque pic de basse énergie fut évaluée à l'aide de réactions de moniteur ayant différents seuils : ^{27}Al(n,p)^{27}Mg, ^{56}Fe(n,p)^{56}Mn, ^{115}In(n,n')^{115m}In, ^{27}Al(n,α)^{24}Na, ^{93}Nb(n,2n)^{92m}Nb et ^{58}Ni(n,p)$^{58m+g}$Co. Le spectre en temps de vol est ainsi divisé en plusieurs groupes dont les intensités relatives sont ajustées selon les activités induites dans les feuilles de moniteur selon la formule

$$C_{\text{low}} = 1 - \frac{\int_0^{E_c} \Phi(E)\sigma(E)dE}{\int_0^\infty \Phi(E)\sigma(E)dE}.$$

Energie	σ_{Am}	Inc.	Matrice de corrélation (x100)								
(MeV)	(mb)	(%)									
8.34(15)	96.8	6.5	100								
9.15(15)	162.9	5.7	35	100							
13.33(15)	241.8	4.6	37	42	100						
16.10(15)	152.4	4.6	38	43	53	100					
17.16 (3)	116.1	4.4	40	45	57	58	100				
17.90(10)	105.7	4.4	41	45	57	59	84	100			
19.36(15)	89.5	8.2	21	24	30	31	39	39	100		
19.95 (7)	102.1	5.8	30	34	44	45	58	59	51	100	
20.61 (4)	77.9	8.8	20	22	29	30	40	42	39	65	100

Table 1: Sections efficaces de la réaction ^{241}Am(n,2n)^{240}Am mesurées au cours de ce travail, avec leurs incertitudes totales et les degrés de corrélation entre les différents point d'énergie.

avec E_c une énergie de cutoff définie arbitrairement pour chaque réaction en dessous de l'énergie du pic monoénergétique.

Le tableau 1 donne les résultats obtenus pour cette mesure de section efficace de la réaction ^{241}Am(n,2n)^{240}Am avec les incertitudes et leurs corrélations respectives. Comme le montre la figure 1, les trois points pouvant être comparés à des mesures précédentes (respectivement à 8.3, 9.2 et 13.3 MeV) semblent en bon accord avec ces dernières, si l'on met à part les résultats de Perdikakis *et al* (notés ATH 2006). Nos points à plus haute énergie suivent la tendance générale donnée par les évaluations calculées précédemment à nos mesures. Seule la nouvelle évaluation effectuée à l'aide du code TALYS prend ici en compte nos résultats expérimentaux pour les inclure dans ses paramètres de calculs.

Mesure de la section efficace de la réaction ^{241}Am(n,tot)

La mesure de la section efficace de la réaction ^{241}Am(n,tot) se fait par transmission, dont le principe de base est relativement simple: il suffit de mesurer le flux de neutrons transmis par l'échantillon. Pour ce faire, un détecteur de neutrons en verre de lithium est placé à la suite de l'échantillon d'américium sur la base de vol du faisceau de neutrons. Une succession de mesures avec l'échantillon dans/hors du faisceau est alors réalisée. Le rapport de ces deux flux, appelé coefficient de transmission, est directement proportionnel à la section efficace totale:

$$T(E) = N_T \frac{\phi_{in}(E)}{\phi_{out}(E)} \equiv e^{-n\sigma_t(E)}$$
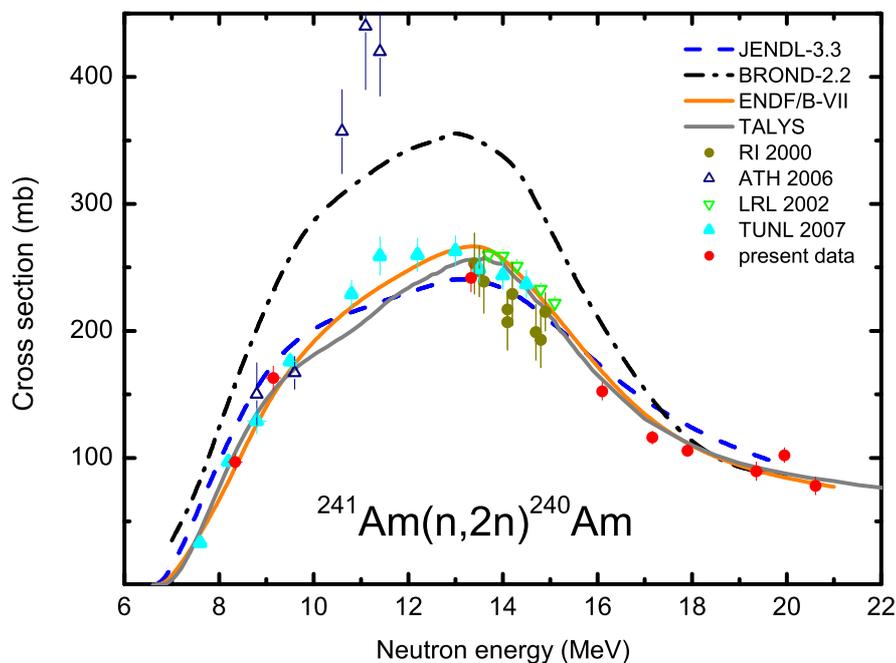
Figure 1: Mesures expérimentales de la section efficace de la réaction ^{241}Am(n,2n) obtenues à l'IRMM et comparées aux mesures et évaluations précédentes.

avec N_T le facteur de normalisation.

Les mesures de transmission furent effectuées sur la base de vol numéro 2 de GELINA, dont la longueur est de 26.45 m. Le diamètre du faisceau de neutrons était d'environ 1.5 cm, obtenu à l'aide d'une combinaison de collimateurs en cuivre et nickel. L'échantillon fut placé à environ 10 m à mi-chemin entre l'origine du faisceau et le système de détection. Plusieurs filtres furent placés sur le parcours du faisceau afin de réduire l'intensité du flash gamma émis lors de la production des neutrons et d'estimer le bruit de fond à l'aide de la technique des résonances noires.

Pour la détection des neutrons transmis, un scintillateur cylindrique en verre de lithium de 0.5 pouce d'épaisseur et 4 pouce de diamètre fut utilisé, couplé à deux tubes photomultiplicateurs placés de par et d'autre. Le temps de vol des neutrons, donnant leurs énergies respectives, était également enregistré. Afin de réduire l'impact de la variation du flux de neutrons, les mesures furent réalisées par cycles d'une vingtaine de minutes.

Le but de cette mesure de transmission était d'améliorer les données relatives aux deux premières résonances de la section efficace (respectivement 0.3 et 0.57 eV), celles-ci relevant de mesures assez anciennes et montrant de larges disparités (cf figure 2). Pour ce faire, un nouveau système d'acquisition fut installé, basé sur une nouvelle électronique numérique rapide, et dont les performances sont comparées dans le travail de thèse. Ce nouveau système enregistre tout évènement se produisant dans le détecteur sans aucune discrimination en ligne, et permet donc une meilleure flexibilité lors de l'analyse des données par une meilleure détermination du bruit de fond.
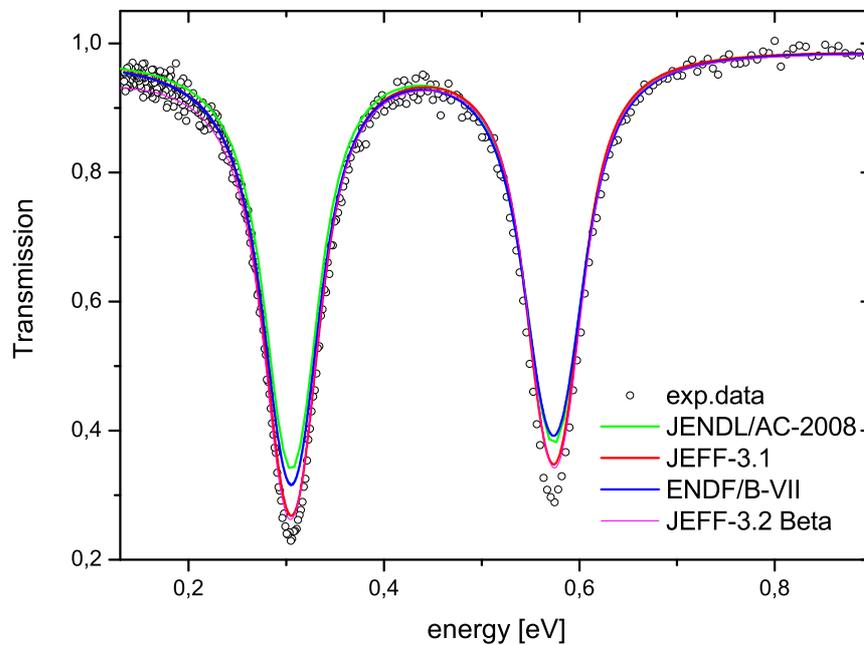
Figure 2: Mesures expérimentales de la section efficace de la réaction ^{241}Am(n,tot) obtenues à l'IRMM et comparées aux évaluations précédentes.

Le facteur de transmission de l'échantillon fut déterminé et analysé pour en déduire les sections efficaces à l'aide du code REFIT spécialement dédié à l'analyse des formes de résonance. La figure 2 montre les résultats d'une telle analyse avec une comparaison des transmissions déterminées avec les paramètres de résonance donnés dans les différentes librairies de données nucléaires existantes (ENDF, JEFF et JENDL). Ces évaluations semblent toutes sous-estimer

la section efficace de la réaction ^{241}Am(n,tot) au niveau du bas des résonances. Cependant, les résultats ne pourront être finalisés qu'après une analyse simultanée avec les mesures de capture.

Simulation des nouveaux détecteurs C_6D_6 pour les mesures de capture

Un nouvel assemblage de scintillateurs C_6D_6 fut mis au point à l'IRMM, chaque détecteur ayant une nouvelle géométrie en forme de pyramide tronquée dont le but est d'accroître significativement leur efficacité aux gammas sans pour autant en augmenter la sensitivité aux neutrons.

Le principe de la mesure de capture est en effet basé sur la détection des rayons gammas émis durant l'interaction du faisceau de neutrons avec l'échantillon. Le taux de capture $Y(E)$, qui est défini comme le nombre d'évènements de capture $N_c(E)$ par neutron incident $\Phi(E)$, s'écrit alors:

$$Y(E) = N_Y \frac{N_c(E)}{\Phi(E)} \equiv (1 - e^{-n\sigma_t})\mu \frac{\sigma_\gamma(E)}{\sigma_t(E)}$$

avec $\sigma_\gamma(E)$ la section efficace de capture, N_Y le facteur de normalisation et μ la correction due aux diffusions multiples. En pratique, $N_c(E)$ et $\Phi(E)$ sont mesurés simultanément à l'aide respectivement de scintillateurs C_6D_6 et d'une chambre de bore.

Pour étudier les caractéristiques de ces nouveaux détecteurs, leur géométrie fut modélisée avec une grande précision à l'aide du programme MCNP5. L'ensemble scintillateur/photomultiplicateur fur ainsi décrit très précisément à l'aide des données fournies par le constructeur des PMs. Le tally F8 du code MCNP5 fut utilisé pour suivre les interactions des photons et des électrons le long du parcours du photon dans le scintillateur. L'intégrale de la quantité d'énergie déposée normalisée à la quantité d'énergie incidente définit l'efficacité gamma totale du détecteur montrée sur les courbes de gauche de la figure 3, illustrant la comparaison des performances des anciens et des nouveaux détecteurs.

Concernant la sensitivité aux neutrons, le même tally fut utilisé, pour suivre cette fois les interactions des photons et des électrons sur le chemin des neutrons. Plusieurs sources de neutrons monoénergétiques furent simulées sur un intervalle allant de 0.1 eV à 1 MeV. Chaque réponse des détecteurs fut intégrée puis normalisée à la probabilité de détection d'un gamma de 4 MeV. Le résultat est montré sur le graphique de droite de la figure 3, où sont comparées les sensitivités aux neutrons pour un seul détecteur au sein d'un assemblement de 4 détecteurs, à la fois pour le nouveau et l'ancien design. Cette dernière restant dans le même ordre
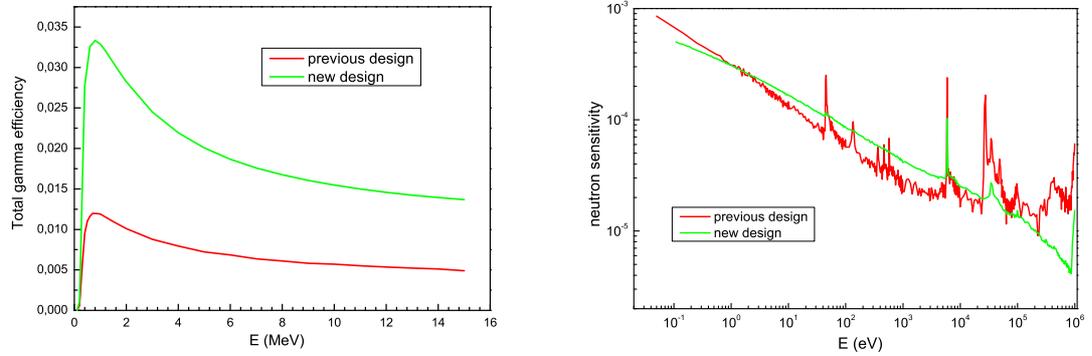
Figure 3: Simulation avec le code MCNP des caractéristiques des détecteurs C_6D_6.

de grandeur, nous constatons bien une augmentation d'un facteur 4 de l'efficacité aux gammas sans augmentation notable de la sensitivité aux neutrons pour ces nouveaux détecteurs C_6D_6.

Abstract

Several measurements of neutron induced reaction cross sections on ^{241}Am have been performed at the JRC-IRMM in Geel, Belgium, in the frame of a collaboration between the EC Joint Research Centres IRMM and ITU and French laboratories from CNRS and CEA. Raw material coming from the Atalante facility of CEA Marcoule has been transformed by JRC-ITU Karlsruhe into suitable ^{241}AmO$_2$ samples embedded in Al$_2$O$_3$ and Y$_2$O$_3$ matrices. They were specifically designed for activation and Time-Of-Flight measurements.

The irradiations for the ^{241}Am(n,2n)^{240}Am reaction cross section measurement were carried out at the 7 MV Van de Graaff accelerator using the activation technique. The measurements were performed in four sessions, using quasi mono-energetic neutrons with energies ranging from 8 to 21 MeV produced via the D(d,n)^{3}He and the T(d,n)^{4}He reactions. The ^{241}Am(n,2n) reaction cross section was determined relative to the ^{27}Al(n,α)^{24}Na standard cross section and was investigated for the first time above 15 MeV. The induced activity was measured off-line after the irradiation by standard gamma-ray spectrometry using a high purity germanium detector. A special effort was made for the estimation of the uncertainties and the correlations between our experimental points, with a detailed identification of the possible correlation sources. Our experimental results were used to parameterize new theoretical calculations of the (n,2n) cross section with the TALYS code.

A different sample of the same isotope ^{241}Am has been measured in transmission and capture experiments in the resolved resonance region at the neutron Time-Of-Flight facility GELINA. The transmission measurement was performed in two campaigns, the second one after a recent upgrade of the whole data acquisition system. The neutron flux was measured using a Li-glass scintillator via the ^{6}Li(n,t)^{4}He reaction. The performances of the new acquisition system, especially concerning its better flexibility for the off-line data reduction, were investigated. A preliminary analysis of the resonance parameters tends to confirm the recent evaluation to a higher value for the cross section at the bottom of the resonances.

The capture measurement was achieved following the transmission one and using the same sample, but its data reduction and analysis are not part of this

work. A new design of C_6D_6 detectors for capture based on a truncated 5-sided pyramid shape has been studied, especially concerning its total gamma efficiency and its neutron sensitivity. The performances were compared with the ones of the previous detectors, and it was shown that their total gamma efficiency was increased by a factor 4 without any notable increase in the neutron sensitivity.

Contents

List of Tables

List of Figures

List of abbreviations

ABWR	Advanced Boiling Water Reactor
ADC	Analogue to Digital Converter
ADS	Accelerator Driven System
AGR	Advanced Gas Reactor
AGS	Analysis of Geel Spectra
APWR	Advanced Pressurized Water Reactor
ATR	Advanced Thermal Reactor
BWR	Boiling Water Reactor
CANDU	CANada Deuterium Uranium
CEA	Commissariat à l'Energie Atomique
CENDL	Chinese Evaluated Nuclear Data Library
CFD	Constant Fraction Discriminator
CM	Central Monitor
CNRS	Centre National de la Recherche Scientifique
CSISRS	Cross Section Information Storage and Retrieval System
EC-JRC	European Commission Joint Research Center
ENDF	Evaluated Nuclear Data File
FBR	Fast Breeder Reactor
FGM	Free Gas Model
FP	Fission Products
FTD	Fast Time Coder
GELINA	GEel LINear Accelerator
GFR	Gas Fast Reactor
GIF	Generation-IV International Forum
GULP	General Utility Lattice Program
HCM	Harmonic Crystal Model
HPGe	High Purity Germanium detector
HTR	High Temperature Reactor
HWLWR	Heavy Water Light Water Reactor
IRMM	Institute for Reference Materials and Measurements
ITU	Institute for TransUranium elements

JEFF	Joint Evaluated Fission and Fusion library
JENDL	Japanese Evaluated Nuclear Data Library
LANL	Los Alamos National Laboratory
LFR	Lead Fast Reactor
LMR	Liquid Metal Reactor
LWGR	Light Water Graphite Reactor
MA	Minor Actinides
MCNP	Monte-Carlo N-Particle
MGUNGG	MaGnox Uranium Natural Gas Graphite
MLBW	Multi-Level Breit Wigner
MMPM	Modular Multi-Parameter Multiplexer
MOX	Mixed OXide
MSR	Molten Salt Reactor
MSRE	Molten Salt Reactor Experiment
NEA	Nuclear Energy Agency
NSC	Nuclear Science Committee
ORELA	Oak Ridge Electron Linear Accelerator
PHWR	Pressurized Heavy Water Reactor
PHWT	Pulse Height Weighting Technique
PM	PhotoMultiplicator
PUREX	Pu-U Refining by EXtraction
PWR	Pressurized Water Reactor
RBMK	Reaktor Bolchoi Mochtchnosti Kanalni
RRR	Resolved Resonance Region
SCWR	Super Critical Water Reactor
SFR	Sodium Fast Reactor
SLBW	Single Level Breit Wigner
SRIM	Stopping and Range of Ions in Matter
TOF	Time-Of-Flight
URR	Unresolved Resonance Region
VHTR	Very High Temperature Reactor
WPEC	Working Party on international Evaluation Cooperation
WWER	Water Water Reactor

Introduction

During this last decade, growing needs in the world energy consumption renewed the interest in nuclear energy exploitation. Yet, any project concerning an increase of nuclear energy production requires the problems from todays existing technologies to be solved. The fuel cycle currently in use, based on the fission of ^{235}U, can actually ensure the production only for a limited time, due to our limited uranium resources. Moreover, the problem of radioactive waste, and in particular the main issue about the production of long-lived radioactive isotopes, is still lacking a satisfactory solution in view of environment preservation and acceptance by society.

If nuclear energy is going to play a major role in the worlds energy future, these issues must be faced. The international community is now considering innovative nuclear systems for the future, with choices based on crucial parameters such as waste minimisation, safety, sustainability, economy and non-proliferation. The study and design of these systems rely on advances in several fields, among which new materials for fuel, fuel processing and recycling, and new developments in the field of reactors and basic nuclear physics.

In this context, the role of nuclear data is essential, since a very good knowledge of the involved nuclear reactions is the compulsory first step for the study of innovative new concepts of reactors. Most of the useful nuclear data are available in different existing evaluated libraries and experimental databases, but the majority of them lacks the required accuracy for the precise study of the new systems characteristics, and are limited in energy range.

Several nuclear facilities in Europe are dedicated to the measurements of accurate nuclear data, such as the Institute for Reference Materials and Measurements (IRMM) in Geel, Belgium. The work presented here concerns the (n,2n) and total neutron cross section measurements on ^{241}Am achieved at IRMM. This isotope is of great interest since it figures among the main contributors to the spent fuel radiotoxicity. The accurate knowledge of its neutron characteristics is crucial, for instance concerning the study of the new reactor concepts running with an innovative fuel containing an important quantity of minor actinides.

The first chapter of this work presents the context of nuclear energy production, as well as the special issue of nuclear waste and the options under study for

their management. The important role of nuclear data is then detailed, focusing on the status of americium data and the scope of this work.

In the second chapter, the basic theory required for the understanding of the measurement is explained. A brief presentation of neutron induced nuclear reactions is presented, as well as their theoretical description with the R-matrix formalism. The important notions of compound nucleus, cross sections and resonances are detailed.

The third chapter of this work presents our experimental measurement of the ^{241}Am(n,2n)^{240}Am. The principle of this measurement is first explained, describing the activation technique we employed. It focuses then on the experimental conditions, from the sample description to the irradiation setup and the induced activity measurement. The analysis of the data and the final calculations of the cross sections are presented in chapter four, along with a detailed explanation of the uncertainty estimations and the correlations between our energy points.

The ^{241}Am(n,tot) reaction cross section measurement is presented in chapter five, starting in the same way by the presentation of the measurement principle. The experiment itself is then detailed, with a description of our neutron source GELINA, the experimental setup and the detectors we employed. The data reduction and a preliminary analysis of the results with the REFIT code are presented in chapter six.

The last chapter concerns a description of the simulation of a new design of C_6D_6 detectors that are employed for capture cross sections measurements at IRMM. The measurement of the ^{241}Am(n,γ) reaction cross section was achieved following the transmission measurement, but its description and analysis are not part of this work.

Chapter 1

Context and motivations for ^{241}Am neutron cross section measurements

Nuclear energy is about to play an important role to secure energy supply in the future. This can be seen from the significant activity in the nuclear sector during these past few years, with some countries beginning the construction of new reactors or announcing plans to do so, and others deciding to introduce nuclear energy or to build enrichment and reprocessing capacity for the first time in decades [1].

In the middle of 2009, there were 436 nuclear units in operation. 52 units were under construction and 5 in long term shutdown [2]. The reasons for the current nuclear energy revival are mainly because it provides an effective answer to the problem of CO_2 emission and to the requirement of a sustainable development, in particular in view of the foreseen growth in energy demand. We will now briefly review the different possible ways for energy production, with their advantages and limits, before giving more details on the nuclear one.

1.1   Different ways for energy production

Most of the world's energy is produced by combustion of fossil fuels (oil, coal and natural gas). Along with their important greenhouse gas emission, another issue of such energy sources is the increasing cost due to the diminution of the available reserves. According to [3], the present reserves of oil and gas allow their use for 40 and 65 years respectively, with a longer deadline to 150 years concerning coal.

Another possibility for energy production concerns the renewable sources and their relative cleanness, that can be added to their certain advantage of sustainability. Yet this point needs some relativization. Concerning photovoltaic cells

for instance, their production gives some chemical waste that has a strong impact on the environment. There are mainly two types of renewable sources: mechanical (wind and water power) and radiant (solar and geothermal). Although such sources are gaining importance, their total part in energy production is unlikely to become predominant compared to the other energy sources, at least in the near future, mainly because of their extremely low energy efficiency. Moreover, the intermittent and unpredictable characteristics inherent to these energies raise the issue of storing.

Thus fossil fuels won't be able to sustain the world's increasing energy demand, and renewable sources don't represent a full scale replacement in the medium term either. Consequently, it seems probable that the role of nuclear energy will get even more important. This future will be based on the consolidation and evolution of present reactor concepts, but also on the definition of new requirements for both future reactors and their associated fuel cycles. The key issues for nuclear energy development are then economics, safety, supplies of uranium, waste minimization and proliferation resistance. The current once through cycle is not sustainable, and the development of close fuel cycles in innovative reactors has to figure among the main research topics.

Different research lines are considered to face these issues. Concerning the radioactive waste produced by the reactors currently in function, safe geological disposal is under investigation along with transmutation as complementary solution. Other studies concern a fuel cycle based on thorium and producing much less radiotoxic actinides as a promising alternative. On the other hand, the international community has concentrated on the development of six future generation nuclear reactors, namely Generation IV reactors, to be operational by 2050 [4].

The next paragraphs will give more details on the principle of existing reactors and all the different research lines mentioned above concerning the nuclear wastes issue, the thorium cycle and new concepts of reactors. This research work relies on an increased role of reliable and well validated nuclear data, both at the stage of feasibility studies and for more detailed design assessments, which constitutes the main motivations of this PhD work.

1.2   Nuclear energy and nuclear reactors

Nuclear energy is produced via the fission of an atomic nucleus. The energy released by this reaction is then transformed into heat, which will then be extracted from the reactor core via thermal exchange and transferred to turbines, where it is finally converted into electricity with alternators.

Current conventional reactors are based on the fission process of ^{235}U and ^{239}Pu. The isotope ^{235}U is indeed one of the most interesting concerning fission, since it is the only one naturally fissile. The fertile isotope ^{238}U, on the other hand, becomes the fissile ^{239}Pu after a neutron capture followed by two β-decays:

$$^{238}_{92}\text{U} + n \longrightarrow\ ^{239}_{92}\text{U} \xrightarrow{\beta^-(23min)}\ ^{239}_{93}\text{Np} \xrightarrow{\beta^-(2.4d)}\ ^{239}_{94}\text{Pu} \tag{1.1}$$
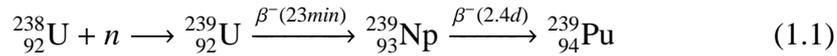
^{235}U represents 0.7% of natural uranium, and ^{238}U the 99.3% remaining. Enriched natural uranium is thus usually used, with a proportion of about 3% of ^{235}U, for a purpose of neutron economy.

The working principle of the reactor is the following: fissile fuel is placed inside the core together with some radioactive material, such as an americium-beryllium source for instance, for the reaction initiation. A flux of neutrons coming from this source will then create some fission reactions. Those last ones are characterized by the emission of fission fragments and a new generation of neutrons that will lead to other fissions. The neutronic performances of a fissile nucleus are evaluated with the parameter η corresponding to the number of fission neutrons per neutron absorbed in the fuel. It is defined by the formula

$$\eta = \frac{\nu}{1 + \alpha} \tag{1.2}$$

with ν the average number of neutrons emitted by fission and

$$\alpha(E_n) = \frac{\sigma_\gamma(E_n)}{\sigma_f(E_n)} \tag{1.3}$$

the ratio between the capture and fission cross sections.

Another important parameter concerning the control of the chain reactions in the reactor is the number of delayed neutrons. These neutrons are emitted by the fission fragments with a large time distribution after the fission occurred (centered typically around 12.5 s). Figure 1.1 shows the typical neutron balance of such a mechanism.

For a sustainable chain reaction, at least one of the neutrons produced in the fission event must survive in order to produce another fission. This is described by the multiplication factor k, which corresponds to the ratio of the number of fissions for one generation over the number of fissions from the previous generation. The steady state, named *criticality*, will then happen for $k = 1$, which implies a constant neutron population. The two other possible states are the *subcriticality* for $k < 1$, and *supercriticality* for $k > 1$; the normal working state of the reactor corresponding obviously to $k = 1$.
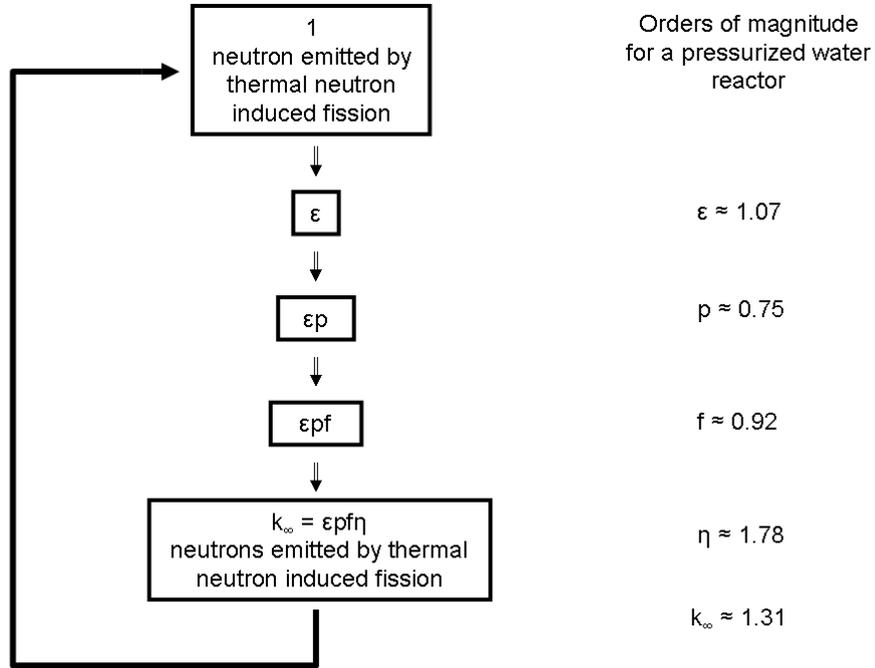
Figure 1.1: Neutron cycle in a thermal reactor and classic four-factor formula (without leaks). Orders of magnitude for a pressurized water reactor [5].

This factor is usually described via the four-factor formula:

$$k = \eta f \epsilon p \tag{1.4}$$

with f the thermal utilization factor corresponding to the probability for a neutron to get absorbed in the fuel material, ϵ the fast fission factor, which is the ratio between the total number of fission neutrons over the number of fission neutrons from thermal fissions, and p the resonance escape probability corresponding to the probability for a neutron not to be captured during the slowing down process.

This formula describes the simplified case of an infinite medium, where neutrons cannot leak out of the system and thus the multiplication factor becomes the infinite multiplication factor $k = k_\infty$. For the practical cases of finite reactors, we define the effective neutron multiplication factor $k_{eff} = k_\infty P_{NL}$, with P_{NL} the non-leakage probability.

The most favorable energy range for fission is the thermal one: at 25 meV the cross section ratio between the fission of ^{235}U and the capture of ^{238}U is about 200. This is the working energy range of the so-called thermal reactors, where the

neutron energy is reduced from the MeV (in which they are produced by fission events) to the thermal region by moderators.

There are currently several types of reactors in function worldwide. The differences between them are at the level of the fuel, the type of moderator for the neutron slowing down and the thermal exchangers for the heat transfer. Table 1.1 presents these different nuclear reactor types in activity in the world.

Table 1.1: Main characteristics of current reactor types [6]. (cf. the complete list of abbreviations)

Reactor type groups	type	coolant	moderator	fuel
gas-graphite	AGR MGUNGG HTR	CO_2 CO_2 He	graphite	enriched UO_2 natural U UO_2, UC_2, ThO_2
heavy water	PHWR	pressurized D_2O	D_2O	natural or enriched UO_2
light water	BWR (ABWR) PWR (APWR) WWER	boiling H_2O pressurized H_2O pressurized H_2O	H_2O	enriched UO_2 or enriched UO_2 and MOX
fast reactor	FBR	sodium		enriched UO_2--PuO_2
water-graphite	RBMK (LWGR)	boiling H_2O	graphite	enriched UO_2
light water-heavy water	HWLWR (ATR)	boiling H_2O	D_2O	enriched UO_2-PuO_2

The majority of industrial reactors in the world use pressurized light water (Pressurized Water Reactor PWR), both as coolant and neutron moderator. In the past, some reactors were also using boiling light water (Boiling Water Reactor BWR) instead of pressurized one, but this type of reactor is not built anymore, and only a few of them still remain in activity. The second major type of reactors is the one using pressurized heavy water (PHWR) as coolant and moderator. The other types of reactors are the Advanced Gas Reactor (AGR), where the coolant is CO_2 with a graphite moderator, the High Temperature Reactor (HTR), cooled with helium and also with a graphite moderator, and the Liquid Metal Reactor (LMR), which is a fast reactor cooled with liquid sodium.

1.3 The issue of nuclear waste

1.3.1 Nuclear waste classification

Radioactive waste is mainly coming from the production of electricity by means of nuclear energy (operating and decommissioning of nuclear power plants), but also from the use of radioactive sources in medicine, agriculture and industry. These include filters, resins, protective equipment (clothing, gloves, etc.), paper, activated concrete, residues from the processing of waste water in nuclear power plants and also decommissioning waste that has been in contact with radioactive substances.

The classification of all these kinds of waste is mainly based on two parameters, as is shown in table 1.2:

the activity: it is measured in Becquerel (1 Bq=1 disintegration per second) but is expressed in terms of mass activity (A_m in Bq/g) for the classification.

the half-life: corresponding to the decrease of activity with time.

Table 1.2: The 3 categories of radioactive waste in France.

	Low level $100 < A_m < 10^5$	Medium level $10^5 < A_m < 10^8$	High level $A_m > 10^8$
Short half-life (< 30 y)	A	A	C
Long half-life (> 30 y)	B	B	C

Table 1.3 shows a summary of the nuclear waste classification adopted in France, from their origin to their conditioning, depending on their category as defined in table 1.2.

- Category A waste: this is waste with a short half-life (< 30 y) and low to medium activity. They are generated from hospitals and industry, as well as the nuclear fuel cycle. It comprises paper, rags, tools, clothing, filters, etc., which contain small amounts of mostly short-lived radioactivity.

- Category B waste: this is waste with a long half-life (> 30 y) and low to medium activity. They include resins, chemical sludge and metal reactor fuel cladding, as well as contaminated materials from reactor decommissioning. They can be solidified in concrete or bitumen for disposal.

- Category C waste: this is high activity waste with both short and long half-lives. They are fission products and transuranic elements generated in the reactor core. They are thus highly radioactive and often thermally hot. They account for over 95% of the total radioactivity produced in the process of nuclear electricity production, though only 0.2% in volume.

- Very Low Activity waste: this is waste with a mass activity lower than 100 Bq/g. They are mainly concrete and brick walls from the decommissioning of nuclear plants or factories.

Table 1.3: Nuclear waste classification [3].

Classification	Description	Origin	Foreseen treatment (France)
Very Low Activity ($A_m < 100$ Bq/g)	concrete and brick walls	decommissioning of nuclear plants	surface storage
Category A	gloves, clothing, paper, tools, small material	nuclear plants operating, research and medical labs decommissioning	surface storage
Category B	Low Activity: graphite, resins Medium Activity: sludge, cladding	Research and nuclear plants decommissioning	under study temporary storage
Category C	fission products and minor actinides	fuel reprocessing	under study: geological disposal + transmutation

1.3.2   Nuclear fuel waste: inventory and radiotoxicity

The operating of nuclear reactors generates by far the major part of category C radioactive waste. These wastes consist mainly of uranium, but also of fission products and isotopes of plutonium and minor actinides like neptunium, americium and curium. This is the major drawback of the currently operating nuclear reactors. These wastes may be in the form of either spent fuel or liquid and solid products from the post-irradiation reprocessing of fuel.

In the reactor core, after the formation of ^{239}Pu explained in formula 1.1, this latter will then give heavier isotopes such as ^{241,243}Pu. These ones will then

decay in ^{241,243}Am after a β-decay. Thus, after successive β-decays and neutron captures, the isotopes spectrum of the fuel will get richer in new elements. The curium isotopes will also be generated via this process. Figure 1.3 shows a scheme of this uranium fuel cycle, whereas table 1.4 shows the post-irradiation inventory of the different isotopes present in a 3.5% enriched fuel from a 900 MW PWR with a 33 000 MWd/t burn-up value [7].

Table 1.4: Inventory of the different isotopes present in a 3.5% enriched fuel from a 900 MW PWR with a 33 000 MWd/t burn-up value after irradiation [7].

		Mass (kg)	Half-life (year)
Major Actinides	^{235}U	10.3	7.08x10^8
	^{236}U	4.1	2.34x10^7
	^{238}U	940.4	4.47x10^9
	Total U	954.7	
	^{238}Pu	0.15	87.7
	^{239}Pu	5.7	24 119
	^{240}Pu	2.2	6 569
	^{241}Pu	1.2	14.4
	^{242}Pu	0.5	3.7x10^5
	Total Pu	9.75	
Minor Actinides	^{237}Np	0.4	2.14x10^6
	^{241}Am	0.2	432.2
	^{243}Am	0.1	7 380
	^{243}Cm	$\simeq$0	28.5
	^{244}Cm	0.02	18.1
	^{245}Cm	0.003	8 500
	Total MA	0.75	
Fission Products	^{79}Se	0.005	70 000
	^{90}Sr	0.5	28
	^{93}Zr	0.7	1.5x10^6
	^{99}Tc	0.8	2.1x10^5
	^{107}Pd	0.2	6.5x10^6
	^{126}Sn	0.02	10^5
	^{129}I	0.2	1.57x10^6
	^{135}Cs	0.4	2x10^6
	^{137}Cs	1.1	30
	^{151}Sm	0.02	93
	Other (stable)	30.7	
Total FP	34.7		

The impact of the nuclear waste radioactivity on environment is described with the notion of radiotoxicity. This quantity is a function of the isotopes activity, the type of radioactivity and the chemical characteristics of the elements. Figure 1.2 shows the time evolution of the radiotoxicity of the main produced nuclei in reference to the raw uranium one. The most radiotoxic element is plutonium, with a radiotoxicity becoming lower than natural uranium after more than 10 000 years. On a short term, the fission products will highly contribute to the radiotoxicity, but between 100 and 10 000 years, the influence of americium and curium will be the major one after plutonium.
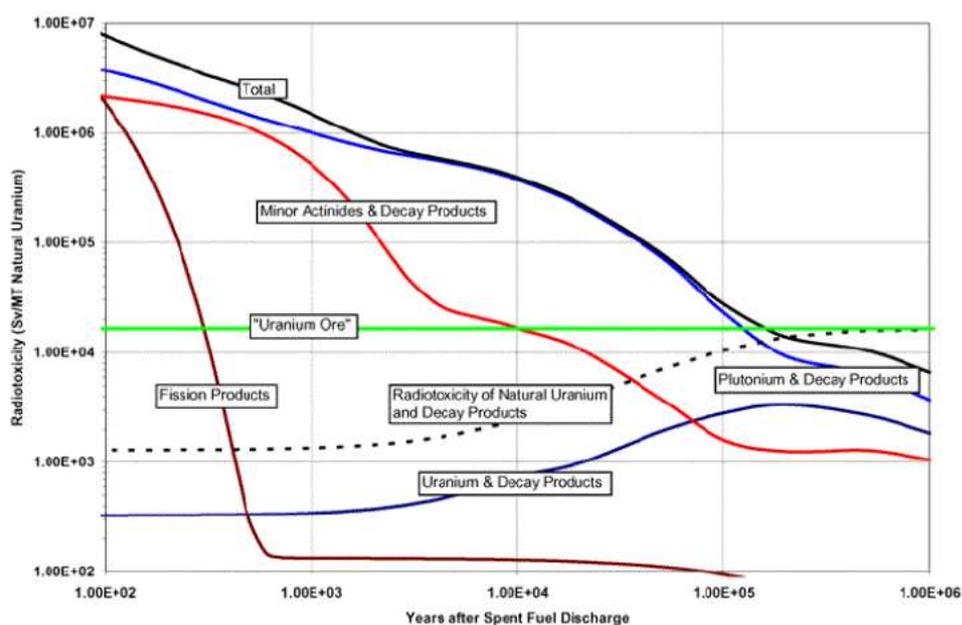
Figure 1.2: Time evolution of the spent fuel radiotoxicity in reference to natural uranium [8].

1.4   The options for nuclear waste management

Before any processing of the nuclear core waste, a pool storage of three to five years is compulsory, due to the important heat released by β and γ radiations. Two possibilities can then be considered:

- fuel reprocessing, in order to extract the uranium and plutonium that represent 96% of the irradiated fuel mass, before conditioning the remaining part. This recycled U and Pu can then be reinjected in the fuel cycle as mixed uranium-plutonium oxide (MOX). This solution, chosen in particular by France, the United Kingdom and Japan, is complex and quite expensive.

- direct storage, a simpler solution, but that leads to a much bigger volume of waste to be stored. This solution was adopted by countries such as the United States, Sweden and Germany (at least for part of its fuel).

In France, a special law (called "loi Bataille") was especially voted on 30th December 1991 to emphasize on the research on nuclear waste reprocessing. Three main research axes were defined in this frame:

- Axis 1: research on solutions concerning the partitioning and transmutation of long-lived radioactive waste.

- Axis 2: research on the possibilities for reversible or irreversible geological disposal, including building new underground laboratories.

- Axis 3: study all the possible conditioning processes for long period surface storage.

This law was meant to proceed to some research work on the three axes for 15 years, until 2006. It has been extended and completed by a new law voted on the 28th June 2006 relative to a sustainable management of radioactive waste and materials. This latter defines new time and guide lines for the 3 axes mentioned above [9]:

- Axis 1: a summary will be drawn in 2012 concerning the different transmutation possibilities. Depending on these results, some facility prototypes could be built from 2020 on, in view of an industrial use around 2040.

- Axis 2: an official request for a storage facility will be presented to the French government in 2015, based on the technological advances made in this field. This should lead to an industrially working facility around 2025.

- Axis 3: the new law foresees the enhancement of existing facilities and the creation of new ones until 2015, based on the considerable progess already made in this field.

Nuclear waste in France is currently separated via chemical reactions on the irradiated fuel with the so-called Purex process (Pu-U Refining by EXtraction), which extracts the uranium and plutonium from the spent fuel. The objective of advanced separation is to enlarge this sorting capacities to other highly radiotoxic elements such as long-lived fission products and minor actinides, in order to proceed then to their possible transmutation or conditioning.

1.4.1   Geological disposal

Global analysis of the nuclear waste management points out that there will always be high radioactivity waste to deal with on long term (at least 200 years for fission products). Therefore, creating long period storage sites seem to be unavoidable.

Underground storage would be based on the confining of waste in three different barriers: the waste container (possibly placed itself in a bigger container), the different surrounding walls of the storage location and finally the rock around the site. Such a disposal presents several advantages. First, it permits to avoid some sorts of accidents likely to happen on the surface, since the geochemical environment is much more stable, and the geological structure of the underground site is itself a supplementary confinement barrier. If, despite of this, some radioactive elements reach the biosphere, the chosen geological location has to insure a dilution ability of the released matter in order to minimize the concentration of the radionuclides at the surface.

Until now, only simulations in different geological environments have been achieved. They have shown that in a normal evolution scenario, that is to say without geological incident or intrusion, the doses released in the biosphere at long term remain much lower than the limits from the current security norms.

Yet, geological disposal also has some issues, such as a very high cost and a not obvious public acceptance. And because of their increasing volume, long term waste management cannot rely only on this kind of disposal. Reprocessing has thus become an important step for some countries. The transmutation of minor actinides appears to be an essential and complementary tool for waste management.

1.4.2   Transmutation of nuclear waste

Principle

The goal of transmutation is to transform long-lived isotopes into short-lived ones by means of nuclear reactions. The term of incineration is rather used in the

particular case where fission is used to transmute the nucleus.

Only neutron induced reactions are to be considered for transmutation or incineration, both because of their important cross sections and the small amount of energy required. It has been shown that any other process, such as direct spallation with a high energy proton beam or reactions with intense gamma rays, are not economically satisfying [10].

The first step in the transmutation process is the separation of the materials from the spent fuel into different waste streams, as it is done in France via the Purex process. Further promising research works are on-going concerning the extension of this process to the separation of minor actinides and some fission products (iodine, technetium and cesium) from the Purex product.

An interesting example to illustrate the transmutation principle is the case of ^{99}Tc. It is a long-lived fission product with a 2×10^5 year half-life. After a neutron capture, the resulting product ^{100}Tc decays in 16 s to the stable ^{100}Ru, as is shown in equation 1.5:

$$^{99}_{43}\text{Tc} + n \longrightarrow ^{100}_{43}\text{Tc} \xrightarrow{\beta^-(16s)} ^{100}_{44}\text{Ru} \tag{1.5}$$
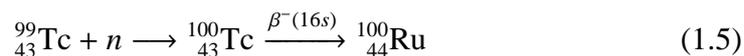
These transmutation and incineration processes can take place in a high neutron flux environment provided by thermal reactors, fast reactors or Accelerator Driven Systems (ADS), consisting of a high energy proton accelerator, a spallation target and a subcritical core.

Transmutation in current thermal or fast reactors

Concerning the transmutation occurring in a thermal or a fast reactor, the major difficulty lies in the conception of an adequate fuel permitting to burn the minor actinides within the limits of the operating parameters like the reactivity coefficient and the safety parameters. The PWR core can be designed to burn a precise amount of MA, but such a system can only stabilize their quantity and therefore cannot be considered as a true actinides incinerator. Moreover, the americium consumption is counterbalanced by a curium production of the same quantity.

Though neutronics calculations confirm the feasibility of thermal recycling the americium over several cycles, it is not proven that the fuel composition can ultimately reach the equilibrium [11]. A solution to this issue would be to transfer the americium in a fast cycle later on.

Due to these difficulties, and also because the resulting radiotoxicity diminution using this system remains quite low, the incineration of plutonium and americium in a PWR is a physically possible but not seducing solution. On the contrary,

a transmutation strategy using only fast reactors to replace the existing PWR permits to deal with the totality of the MA without a need of enriched uranium. That is why the main transmutation scenario under study is considering a smooth replacement of the current PWR fleet by innovative fast reactors.

Accelerator Driven Systems

A hybrid system comprises a particle accelerator coupled with a subcritical nuclear reactor. In a subcritical reactor, the number of fission neutrons is not sufficient to reach a stationary reaction rate. In order to maintain the reaction, it is necessary to bring in some more neutrons from an external source. In the hybrid system, these external neutrons are produced by spallation through the impact of a proton beam on a heavy material target such as lead. Most of the ADS concepts assume proton accelerators delivering continuous-wave beams with an energy around 1 GeV. The accelerator can be either a linear accelerator or a cyclotron.

The flux of external neutrons depends on the beam intensity, which permits a precise and almost instant control. The reactor being subcritical, the danger of reaction rate divergence is significantly reduced, which makes such a system much safer than the existing reactors.

In the context of transmutation, the possibility to operate a reactor core at a neutron multiplication factor $k_{eff} < 1$ allows to obtain a higher degree of flexibility in core design and fuel management. The neutron spectrum produced by spallation is characterized by a high fast neutrons flux, which is much in favor of the MA incineration. Hybrid systems would thus appear to be an interesting solution for the most difficult waste to eliminate, that is americium and curium, but the additional cost due to the target and accelerator inclusion makes them economically less attractive. That being said, research on this kind of innovative concepts is still very active, as can be seen with the construction of the MYRRHA prototype in Belgium, that is meant to be a European multipurpose research facility of the ADS type.

1.5   The thorium cycle: a possible alternative

Beside the well exploited U/Pu fuel cycle, another possible one corresponds to the Th/U cycle, which presents very interesting particularities, especially concerning the nuclear waste production, as will be explained below.

In this thorium cycle, the fissile element ^{233}U is produced starting from the fertile ^{232}Th isotope after a neutron capture followed by two β-decays (see figure 1.3):

$$^{232}_{90}\text{Th} + n \longrightarrow {}^{233}_{90}\text{Th} \xrightarrow{\beta^-\,(22min)} {}^{233}_{91}\text{Pa} \xrightarrow{\beta^-\,(27d)} {}^{233}_{92}\text{U} \qquad (1.6)$$
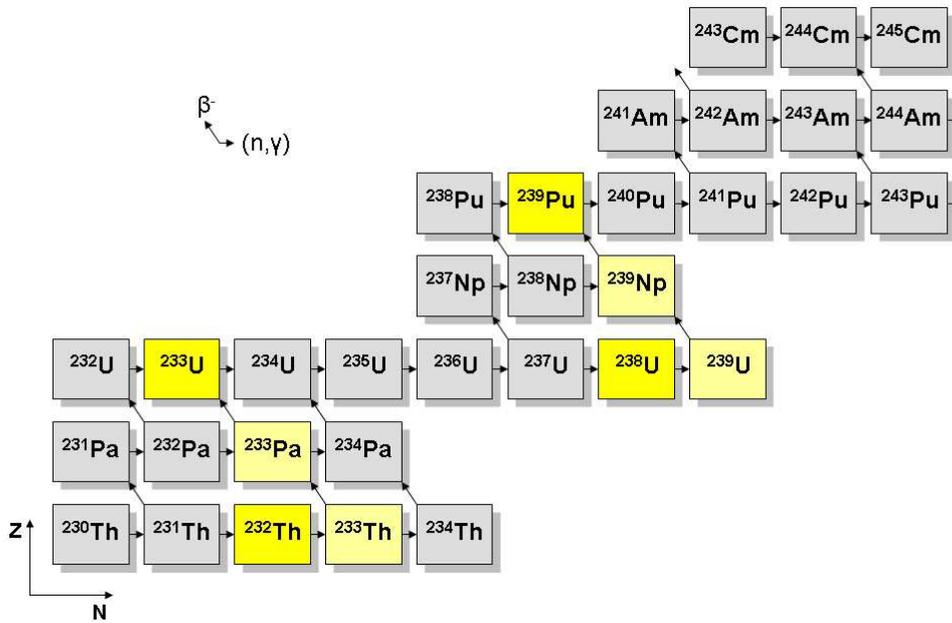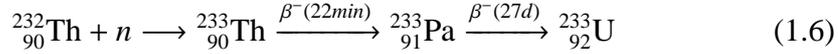
Figure 1.3: Formation and decay chains for the uranium and thorium cycles.

A first advantage from this cycle is the fact that thorium is 3 to 4 times more abundant than uranium in the earth crust. Moreover, unlike natural uranium which contains only 0.7% of the fissile ^{235}U isotope, natural thorium does not contain any fissile material and is wholly constituted of the fertile ^{232}Th isotope.

Another advantage concerns the good neutron properties of the ^{233}U in the thermal region, with η=2.29, which means a number of neutrons produced after a neutron absorption higher than ^{235}U and ^{239}Pu for the uranium cycle (respectively 2.07 and 2.11).

On the other hand, the control of the critical reactor is more delicate, due to the smaller amount of delayed neutrons. Another drawback of the thorium cycle concerns the much harder extraction of the thorium ore, because of its direct radiological impact. It is actually a strongly radiotoxic α emitter. Though a

few reactors have been built in the 1960s and 1970s, such as the Molten Salt Reactor Experiment (MSRE) and the CANada Deuterium Uranium (CANDU), the difficulty of the post-irradiation fuel reprocessing due to the presence of ^{232}U, a strong α emitter with a complex decay chain of radioactive isotopes, was a strong impediment to its development.

But despite of this, and because of the growing concern of the public opinion on nuclear waste and safely operating energy systems, the Th/U cycle has become quite appealing in some countries. This is especially the case for those without uranium enrichment capabilities, such as India, which is also particularly interested because of its large thorium resources.

1.6   Generation IV reactors

As we saw in the previous paragraphs, considerable research efforts are being made in order to define the best way to deal with the nuclear waste produced by the existing nuclear reactor fleet. In parallel of this, research is also concentrated in the development of a future generation of nuclear reactors, the so-called Generation-IV, to be operational by 2050. A special organization, the Generation-IV International Forum (GIF), was especially created to coordinate the research and development of promising techniques for future reactors, fuel compositions and fuel cycles. The reactors and their associated fuel cycles are considered to be part of a whole nuclear system that ought to be optimized in order to play a significant role in the sustainable energy policies.

The major objectives assigned to these future nuclear energy systems are the following:

- Enhanced economic competitiveness towards the other electricity production means.

- Improved safety and reliability, via a better reactor operating management under normal and abnormal conditions.

- Minimization of the long-lived radioactive waste production.

- Optimization of the resource use, through an efficient and flexible use of the available resources in fissile and fertile materials.

- Enhanced resistance to proliferation risks.

These last three objectives are fundamental for long term nuclear energy sustainability. Other considerations, such as the potential for other applications than electricity production (including hydrogen production or sea water desalination) do also have a considerable importance.

A number of six concepts have been retained for deeper investigation, research and development, namely the Very High Temperature Reactor (VHTR), the Gas cooled Fast Reactor (GFR), the Lead cooled Fast Reactor (LFR), the Sodium cooled Fast Reactor (SFR), the SuperCritical Water cooled Reactor (SCWR), and the Molten Salt cooled Reactor (MSR). Three systems are thermal reactors (the VHTR, the SCWR and the MSR) and the three others are fast reactors. The VHTR is the main one being researched for potentially providing high quality process heat for hydrogen production. The fast reactors offer the possibility of burning actinides to reduce radioactive waste and of being able to breed more fuel than they consume. These systems present significant advances in economics, safety and reliability, sustainability and proliferation resistance.

France has given priority to the development of two technologies (see figures 1.4 and 1.5:

- Gas cooled technology for both the thermal spectrum (VHTR) and the fast spectrum (GFR).

- Sodium cooled reactor technology (SFR).

Studies on a smaller scale are also to be conducted on supercritical technology, lead cooled fast breeder reactor and molten salt technology.

1.7 Nuclear data needs

1.7.1 The role of nuclear data

Nuclear data are necessary to the conception, safety evaluation and operating of nuclear plants and waste reprocessing facilities. They are also of great use in different other domains such as medicine, radioisotopes production or astrophysics. The different types of data can be, for instance:

- Total, capture and fission cross sections. Measuring these data usually require white neutron sources facilities with the time-of-flight technique for the neutron energy measurement.
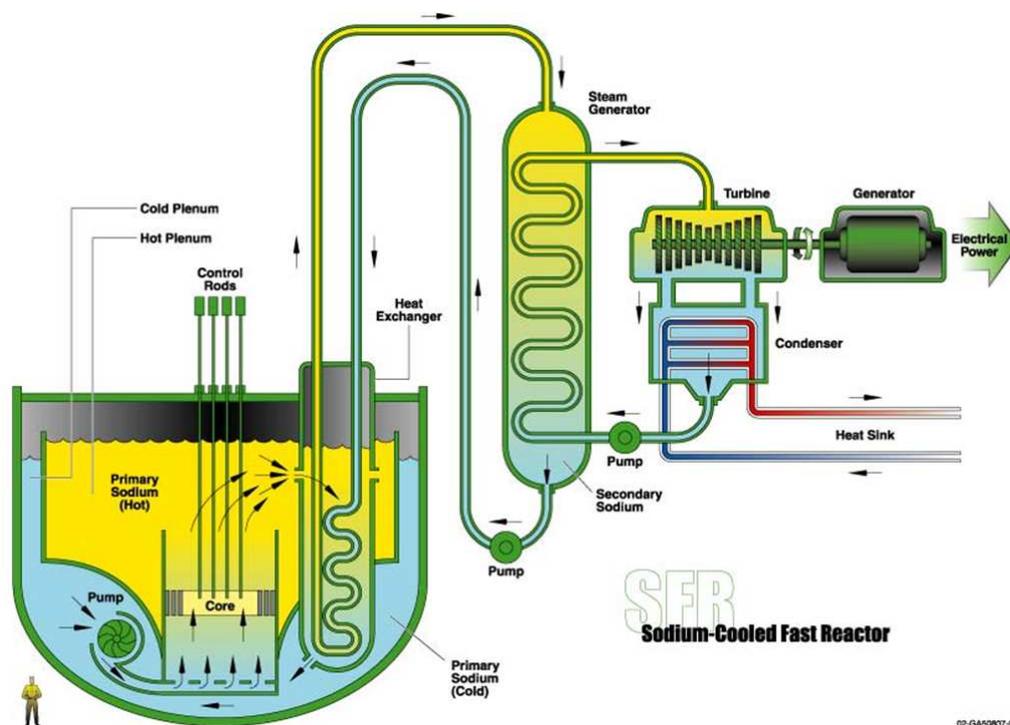
Figure 1.4: Scheme of the Sodium cooled Fast Reactor (SFR) concept [4].
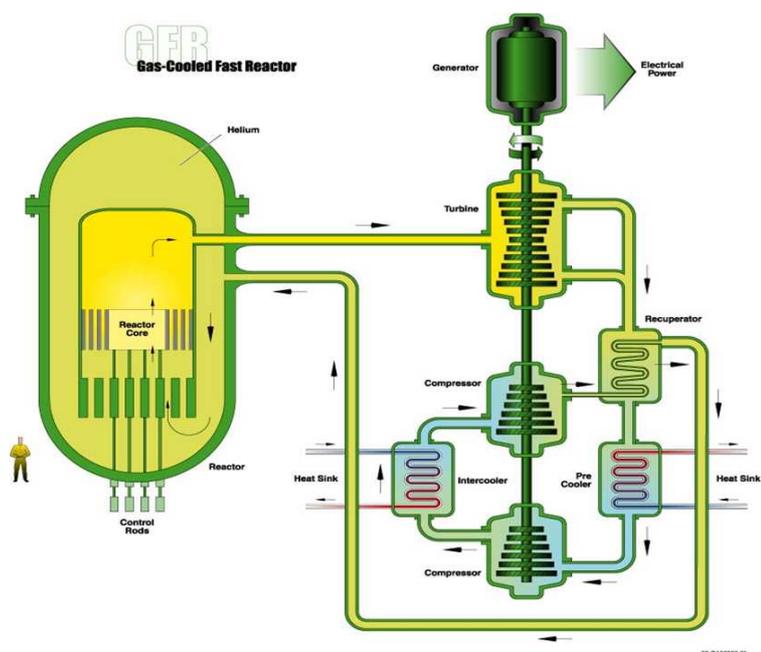
Figure 1.5: Scheme of the Gas cooled Fast Reactor (GFR) concept [4].

- Angular and energy distributions of scattered neutrons or secondary particles.

- Neutron or charged-particle induced activation cross sections.

- Fission yields for prompt and delayed neutrons.

- Fission product yields and their decay properties.

- Decay characteristics of unstable nuclei.

In current nuclear systems development programs, the emphasis is put on the data needs linked to the nuclear waste management (MA and fission products), on the conception of new fission reactor models (Generation-IV) and on the studies on protection, activation and heating of fusion reactor materials. Pu recycling in thermal reactors, as well as the use of different coolants and the thorium cycle also constitute new data needs. Recent studies on the ADS systems enlarged the energy range for the neutron interaction data needs beyond the usual limit of 20 MeV. They also showed a new need for proton interaction data until the GeV region.

We can identify two different steps in the nuclear data production:

1. Measurement of nuclear data.

   Differential measurement: These are microscopic nuclear data concerning the cross sections in function of the incident particle energy, or of the multiplicity, energy and angular distributions of secondary particles. Most of these data are published without restriction and widely spread.

   Integral measurement: They can be measured in critical reactors and are used to validate (or adjust in some cases) the differential data. They are often copyright protected and are only accessible to the organizations participating to their measurements.

2. Evaluation and validation of nuclear data. This consists in the interpretation and comparison of experimental data, validation against benchmark experiments, evaluation of statistical and systematic errors, check for internal consistency and uniformity with standard neutron cross sections, etc.

At the end of the process, recommended values are obtained. An evaluated data set for a particular isotope has to be as complete as possible, in particular for reactor applications, covering for instance the widest energy range. For this purpose, evaluators often combine experimentally measured cross sections with

predictions of nuclear model calculations with codes such as TALYS [12, 13] in order to get a single complete data set. The validation work points out the precision that can be expected from the evaluation calculations, as well as the possible data reevaluation need. The objective is always to get a new library with a better confidence level than the previous one.

A list of priority measurements is established by an international collaboration, coordinated by a subgroup of the Working Party on international Evaluation Cooperation (WPEC) of the NEA Nuclear Science Committee (NSC). Table 1.6 presents this high priority request list for MA in the relevant neutron energy ranges defined in table 1.5 [14]. The required accuracies are estimated based on sensitivity studies taking into account the required uncertainties on integral parameters.

Table 1.5: Definition of the neutron energy groups used in table 1.6.

Group number	Energy range (eV)	Group number	Energy range (MeV)
15	0 to 0.1	7	0.0248 to 0.0674
14	0.1 to 0.54	6	0.0674 to 0.183
13	0.54 to 4	5	0.183 to 0.498
12	4 to 22.6	4	0.498 to 1.35
11	22.6 to 454	3	1.35 to 2.23
10	454 to 2 040	2	2.23 to 6.07
9	2 040 to 9 120	1	6.07 to 19.6
8	9 120 to 24 800		

1.7.2   Nuclear data libraries

For the last decades, a large worldwide research programme on nuclear data has permitted the elaboration of vast databases of continuously growing quality. These experimental nuclear reaction databases, such as EXFOR (Experimental Nuclear Reaction Data) or CSISRS (Cross Section Information Storage and Retrieval System) [15], store nuclear reaction data and their bibliographic information, as well as information about the measurement. These include the status and history of the datasets.

Due to the large number of variables involved in the evaluation process, including the arbitrary choice of experimental data and of the model parameters, several different evaluated nuclear data files are compiled and maintained:

Table 1.6: NEA high priority nuclear data request list for MA in the relevant energy interval [14].

Isotope	Cross section	Group	Original uncertainty (%)	Required accuracy (%)
[241]Am	σ_{fiss}	5	8	4
		4	8	1 to 6
		3	10	1 to 6
		2	12	2 to 7
		1	13	6
	σ_{cap} and σ_{tot}	thermal		5
		10	7	3
		9	7	2 to 3
		8	7	2 to 3
		7	8	2 to 3
		6	7	2 to 4
[242]Am	σ_{fiss}	10	12	5
		9	12	7
		8	12	4 to 6
		7	14	4 to 6
		6	17	3 to 5
		5	17	3 to 8
		4	17	4 to 6
		3	20	8
		2	23	8
[244]Cm	σ_{fiss}	6	48	7
		5	37	4 to 12
		4	50	2 to 20
		3	44	3 to 14
		2	31	3 to 12
[245]Cm	σ_{fiss}	10	13	5
		9	13	4
		8	14	3 to 9
		7	27	3 to 11
		6	48	3 to 42
		5	37	3 to 13
		4	49	3 to 43
		3	44	6 to 14
		2	31	7

- The Joint Evaluated Fission and Fusion library (JEFF) for the Nuclear Energy Agency countries in Europe. The current version is JEFF-3.1 (released in 2005) [16].

- The Evaluated Nuclear Data File (ENDF/B) for the USA. The latest version ENDF/B-VII was released in 2007 [17].

- The Japanese Evaluated Nuclear Data Library (JENDL), with the current version JENDL-3.3 released in 2002 [18].

- The Russian evaluated neutron data library (BROND, Library of Recommended Evaluated Neutron Data), with a current version BROND-2.2 dating from 1992. The development of the version BROND-3 started in 1998 [19].

- The Chinese Evaluated Nuclear Data Library (CENDL), with the current version CENDL-3 released in 2001.

These nuclear reaction databases contain, under several sublibraries, evaluated cross sections, spectra, angular distributions, fission product yields, thermal neutron scattering, photo-atomic and other data, with a special emphasis on neutron induced reactions. the data are represented according to strict formatting rules, the ENDF format, documented in [20]. This format, originally for the ENDF library, has been adopted for all other libraries as well.

1.7.3   Americium nuclear data needs

Historically, the MA including americium isotopes have received little attention from the nuclear data and applications communities, therefore explaining the rather poor status of the different evaluation libraries. With the new needs just mentioned, it has been shown that the current uncertainties on neutron induced reaction cross sections on specific americium isotopes are too large for some important target accuracies.

There are several reasons explaining the weakness of the americium and curium data:

- The MA being present in the spent fuel up to 1%, the data uncertainties does not have major consequences on the fuel cycle precision and the safety of current reprocessing. But this won't be the case any more for innovative actinides burning reactors with a fuel containing up to 10% of MA.

- It is necessary to get some pure isotopes as samples to achieve the cross section measurements in good conditions, which is a very hard task for MA, due to the scarcity of material.

- The measurement facilities must have the ability to deal with such very active materials.

In the high fast neutron flux of a hybrid system, for instance, the reactions with a high threshold become much more important in comparison to thermal reactors. The threshold of (n,xn) reactions are of about $(x-1)E_s$, where E_s stands for the neutron binding energy, which is about 7 to 8 MeV for most of the nuclei. These reactions modify the flux and neutron spectrum, and therefore the reactor criticality. Knowing well these reaction cross sections is thus essential to master the hybrid system neutronics.

Figure 1.6 shows the status of the ^{241}Am(n,2n)^{240}Am reaction cross section. Two references report measured cross sections for the ^{241}Am(n,2n) reaction at neutron energies around 14 MeV [21, 22], and two recent works report data for neutron energies from threshold to 14 MeV [23, 24].

At 14 MeV the data of references [22, 24] are in good agreement, while the data from reference [21] appear to be systematically lower, agreeing only within one to two standard deviations with the other works. The data of references [23, 24] agree well below 10 MeV but reveal huge discrepancies around 11 MeV. Estimates of the cross section available from applications libraries (here the JEFF-3.1 adopted the estimates from ENDF/B-VII) show a large spread in the predicted excitation function [17, 18, 19]. Measurements at higher incident neutron energies are thus needed to guide evaluations and model calculations.

Concerning the ^{241}Am(n,tot) and ^{241}Am(n,γ) reaction cross sections, few recent experimental data are available. These latter present a huge discrepancy on the total cross section for the two first resonances (at 0.3 and 0.55 eV), and a strong disagreement for the capture cross section at the thermal point: between 700 b (integral value) and 620 b (differential value).

Figure 1.7 shows the status of the total americium cross section for the first resonances. The evaluation for the lowest resonances are based essentially on three measurements: Adamchuck *et al.* [25], Belanova *et al.* [26, 27], and Slaughter *et al.* [28]. The agreement for the lowest resonances between Adamchuck *et al.*, and Belanova *et al.* are satisfactory, neglecting a small shift in the energies of the lowest resonance, but the results by Slaughter *et al.* are different. The peak cross sections of the resonances are about 30% higher than for the two other measurements. The cross sections as suggested in the evaluation are typically somewhere in between those two curves. The JEFF-3.1 new reevaluation made
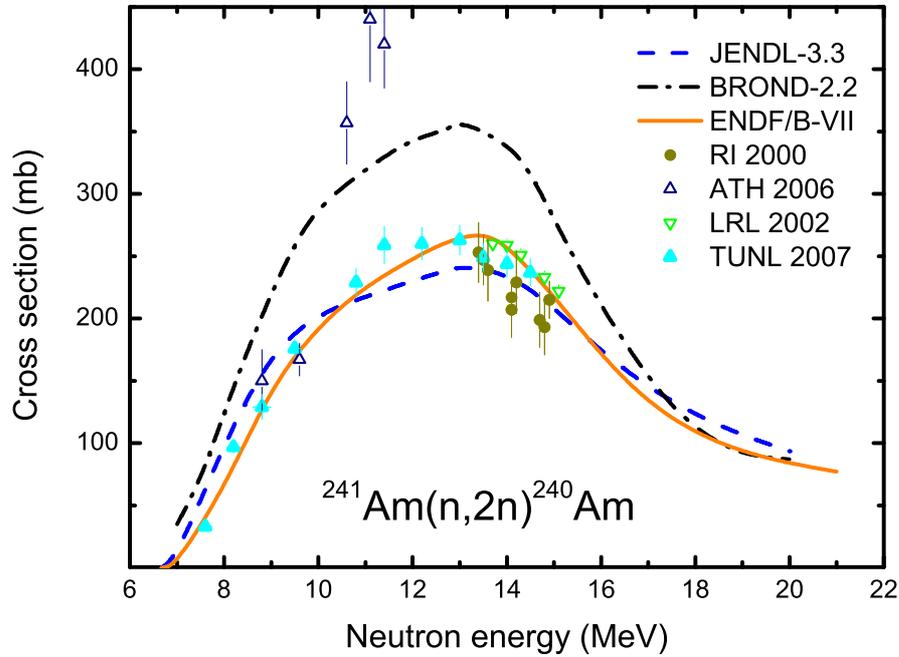
Figure 1.6: Status of the ^{241}Am(n,2n)^{240}Am cross section data and evaluations.

by O. Bouland [88] tends to reach the Slaughter *et al.* cross section values for the two first resonances though, following an integral measurement trend.

That is why a measurement campaign of induced neutron reaction cross sections on ^{241}Am has been launched in the frame of a collaboration between the EC-JRC and French laboratories from CNRS and CEA. This PhD work will present the measurements achieved for the ^{241}Am(n,2n) and ^{241}Am(n,tot) reaction cross sections.
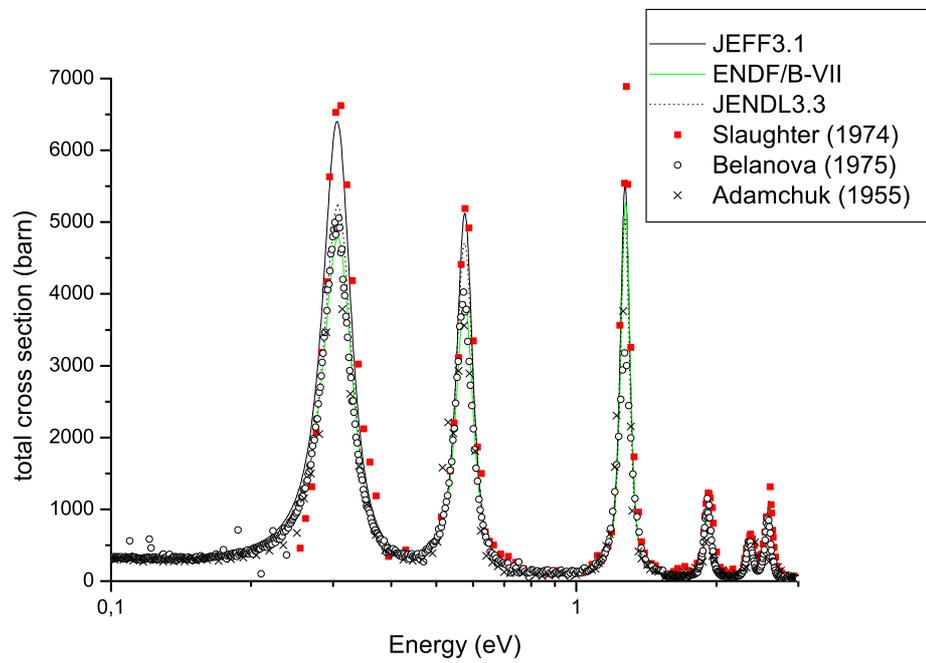
Figure 1.7: Status of the ^{241}Am(n,tot) cross section data for the first resonances.

Chapter 2

Neutron cross sections: theoretical aspects

In this chapter some theoretical aspects relative to neutron induced nuclear reactions will be discussed. In the first part, we will see the nature of the different nuclear reactions that can occur. We will then present the notions of compound nucleus, cross section and resonance.

In compound nuclear reaction theory, a collision matrix describes the interaction process with a nucleus, but is not easily accessible due to the complexity of the nuclear potential. We will see how the so-called R-matrix formalism can bring a solution to this matter. We will end this theoretical overview by presenting the Doppler effect, which has an important impact for the transmission measurements.

2.1   Concept of nuclear reactions

A nuclear reaction $A(x, y)B$ can occur when a projectile x comes sufficiently close to the target nucleus A, i.e. closer than the range of the strong nuclear force (10^{-15} m). A particle y is then emitted, leaving the residual nucleus B, which can be either stable, radioactive or an isomer. Such a reaction can entail three types of reaction mechanisms: direct, compound nucleus and pre-equilibrium. The contribution of these processes depends on the given reaction and the energy of the incident particle. The three types can be distinguished by their angular distributions and time scales.

Direct reactions: for incident particle energies above a few tens of MeV and for lighter target nuclei ($A < 30$) a direct transition from the entrance to the

exit channel occurs within a very short timescale of about 10^{-22} s, which is roughly the time it takes to cross the nucleus. According to the direct interaction model, the incident particle interacts with only one nucleon at a time, whereas the nuclear "core" remains inert or in a simple motion. This kind of interaction happens for energies where the incident particle wavelength is smaller than the average nucleon size in the target nucleus, which means above about 1 MeV for an incident neutron on a medium or heavy mass nucleus. There is no creation and subsequent decay of a highly excited intermediate state, which results in an anisotropic and forward-peaked angular distribution. Typical examples of direct reactions are potential scattering (also for E<1 MeV), charge transfer, stripping, pick-up and knock-on processes.

Compound nucleus reactions: most of the low energy neutron induced nuclear reactions follow this mechanism, which was first introduced by Niels Bohr [29]. The incident particle is captured to form a highly excited intermediate state C^*, whereby the available energy is distributed over all nucleons.

$$A + x \rightarrow C^* \rightarrow B + y \tag{2.1}$$
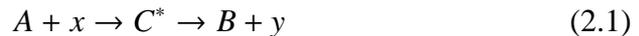
The compound nucleus decays by γ or neutron emission, or at higher energies by evaporation of one or more nucleons with a Maxwellian energy distribution. The emission is isotropic and the interaction time is about 10^{-14} to 10^{-18} s.

Pre-equilibrium reactions: on a time scale this process lies between the direct and the compound nucleus reactions. The particle is emitted before the energy is evenly distributed over all nucleons, thus giving a smooth forward-peaked angular distribution. Another characteristic is a pronounced high-energy tail in the excitation function.

Within the frame of the present work, only compound nucleus reactions are investigated.

2.2   Neutron induced nuclear reactions

The neutron was discovered by Chadwick in 1932 [30]. Because of its neutral charge, it constitutes a very interesting probe to study nuclei, since it is insensitive to the Coulomb barrier. Therefore, a neutron can approach the nucleus and induce a nuclear reaction even with an initial kinetic energy close to zero.

Table 2.1: Main neutron induced reaction types.

total reaction (n,tot) σ_t	• *direct reactions* (*potential scattering* σ_p, direct capture)	
	• *compound nucleus reactions*	• *elastic scattering* (n, n) σ_s
		• *inelastic scattering* (n, n') $\sigma_{s'}$
		• *radiative capture* (n, γ) σ_γ
		• *fission* (n, f) σ_f
		• *emission* $(n, xn), (n, p), (n, \alpha)$

We speak of a neutron induced nuclear reaction when the incident particle x from equation (2.1) is a neutron n that hits the target nucleus A. Another particle y is then emitted, leaving a residual nucleus B. The probability for this type of reaction to occur is related to the *cross section* $\sigma_{n,y}$. It is defined as the number of reactions (n,y) on a target nucleus per unit time and unit incident particle flux. The cross section is expressed in barns (1 b = 10^{-24} cm^2) and is a function of the energy of the incident particle. The plot of $\sigma(E)$ versus E is called the *excitation function*. Taking into account the angular distribution of the emitted particle in the solid angle $d\Omega$, one gets the *differential cross section $d\sigma/d\Omega$*, or $d\sigma/dE$ if we take into account the energy of the outgoing particle dE. The *double differential cross section $d^2\sigma/d\Omega dE$* is a function of the kinetic energy E of the emitted particle and of the emission angle θ.

2.2.1   Partial cross sections

The different partial cross sections are associated to the different reaction channels that are likely to occur in a compound nucleus reaction. These partial cross sections are:

- Elastic scattering cross section σ_s: the compound nucleus changes back to the target nucleus in its fundamental state by emission of a neutron of the same energy than the incident one. Unlike the potential scattering cross section σ_p that occurs without the formation of a compound nucleus, it is associated to a partial width called neutron width and written Γ_n.

- Inelastic scattering cross section $\sigma_{s'}$: the process is identical to the previous one, but the target nucleus is left in an excited state. It is then a threshold

reaction, since the incident neutron energy in the center of mass has to be equal or higher than the one of the target nucleus first excited state. $\Gamma_{n'}$ refers to the inelastic scattering partial width.

- Capture cross section σ_γ: the compound nucleus de-excites by the emission of at least one γ-ray. The corresponding partial width is the radiation width Γ_γ. The spectrum of the emitted γ-rays is discrete and determined by the selection rules. It is a function of the energies, spins and parities of the excited states.

- Fission cross section σ_f: the compound nucleus becomes highly deformed up to the point where it fissions into two fragments. The excitation energy is then transformed into the kinetic and excitation energies of the fission fragments. The fission partial width is Γ_f.

- Emission partial cross sections: the compound nucleus de-excites by emitting charged particles such as protons ($\sigma_{n,p}$ and Γ_p), deuterons ($\sigma_{n,d}$ and Γ_d), α particles ($\sigma_{n,\alpha}$ and Γ_α) or a neutron ($\sigma_{n,n}$ and Γ_n). After a first neutron emission, and if the resulting state of the nucleus is still excited enough, there can be an emission of a second neutron, a third one, etc. Following this process, we can get a cascade emission of x neutrons. The associated cross sections will be $\sigma_{n,xn}$ with a partial width Γ_{xn}.

Table 2.1 shows the main neutron induced reaction types and figure 2.1 is an example of such cross sections for the ^{241}Am isotope.

2.2.2   Compound nucleus reactions

The complete and rigorous description of the interaction between a neutron and a nucleus is complex, as it consists in solving an N body problem. Theoreticians were then led to develop simplified models of the system.

In the frame of Bohr's compound nucleus theory, a neutron induced reaction is considered as a two-step process:

- the compound nucleus formation: the neutron energy in the center of mass, composed of the sum of its kinetic energy and the neutron binding energy for the compound nucleus, is shared between all nucleons of the nucleus.

- the compound nucleus desexcitation.
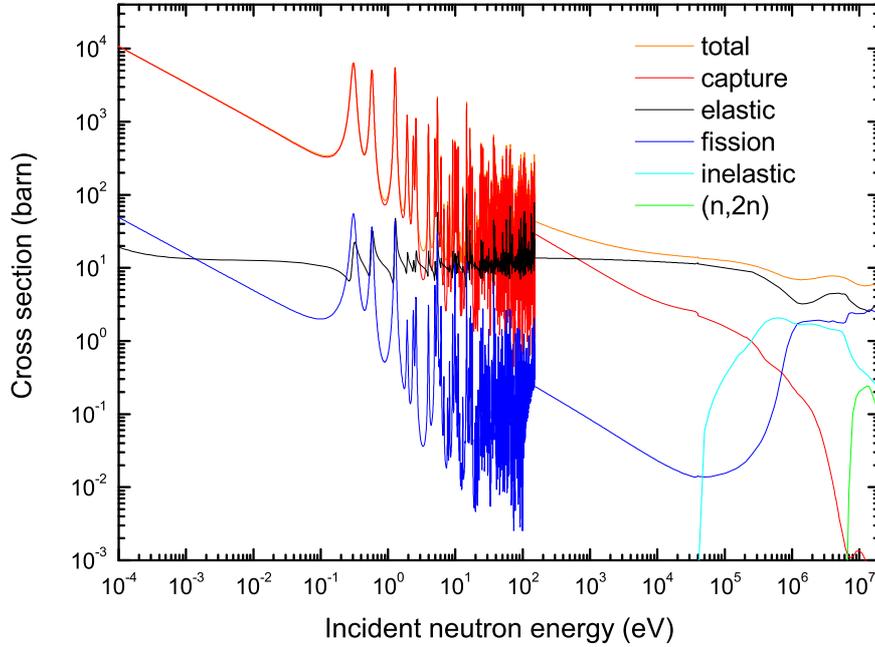
Figure 2.1: Total, capture, elastic, fission, inelastic and (n,2n) cross sections for the ^{241}Am isotope from the JEFF-3.1 library.

Since it is almost impossible to describe a nucleus and its excited states in terms of wave functions, Bohr's compound nucleus model provides an adequate description of the interactions through the statistical properties of the nuclear system. The complex interactions between the $A + 1$ nucleons lead to the independence hypothesis according to which the formation and the decay of the compound nucleus are independent from one another.

This compound nucleus model was introduced by Niels Bohr to explain the observed resonances in neutron induced nuclear reactions, as can be seen on figure 2.1. Variations of several orders of magnitude can indeed be observed in such cross sections. These resonances are located in the same energy range for all partial cross sections, and to each resonance corresponds an excited state of the compound nucleus. The lifetime τ of this excited state is finite, and satisfies the Heisenberg uncertainty principle with the relation

$$\tau \cdot \Gamma \approx \hbar \qquad (2.2)$$

where Γ stands for the energy width of this level, i.e. the resonance energy width.

The total width of a level is the sum of the partial widths corresponding to the decay possibilities of the excited compound nucleus. In the resonance energy range of ^{241}Am (about 0.1 eV to 100 eV), only elastic scattering, fission and capture events can occur. The total width will then be defined as:

$$\Gamma = \Gamma_n + \Gamma_\gamma + \Gamma_f \qquad (2.3)$$

These excited states are therefore quantum states with finite lifetimes. Their decay time distribution corresponds to a decreasing exponential. Determining the square of the absolute value of the Fourier transform for this exponential will lead to the energy distribution $P(E)$ associated to these states:

$$P(E) = \frac{\Gamma/2\pi}{(E - E_0)^2 + \Gamma^2/4} \qquad (2.4)$$

with E_0 the level energy and Γ its width.

We usually distinguish two different energy regions characterizing the compound nucleus resonance reaction cross sections. The Resolved Resonance Region (RRR) is located at the lower incident neutron energies (including the thermal region), which is until a few keV for heavy nuclei, and a few MeV for lighter ones. The resonances appear well separated and their shape is entirely observable. In this region, the neutron capture cross section behaviour follows a decreasing $1/\sqrt{E}$ shape, on top of which the resonance peaks are superimposed. The spacing between the resonances is about a few eV for heavy nuclei and a few keV or tens of keV for lighter and magic ones. Generally speaking, the more nucleons there are in the compound system, the finer the resonant structure is. With the increasing neutron energy, the spacing between resonances decreases whereas their width increases. At a certain stage, the resonances won't be resolved anymore, because of the experimental resolution and Doppler broadening, but also due to important level overlap. This region is the so-called Unresolved Resonance Range (URR).

The resonances have a definite angular momentum and parity J^π. The possible values depend on the spin I and parity π_I of the target nucleus, on the spin $i = 1/2$ and parity $\pi_i = +$ of the incident neutron and on the orbital momentum l. Their vectorial combinations lead to the channel spin s, and to the angular momentum J and parity π of the compound state:

$$|I - i| \leq s \leq I + i \qquad (2.5)$$

$$|l - s| \leq J \leq l + s \qquad (2.6)$$

$$\pi = (-1)^l \pi_I \pi_i \qquad (2.7)$$

The possible J^π values for the americium resonances are given in table 2.2. An interaction may occur if the $J'^{\pi'}$ value of the exit channel is equal to the J^π value of the entrance channel, according to the quantum mechanics conservation law. The number of possible ways to reach a state characterized by an angular momentum J is given by the statistical spin factor g_J, corresponding to:

$$g_J = \frac{2J + 1}{(2i + 1)(2I + 1)} \tag{2.8}$$

Table 2.2: Possible J^π values for the s-, p- and d-waves of ^{241}Am.

I^π	l	s	J^π					g_J					wave
	0	2	2^-					5/12					s
		3	3^-					7/12					
$5/2^-$	1	2	1^+	2^+	3^+			1/4	5/12	7/12			p
		3	2^+	3^+	4^+			5/12	7/12	3/4			
	2	2	0^-	1^-	2^-	3^-	4^-	1/12	1/4	5/12	7/12	3/4	d
		3	1^-	2^-	3^-	4^-	5^-	1/4	5/12	7/12	3/4	11/12	

2.3 R-matrix formalism

The R-matrix theory is thoroughly explained in [31]. We will present here a short overview of this formalism.

2.3.1 Description

The principle of the R-matrix formalism consists of assuming both incident particles and emerging reaction products as ingoing and outgoing wave functions. Since the nuclear forces are short-ranged, the configuration space is divided into an external and an internal region separated by an imaginary closed surface of radius a_c. The internal region, corresponding to the compound nucleus, is located inside this arbitrary volume, which size is slightly bigger than the one occupied by the nucleons. This radius can be defined by

$$a_c = r_0(1 + A)^{1/3} \tag{2.9}$$

with A the mass number of the the target nucleus and r_0 a constant number. The usual convention for a_c is $a_c = 0.8 + 1.23A^{1/3}$ (expressed in fm).

In the external region the nuclear forces are negligible. Therefore, the asymptotic wave function governing the dynamic of the free interacting particles may be known analytically. On the contrary, in the internal region the nuclear forces predominate. The neutron and the nucleus are merged together to form a system of $A + 1$ nucleons in interaction which increases the complexity of the wave function of the nuclear system.

In such a configuration, nuclear reactions occur in two steps: the first one corresponds to the entrance channel $c = \{\alpha, l, s, J\}$ and will lead to the compound nucleus, whereas the second one will be the exit channel $c' = \{\alpha', l', s', J'\}$. These steps are characterized by the nature α and the quantum states l, s, J of the compound nucleus components.

Although the internal wave function is unknown, the internal domain may be treated in terms of the collision matrix U which describes the nuclear interaction. For a given ingoing wave c, all outgoing wave functions c' (or partial cross sections $\sigma_{cc'}^{J}$) may be expressed under the following simplified way:

$$\sigma_{cc'}^{J} = \pi \lambdabar^2 g_J \mid \delta_{cc'} - U_{cc'} \mid^2 \tag{2.10}$$

with

$$U_{cc'} = U_{\alpha l s, \alpha' l' s'}^{J} \qquad \text{and} \qquad \delta_{cc'} = \delta_{\alpha \alpha'} \delta_{l l'} \delta_{s s'} \tag{2.11}$$

where $\mid U_{cc'} \mid^2$ is the probability of a transition from channel c to channel c', and $\delta_{cc'}$ occurs because the ingoing and the outgoing particles cannot be distinguished if $c = c'$.

The cross sections of a reaction leading from a system α to a system α' are then given by the formula

$$\sigma_{\alpha \alpha'} = \pi \lambdabar^2 \sum_{J} g_J \sum_{l, s, l', s'} \mid \delta_{cc'} - U_{cc'} \mid^2 \tag{2.12}$$

The elastic scattering cross section will then be:

$$\sigma_{\alpha \alpha} = \pi \lambdabar^2 \sum_{J} g_J \sum_{l, s} \mid 1 - U_{cc} \mid^2 \tag{2.13}$$

whereas the total cross section will be:

$$\sigma_{\alpha} = 2\pi \lambdabar^2 \sum_{J} g_J \sum_{l, s} (1 - Re(U_{cc})) \tag{2.14}$$

The matrix $U_{cc'}$ makes then the link between the ingoing and outgoing wave functions, that together constitute the wave function in the external region $r > a_c$.

Though the outgoing wave function's shape is known, since it is the solution of the Schrödinger equation in absence of potential, the boundary conditions still have to be specified to get the unknown phase and amplitude.

If the wave function in the internal region $r < a_c$ were known, these boundary conditions could be applied by insuring the continuity of the total wave function and its derivative at $r = a_c$. Yet, the nucleus potential is far too complex to solve the Schrödinger equation in the internal region. Nevertheless, it is possible to describe a wave function as a linear combination of its eigenstates. That is how the matrix R, which contains the properties E_λ and $\gamma_{\lambda c}$ of the eigenstates:

$$R_{cc'}(E) = \sum_\lambda \frac{\gamma_{\lambda c}\gamma_{\lambda c'}}{E_\lambda - E} \tag{2.15}$$

is used to put together the wave function at the surface. E corresponds to the incident particle energy, λ refers to the index of the internal region states, E_λ will be the eigenstates of the λ states energy, and $\gamma_{\lambda c}$ the width amplitudes of channel c for a state λ. According to the fundamental assumptions of the statistical model, $\gamma_{\lambda c}$ and $\gamma_{\lambda c'}$ are independent, uncorrelated and have random signs. These assumptions imply that the statistical properties of the exit channel c' contain no memory of the entrance channel. Besides, the square of these amplitudes is proportionnal to the partial widths $\Gamma_{\lambda c}$.

At $r = a_c$, the value and the derivative of the internal and external wave funcions can be matched. After further untrivial mathematical operations, the collision matrix $\mathbf{U}$ can be expressed in function of the matrix R. For neutral incident particles, this expression will be:

$$U_{cc'} = e^{-i(\phi_c+\phi_{c'})}\left\{\delta_{cc'} + 2iP_c^{\frac{1}{2}}[(\mathbf{1} - \mathbf{R}(\mathbf{L} - \mathbf{B}))^{-1}\mathbf{R}]_{cc'}P_{c'}^{\frac{1}{2}}\right\} \tag{2.16}$$

with

$$L_c = S_c + iP_c \tag{2.17}$$

and where

- ϕ_c is the hard-sphere potential scattering phase shift,

- P_c is the penetration factor in the potential barrier. It is the imaginary part of the logarithmic derivative of the outgoing wave function at the channel radius a_c. For neutron induced reactions, this penetration factor is defined by the centrifugal-barrier penetrability,

- S_c is the shift factor and is the real part of the logarithmic derivative of the outgoing wave function at the channel radius a_c,

- B_c is the boundary condition at the channel radius a_c.

For neutral projectiles (c=n), ϕ_n, S_n and P_n for s-, p-, and d-waves are defined in table 2.3. They depend on the parameter ρ, which is itself a function of the channel radius a_c and of the wave number k:

$$\rho = ka_c \tag{2.18}$$

with

$$k = \frac{1}{\lambda} = \frac{\sqrt{2m_n E_n}}{\hbar} \tag{2.19}$$

They are calculated following the recursion relations

$$\phi_0 = \rho \qquad \text{and} \qquad L_0 = i\rho \tag{2.20}$$

$$\phi_l = \phi_{l-1} + \arg(l - L_{l-1}) \qquad \text{and} \qquad L_l = -l - \frac{\rho^2}{L_{l-1} - l} \tag{2.21}$$

Table 2.3: The hard-sphere phase $\phi_{n,l}$, the shift factor $S_{n,l}$ and the penetration factor $P_{n,l}$ as a function of ρ for s-, p- and d-wave neutrons.

l	wave	$\phi_{n,l}$	$S_{n,l}$	$P_{n,l}$
0	s	ρ	0	ρ
1	p	$\rho - \arctan(\rho)$	$-\frac{1}{1+\rho^2}$	$\frac{\rho^3}{1+\rho^2}$
2	d	$\rho - \arctan(\frac{3\rho}{3-\rho^2})$	$\frac{-3(\rho^2+6)}{9+3\rho^2+\rho^4}$	$\frac{\rho^5}{9+3\rho^2+\rho^4}$

Another difficulty has to be overcome concerning the untrivial inversion of the $(\mathbf{1} - \mathbf{R}(\mathbf{L} - \mathbf{B}))$ term. For this purpose, a new inverse matrix written A^{-1} was introduced by Wigner following this formula:

$$[\mathbf{1} - \mathbf{R}(\mathbf{L} - \mathbf{B})]_{cc'}^{-1} = \delta_{cc'} + \sum_{\lambda\mu} \gamma_{\lambda c}(L_{c'} - B_{c'})\gamma_{\mu c}A_{\lambda\mu} \tag{2.22}$$

and considering the definition of the matrix $\mathbf{A}^{-1}$:

$$A_{\lambda\mu}^{-1} = (E_\lambda - E)\delta_{\lambda\mu} + \Delta_{\lambda\mu} - \frac{i}{2}\sum_c \sqrt{\Gamma_{\lambda c}\Gamma_{\mu c}} \tag{2.23}$$

or also written

$$A_{\lambda\mu}^{-1} = (E_\lambda - E)\delta_{\lambda\mu} + \sum_c (L_c - B_c)\gamma_{\lambda c}\gamma_{\mu c} \tag{2.24}$$

with the level shift $\Delta_{\lambda\mu}$

$$\Delta_{\lambda\mu} = -\sum_c (S_c - B_c)\gamma_{\lambda c}\gamma_{\mu c} \tag{2.25}$$

and the following formula between the partial width $\Gamma_{\lambda c}$ and the reduced width amplitude $\gamma_{\lambda c}$:

$$\Gamma_{\lambda c} = 2\gamma_{\lambda c}^2 P_c \tag{2.26}$$

From equation (2.16) established for neutral incident particles, we get a new formula for the collision matrix U:

$$U_{cc'} = e^{-i(\phi_c + \phi_{c'})}\left\{\delta_{cc'} + i\sum_{\lambda\mu} \sqrt{\Gamma_{\lambda c}}A_{\lambda\mu}\sqrt{\Gamma_{\mu c'}}\right\} \tag{2.27}$$

2.3.2   Approximations of the R-matrix

The exact use of the R-matrix theory is often too complex for a numerical implementation in a computer program because of too many neutron induced reactions on medium and heavy nuclei. The practically important variants of the R-matrix formalism presented in this work are the Reich-Moore approximation [32] and the Single Level Breit-Wigner approximation (SLBW) [33].

The Reich-Moore approximation

The Reich-Moore approximation neglects the off-diagonal contribution of photon channels (c=γ). This approximation is valid, because there are usually many channels where decay amplitudes have comparable magnitude and random signs. Therefore, their contribution to the sum over the photon channel tends to cancel:

$$\sum_{c\in\gamma} \gamma_{\lambda c}\gamma_{\mu c} \simeq 0 \qquad (\lambda \neq \mu) \tag{2.28}$$

The photon channels are only taken into account through the total radiation width defined as:

$$\Gamma_{\lambda\gamma} = \sum_{c\in\gamma}\Gamma_{\lambda c} \tag{2.29}$$

The resulting collision matrix will then become a function of a reduced R-matrix defined over the non-photonic channels:

$$R_{cc'} = \sum_\lambda \frac{\gamma_{\lambda c}\gamma_{\lambda c'}}{E_\lambda - E - i\Gamma_{\lambda\gamma}/2} \qquad (c, c' \neq \gamma) \tag{2.30}$$

Excluding the photon channels reduces largely the number of channels and therefore the matrix inversion needed in the relation between the R-matrix and the cross sections. At low neutron energy, the reduced R-matrix dimension for fissile target nuclei is usually a 3 x 3 matrix (1 elastic plus 2 fission channels). In the frequent case that only the elastic scattering and neutron capture channels are open, the number of channels in the R-matrix is one: the neutron channel, the photon channels being excluded explicitly. The R-matrix becomes in this case an R-function the inversion of which is straightforward. Including other channels, like for instance one or two fission channels as it is the case for ^{241}Am in the RRR, keeps the number of channels low and makes the inversion still feasible. This approximation is the most accurate one used and was the one chosen in this work for the americium total cross section analysis.

The Single Level Breit Wigner approximation

The Breit-Wigner formalism corresponds to an R-matrix approximation which consists of taking into account each level separately. It is therefore only valid for isolated resonances, which means resonances whose width is much smaller than the spacing with the neighboring ones with the same spin. The interferences between the states being neglected, the off-diagonal elements from the level matrix $\mathbf{A}^{-1}$ are equal to zero, and we get then from equation (2.23):

$$A_{\lambda\lambda}^{-1} = (E_\lambda - E) + \Delta_\lambda - \frac{i}{2}\Gamma_\lambda \tag{2.31}$$

where the total width $\Gamma_\lambda = \sum_c \Gamma_{\lambda c}$ of level λ corresponds to the resonance total width, and $\Delta_\lambda = E_\lambda - E_r$ to the shift between the level energy E_λ and the resonance energy E_r.

Following equation (2.27) giving the general form of the collision matrix, this latters becomes in the frame of this approximation:

$$U_{cc'} = e^{-i(\phi_c + \phi_{c'})}\left\{\delta_{cc'} + \frac{i\sqrt{\Gamma_{\lambda c}\Gamma_{\lambda c'}}}{E_\lambda - E + \Delta_\lambda - i\Gamma_\lambda/2}\right\} \tag{2.32}$$

The resulting total and partial cross sections are expressed as follows:

$$\sigma_c^J = \pi\lambda_c^2 g_J\left(4\sin^2\phi_c + \frac{\Gamma_\lambda\Gamma_{\lambda c}\cos 2\phi_c + 2(E - E_\lambda - \Delta_\lambda)\Gamma_{\lambda c}\sin 2\phi_c}{(E - E_\lambda - \Delta_\lambda)^2 + \Gamma_\lambda^2/4}\right) \tag{2.33}$$

$$\sigma_{cc'}^J = 4\pi\lambda^2\frac{g_J\Gamma_{\lambda c}\Gamma_{\lambda c'}}{(E_\lambda - E)^2 + \Gamma_\lambda^2/4} \tag{2.34}$$

The first part of the total cross section is the potential scattering cross section $\sigma_p = 4\pi \lambdabar_c^2 g_J \sin^2 \phi_c$. It is associated with the elastic scattering of the incoming neutron from the potential of the nucleus without forming a compound state. The term with the factor $\sin 2\phi_c$ is the interference of the potential scattering and the resonant elastic scattering through formation of a compound nucleus. Finally the term with $\cos 2\phi_c$ describes the resonance cross sections of the channels.

In the case where resonances are not so well separated, several resonances can be taken into account as a sum of Breit-Wigner single level cross sections. This corresponds to an extension of the SLBW called the Multi Level Breit-Wigner approximation (MLBW), where any possible interference between channels and levels are neglected.

2.4 Doppler effect

In an actual experiment, even with the best experimental resolution, the observed cross section in the resonance region is not the actual nuclear cross section, but a cross section that is Doppler broadened due to the thermal motion of the target nucleus in the sample. The theoretical cross sections have then to be averaged over the thermal motion of the target nuclei. This is achieved by convoluting the unbroadened cross section σ with the so-called scattering function $S(E', E)$ [34]. We get then the Doppler broadened cross section σ_D via the formula:

$$\sigma_D(E) = \int S(E', E)\sigma(E')dE' \tag{2.35}$$

with E' the energy transfered to the target nucleus and E the initial neutron energy. $S(E', E)$ contains all the information on the nuclei dynamics and neutron scattering process.

In most cases, the Doppler broadening calculations rely on the free gas model, which assumes that the target nuclei have a velocity distribution characteristic of a free gas at an effective temperature T_{eff}. However in some cases, especially for lower energy resonances or when atoms are bound in a crystal lattice, it is preferable to use a more realistic model such as the harmonic crystal model. Both models are thoroughly explained in references [35, 36], and we will here summarize the formulas of interest.

2.4.1 Free gas model

The Doppler broadening for the free gas model is obtained via the scattering function:

$$
\begin{aligned}
S_{FGM}(E', E) = & \frac{1}{\Delta \sqrt{\pi}} \left(1 + \frac{1}{A}\right)^{\frac{3}{2}} \sqrt{\frac{E - E'}{E}} \\
& \cdot \left[e^{-\frac{A}{k_B T_{eff}} \left(\sqrt{E} - \sqrt{(E-E')(1+1/A)} \right)^2} - e^{-\frac{A}{k_B T_{eff}} \left(\sqrt{E} + \sqrt{(E-E')(1+1/A)} \right)^2} \right]
\end{aligned}
\tag{2.36}
$$

where the Doppler width Δ is given by:

$$
\Delta = 2 \sqrt{\frac{E k_B T_{eff}}{A}}
\tag{2.37}
$$

with A the target mass and k_B the Boltzmann constant. The effective temperature is usually given by:

$$
T_{eff} = \frac{3}{8} \theta \coth\left(\frac{3}{8} \frac{\theta}{T} \right)
\tag{2.38}
$$

where θ is the Debye temperature and T the sample temperature. This approximation is valid in the case of an effective temperature slightly higher than the sample temperature.

In the resonance energy range, the thermal motion of the target nucleus is negligible in comparison with the incident neutron energy. Equation (2.36) can then be approximated by the formula

$$
S_{FGM}(E', E) = \frac{1}{\Delta \sqrt{\pi}} \cdot e^{-\frac{\left(E' - \frac{E}{A}\right)^2}{\Delta^2}}
\tag{2.39}
$$

This formulation of the scattering function leads to a convolution of the cross section with a Gaussian function with a width Δ, which is why this latter is called the Doppler width.

2.4.2 Harmonic crystal model

In the frame of the harmonic crystal model [37], the scattering function is given by:

$$
S_{HCM}(E', E) = \frac{1}{2\pi} \int_{-\infty}^{+\infty} e^{iE't} e^{g_C(E,t)} dt
\tag{2.40}
$$

The function $g_C(E, t)$ contains all the crystal information, such as the phonon vibration spectrum of the target nucleus in the crystal lattice.

Chapter 3

The ^{241}Am(n,2n)^{240}Am reaction cross section: experimental procedure

There is no general method that would be applicable to any isotope for the measurement of (n,xn) cross sections. There are in fact three main ones that can be used in different situations: the direct detection of emitted neutrons, the prompt γ spectroscopy and the activation technique.

The first one consists in measuring the energy and angular distribution of the emitted neutrons produced in the reaction process. It is the most direct method, but some difficulties concerning the competing reactions with a different number of emitted neutrons can make it difficult, as well as the determination of the incident neutron flux and its distinction from the neutrons emitted. A detection efficiency as close as possible to 100% gives the best results. In the case of fissile nuclei, neutrons produced via the fission reaction add another background component to the detection of the emitted neutrons.

Prompt gamma spectroscopy is a method where the reactions induced by a particle beam are studied through the characteristic γ-rays emitted by the compound or residual nucleus. This method often implies very high instant count rates. Measuring the detection time of the prompt gamma transitions usually gives the neutron time of flight, and consequently the incident neutron energy. It is the usual method employed with white neutron sources.

The activation method is relevant for reactions where the product nucleus is unstable or in a metastable state. An activation cross section to the ground state is besides the only technique that measures unambiguously the (n,2n) cross section. This method consists of two distinct steps: the target irradiation with a

monoenergetic neutron beam, followed by off-line γ spectroscopy of the irradiated target. A relatively long irradiation and a measuring time of the same order of magnitude than the produced isotope half-life is then required to use this method.

^{241}Am is one of the few minor actinides where the activation technique is possible for the (n,2n) cross section measurement. The reaction product ^{240}Am has a short half-life ($T_{1/2}$ = 50.8 h) and is emitting two strong γ-rays at 888.85 and 987.79 keV. The major problem here is the intense background due to the ^{241}Am natural activity, especially the strong 60 keV γ emission.

3.1   Principle of the measurement

The principle of the method is illustrated in figure 3.1. It consists in two main steps: the sample irradiation and its induced activity measurement achieved directly after the irradiation.
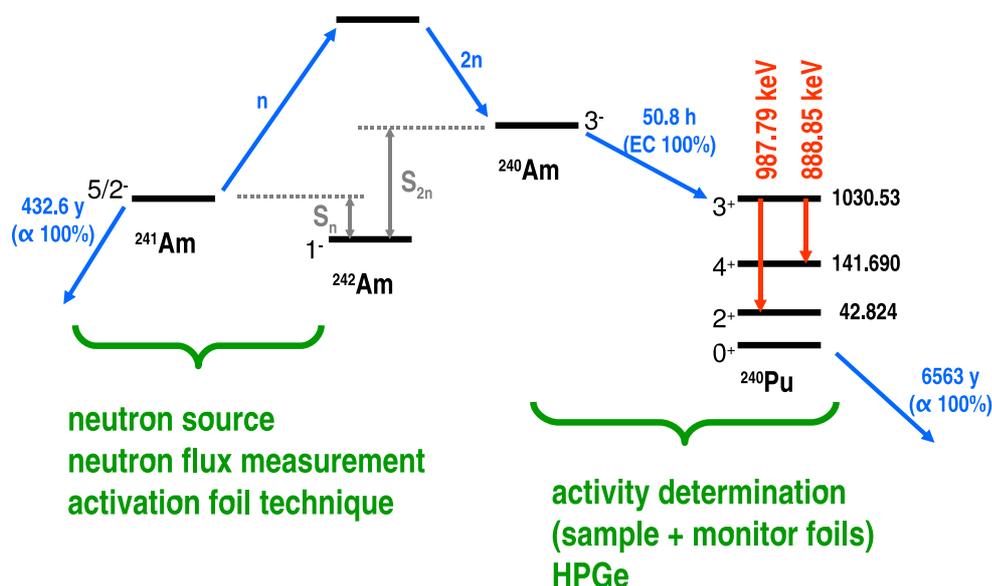
Figure 3.1: Simplified scheme of the ^{241}Am(n,2n)^{240}Am reaction process.

During the irradiation, the ^{242}Am compound nucleus is formed, which then emits two neutrons to give the reaction product ^{240}Am. This latter then decays to

^{240}Pu (EC 100%) with a half-life of 50.8 h. The γ-rays of interest here are from the ^{240}Am decay and from the ^{241}Am natural activity. Table 3.1 summarizes the characteristics of these rays. We can see from this table that the challenge here will be to get rid of the huge background coming from the numerous ^{241}Am rays.

Table 3.1: Relevant gamma and X-rays from the decay radiations of ^{240}Am and ^{241}Am [38, 39].

Nucleus	Half life	E_γ (keV)	I_γ (%)
^{240}Am	50.8(3) h	98.9(1)	1.47(4)
		99.525	18.4(5)
		103.374	29.2(8)
		116.244	3.53(10)
		117.228	6.93(20)
		120.54	2.71(7)
		888.85(5)	24.7(5)
		987.79(6)	72.2(9)
^{241}Am	432.6(6) y	59.5409(1)	35.9(4)
		208.01(3)	7.91×10^{-4}(19)
		322.52(3)	1.52×10^{-4}(4)
		332.35(3)	1.49×10^{-4}(3)
		335.37(3)	4.96×10^{-4}(11)
		368.65(3)	2.17×10^{-4}(5)
		376.65(3)	1.38×10^{-4}(3)
		662.40(2)	3.64×10^{-4}(9)
		722.01(3)	1.96×10^{-4}(4)
		887.3(3)	2.2×10^{-7}(5)

In practice, the cross section itself will be calculated relative to the ^{27}Al(n,α)^{24}Na standard cross section. For this purpose, two aluminium foils were placed before and after the americium sample. We also placed other so-called monitor foils at the same positions (iron, indium, niobium and nickel foils) in order to get the most precise estimate of the neutron flux. This method will be further described in the neutron flux determination part.

3.2   Sample description

The americium dioxide AmO_2 was originally produced by partitioning military plutonium in the Los Alamos (LANL) laboratory. Some of this material was then

transferred to CEA Marcoule in the frame of the FUTURIX/FTA collaboration for purification, before being processed at JRC-ITU Karlsruhe for the sample fabrication.

The samples were prepared by a method especially developed for the present study by JRC-ITU in Karlsruhe. This sol-gel method, which is compared to the conventional powder blending process in Appendix A, is based on the production of porous alumina granules by powder metallurgy. The americium was introduced into the porous particles by infiltration of its nitrate solution. Following drying to eliminate water, and calcination to convert to oxide, the resulting powder was pressed into pellets of 12 mm diameter and 2 mm thickness. The sample weight was on average 400 mg and the average americium content was 40 mg. The americium-alumina composite was then encapsulated into aluminium containers.

The geometry of each sample was examined by X-ray radiography and the americium content determined by calorimetry [40]. The mass of ^{241}Am in the samples was also determined by γ-spectrometry at the IRMM with results agreeing within 2%. Table 3.2 summarizes the characteristics of the 6 samples produced for these measurements.

Table 3.2: The mass and elemental composition of the samples.

sample number	total mass (g)	Al$_2$O$_3$ (g)	^{241}Am content (mg)	Calculated ^{241}Am (wt%)
1	0.342	0.305	32.2±0.1	9.43
2	0.442	0.394	42.2±0.1	9.51
3	0.428	0.382	40.3±0.1	9.42
4	0.435	0.388	41.0±0.1	9.42
5	0.448	0.401	41.2±0.1	9.20
6	0.447	0.399	42.1±0.1	9.42

Figure 3.2 shows a picture of the samples with a scheme of the container and an example of the IRMM X-ray radiography result for one of the samples. This X-ray analysis revealed a shape problem for the sample 5, this latter being slightly truncated on one side. It was then decided not to use this sample for the rest of the measurement campaign.

Figure 3.2: Americium samples and sample holders picture, scheme and X-ray radiograph.

3.3 Irradiation process

3.3.1 Irradiation setup

Monoenergetic neutron source

The irradiations were carried out at the 7 MV Van de Graaff electrostatic accelerator at the IRMM. The neutrons used in these experiments were obtained by hitting deuterium and tritium targets with a deuteron beam. The projectile energies are adjusted in order to get the desired neutron energies via the $^2H(d,n)^3He$ and $^3H(d,n)^4He$ reactions. The energy scale of the accelerator is calibrated with an accuracy of ± 5 keV via a nuclear magnetic resonance system inserted in a 90° bending magnet, using well-known reaction thresholds and resonances .

The neutron production reactions are two-body reactions in which the neutron energy is perfectly defined by the kinematics and the irradiation conditions. This leads to the production of monoenergetic neutrons, but beyond a few MeV projectile energy, other secondary reactions such as $^2H(d,np)^2H$, $^3H(d,np)^3H$ or

^{3}H(d,2n)^{3}He are energetically possible and produce then a continuous energy spectrum, with a monoenergetic peak and some lower energy components in the tail. In reality, the peak energy is quasi-monoenergetic as a result of energy loss of the deuteron in the target and the associated energy straggling.

Two types of targets were used for the irradiations, corresponding to the two reactions already mentioned.

- **Gas target:** this consisted of a deuterium gas target filled under 120 kPa. The target cell was 4 cm in length and 4 cm in diameter with a 5 μm molybdenum entrance window for the separation with the accelerator vacuum tube. The beam stop was achieved by a 1 mm thick tantalum exit window. We used this target with 5.5 and 6.3 MeV deuteron energies to get neutrons respectively at 8.34 and 9.15 MeV.

- **Solid target:** this was a solid state Ti/T target on a silver backing (0.4 mm thick) with a 26 mm diameter. The tritium is diffused into the Ti layer (2 mg/cm^2) at high temperatures until it is saturated at a value of 1.5 T atoms per Ti atom. This target is wobbled and cooled with a jet of compressed air to further aid in the dissipation of heat. We used this target with deuteron energies ranging from 1 to 4 MeV to get neutrons from 16.1 to 20.6 MeV at 0° emission angle and 13.3 MeV at 125°.

Figure 3.3 shows a scheme of both types of targets and table 3.3 summarizes the characteristics of the two corresponding reactions used for the neutron production.

Table 3.3: Characteristics of the neutron production reactions.

Reaction	Q-value (MeV)	break up reaction	threshold (MeV)	neutron energy range (MeV)
^{2}H(d,n)^{3}He	3.269	^{2}H(d,np)^{2}H	4.45	3 - 10
^{3}H(d,n)^{4}He	17.59	^{3}H(d,np)^{3}H	3.71	13 - 21
		^{3}H(d,2n)^{3}He	4.92	

For these two reactions, the main part of the neutron production as well as the higher neutron energy corresponds to the incident beam direction. It is then in this direction (0°) that we placed our americium samples, except for the 13.3 MeV energy point. For this measurement, we used the property of the reaction kinematics in order to get this expected neutron energy. As is shown on figure 3.4, for any deuteron energy, the maximum neutron energy will be at 0°. The emitted neutron energy as well as the flux will then decrease with the increasing emission
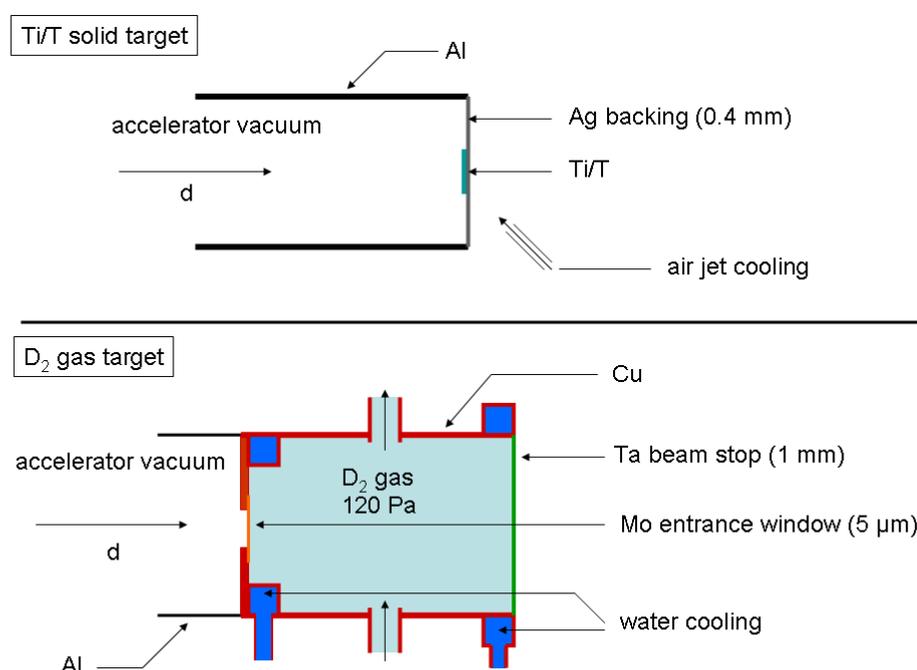
Figure 3.3: Simplified schemes of the gas and solid targets used in the experiments.

angle. We could place the americium sample at the angle of 125° to get the corresponding energy of 13.3 MeV for deuteron energies of 1 to 4 MeV. This value of angle was chosen in order to have a longer irradiation for this sample: while irradiating two samples placed at 0° during 2x2 days one after the other with a deuteron beam of 1 then 2 MeV, we could irradiate the sample at 125° during four days (to compensate for the lower flux) at the same neutron energy but with two different deuteron energies. This 125° angle was the only one corresponding to this compromise, and it was important to find this irradiation solution so as to get an energy point around 14 MeV and then be able to compare our results with the previous measurements mainly existing at this energy.

Irradiation geometry

For all measurements, the sample was mounted in a specially prepared lightweight aluminium frame in order to reduce the material amount around the irradiation. The frame allowed to attach foils of Al, Fe, In, Nb and Ni (13 mm diameter) on both sides of the sample to monitor the neutron flux and to account
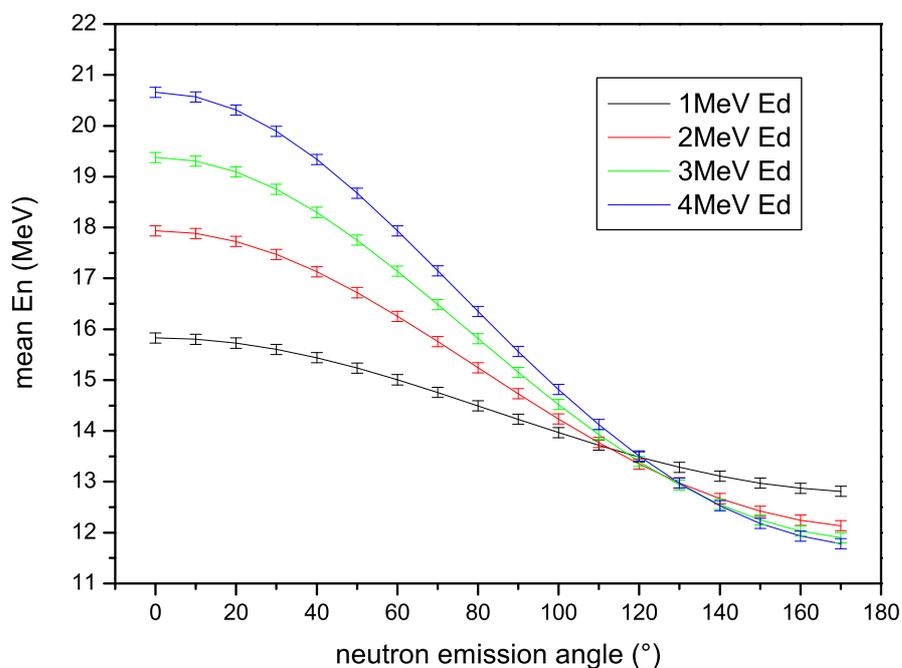
Figure 3.4: Mean E$_n$ of the produced neutrons as a function of the emission angle calculated with EnergySet [41], case of the Ti/T solid target for 4 different deuteron energies.

for its variation with distance. The distance between the monitor foils and the sample was 3 mm in the front and 10 mm at the back.

For the irradiations with the gas target, the sample was placed at 1.5 cm from the target, whereas this distance was about 2 cm for the irradiations with the solid target. The special irradiation at 125° was achieved with a sample placed at 3.9 cm from the target. During each 2-days long irradiation, a BF$_3$ counter operated in multichannel scaling acquisition mode was used to record the time profile of the neutron flux. Figure 3.5 shows a picture of the irradiation setup for the case of the solid target, as well as a simplified scheme of the geometry, where we can see the deuteron beam hitting the Ti/T target to produce the neutrons that will irradiate the sample and the monitor foils stack.
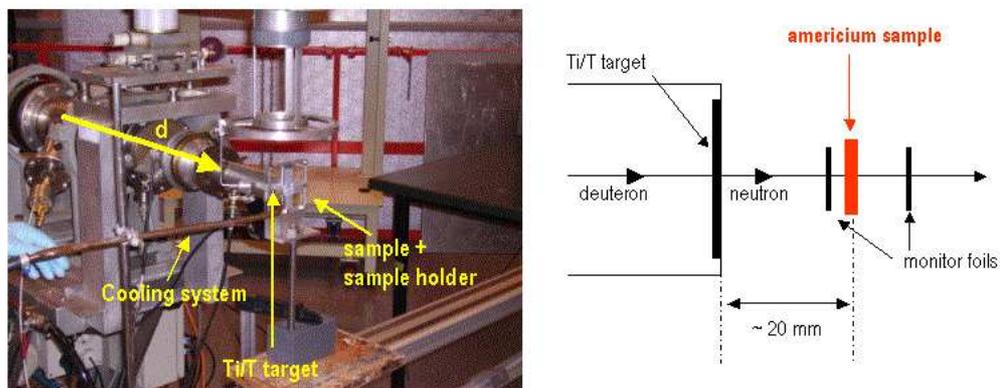
Figure 3.5: Picture of the irradiation geometry (left) and a schematic view of the setup (right).

Summary of performed irradiations

The measurements were performed in four sessions from february 2007 to March 2008, each of them lasting about one week. These sessions were separated by at least a few months in order to be able to use the irradiated samples again without having any issue with some activity remnant coming from the previous irradiation.

The first session occurred from the 26th of February to the 5th of March 2007. Within this week we achieved the two lower energy measurements (with neutrons of 8.34 and 9.15 MeV) using the deuterium gas target with deuteron energies of 5.5 and 6.3 MeV respectively. For this measurement, four samples were irradiated, two of them for the real measurement, the two other ones being irradiated with an empty gas cell for background estimation.

The second session took place from the 18th to the 25th of June 2007. Four samples were irradiated using the solid Ti/T target and deuterons of 2, 3 and 4 MeV to get neutrons at 17.9, 19.36 and 20.61 MeV. The fourth sample was irradiated at 125° to get the point at 13.3 MeV neutron energy with 2 and 3 MeV deuterons.

A third two-weeks long measurement session was achieved from the 3rd to the 16th of December 2007. The same solid target was used with deuteron energies of 1, 1.5, 2 and 3.5 MeV to get neutrons of 16.1, 17.16, 17.9 and 19.95 MeV, as welle as another measurement with 13.3 MeV neutrons with a sample placed at 125°.

The last measurement session took place from the 11th to the 17th of March 2008. This time, a new solid state Ti/T target was used with the same characteristics as the other one. We irradiated three samples with 1 and 2 MeV deuteron energies to get neutrons at 16.1, 17.9 and 13.3 MeV.

Table 3.4 summarizes the characteristics of the irradiations performed during the four measurement sessions, showing the sample number, the deuteron and neutron energies, the type of target used, the position of the sample, the average deuteron beam current and the irradiation time.

Table 3.4: Summary of performed irradiations.

Session	Target	Sample number	Sample position	E_d (MeV)	E_n (MeV)	Average beam current (μA)
Feb. 2007	gas in	1	0°	5.5	8.34	5.6
	gas out	4	0°	5.5		6.7
	gas in	3	0°	6.3	9.15	6.1
	gas out	6	0°	6.3		6.2
June 2007	Ti/T 1	1	0°	4	20.61	3.5
		2	0°	3	19.36	3.0
		3	125°	2-3	13.33	3-3.3
		4	0°	2	17.9	3.3
Dec. 2007	Ti/T 1	1	0°	2	17.9	10
		2	0°	1.5	17.16	11
		3	0°	1	16.1	16
		4	125°	1-3.5	13.33	14-16
		6	0°	3.5	19.95	14
March 2008	Ti/T 2	1	0°	2	17.9	23
		3	125°	1-2	13.33	20-23
		4	0°	1	16.1	20

3.3.2   Neutron energy and flux determination

The mean neutron energy and yield distributions as a function of deuteron energy and emission angle for the primary neutrons of the D(d,n)^{3}He and T(d,n)^{4}He reactions were calculated by the code Energyset [41] which is based on the reaction cross section evaluations of ref. [42] and energy loss estimates with stopping powers of ref. [43] to achieve the kinematics calculations of the corresponding reactions. This program, coupled to the TARGET code [44], takes into account:

- the angular distribution of the $D(d,n)^3He$ and $T(d,n)^4He$ reactions,

- the production of the neutrons in the space of the gas cell,

- the distance between the sample and the beam stop,

- the breakup of the deuterons as well as other secondary reactions.

During the irradiations, a BF_3 counter was used to record the time profile of the neutron flux. This time profile allows for a correction that is important when beam current variations are substantial. Figure 3.6 shows four typical examples of very different beam conditions we met during the four measurement sessions. The first spectrum corresponds to a gas cell measurement from February 2007 with very good beam stability. The second one shows the typical neutron beam we had for the June 2007 measurements, with very low intensity but good stability. For the third spectrum corresponding to a measurement achieved in December 2007, the beam loss during the first ten hours corresponds to an obvious beam problem during the first night irradiation, whereas the last spectrum from March 2008 shows a very intense but quite unstable neutron beam. Further details on the corresponding correction calculations are given in the next chapter concerning the data analysis.

The presence of low-energy secondary neutrons necessitated the application of significant corrections to the measured activation yields for the reactions with low threshold energies. In this work, the determination of this flux components was done using metal monitor foils of Al, Fe, In, Nb and Ni in sandwich geometry in combination with previously measured time-of-flight spectra. The induced activity of the foils was measured off-line after the irradiation, and the calculation of the derived correction is also further explained in the next chapter.

The monitor foils reactions used for the unfolding were: $^{27}Al(n,p)^{27}Mg$, $^{56}Fe(n,p)^{56}Mn$, $^{115}In(n,n')^{115m}In$, $^{27}Al(n,\alpha)^{24}Na$, $^{93}Nb(n,2n)^{92m}Nb$, $^{58}Ni(n,p)^{58m+g}Co$. The cross section data for these dosimetry reactions were taken from Smith *et al.* [45] for the $^{115}In(n,n')^{115m}In$ reaction, from Wagner *et al.* [46] for the $^{27}Al(n,\alpha)^{24}Na$ and the $^{93}Nb(n,2n)^{92m}Nb$ reactions, and from the ENDF/B-VI library [47] for the remaining ones. Figure 3.7 shows the different monitor foils evaluated cross sections and table 3.5 summarizes the characteristics of these reactions.
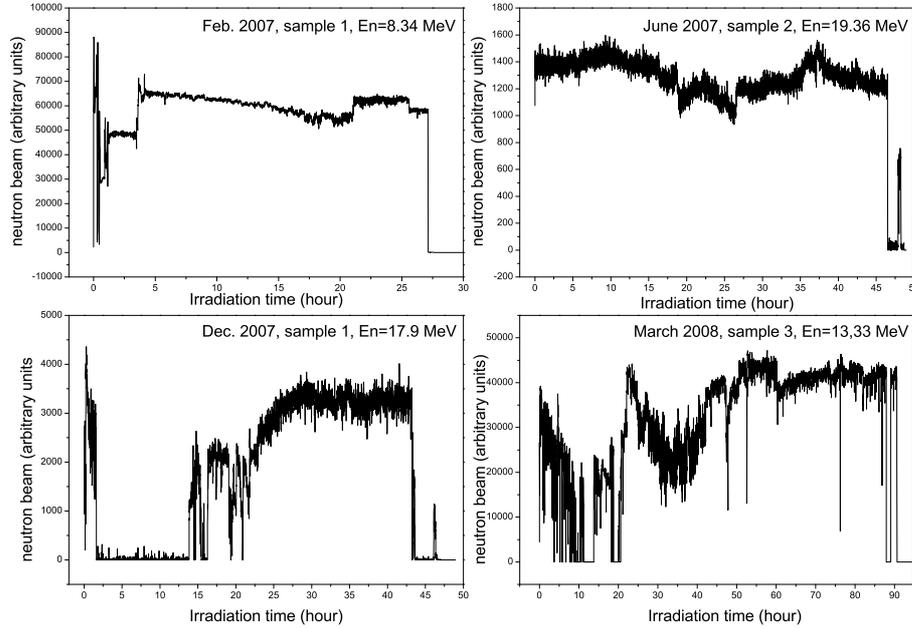
Figure 3.6: Typical neutron beam time profiles.

Table 3.5: The β-decay properties of the monitor reactions used for the neutron flux normalization (from references [48, 49, 50, 51, 52, 53]).

Reaction	Half-life of product	Q-value (MeV)	E_γ (keV)	Intensity (%)
^{27}Al(n,p)^{27}Mg	9.458(12) m	-1.828	843.8	71.8(4)
^{56}Fe(n,p)^{56}Mn	2.5789(1) h	-2.913	846.8	98.9(3)
^{115}In(n,n')^{115m}In	4.486(4) h	0.336	336.2	46(2)
^{27}Al(n,α)^{24}Na	14.997(12) h	-3.132	1368.6	99.9936(15)
^{93}Nb(n,2n)^{92m}Nb	10.15(2) d	-8.967	934.4	99.07(4)
^{58}Ni(n,p)^{58}Co	70.86(7) d	0.401	810.8	99.45(1)

3.4   Induced activity measurements

3.4.1   Detector setup description

After the irradiation, the induced activity was measured off-line by standard γ-ray spectrometry using a high-purity germanium detector (HPGe). The data acquisi-
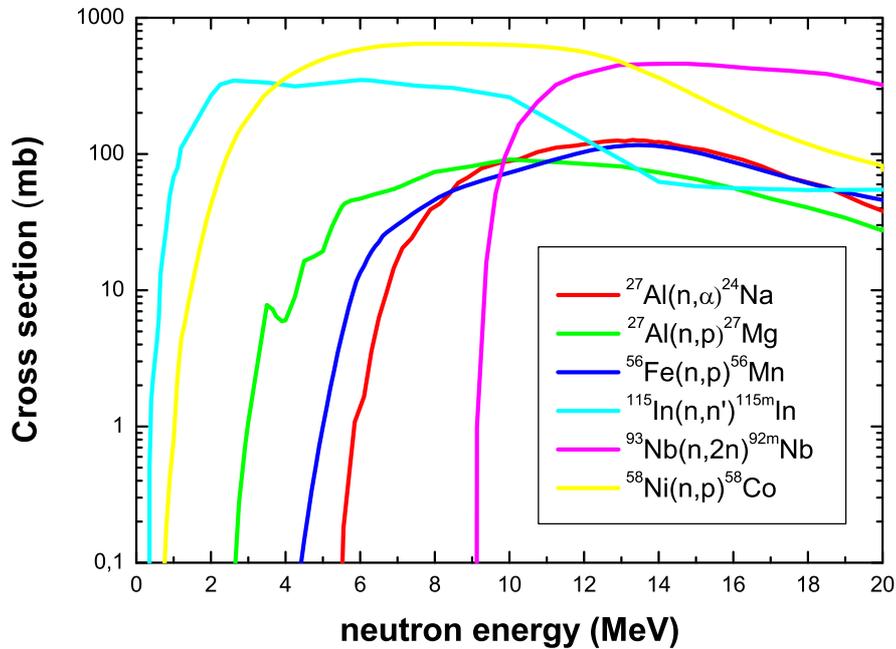
Figure 3.7: Evaluated monitor reaction cross sections used in this work, data from ref. [45, 46, 47].

tion was controlled by the Maestro system supplied by Ortec, and the γ-ray spectra were analyzed using the software package Genie2000 of Canberra. The decay data for the monitor reactions were taken from references [48, 49, 50, 51, 52, 53] and are given in table 3.5 along with the reaction Q-values [54].The decay data for ^{240}Am and ^{241}Am used for the data analysis were taken from references [38, 39] and are given in table 3.1.

A Pb/Sn/Cu shielding, with respectively 5/3/3 mm thicknesses, was used to reduce the important natural activity from the ^{241}Am decay in order to limit the dead time of the system to less than 15% (between 7 and 15% typically, for a sample directly placed on top of the shielding). Figure 3.8 shows the gamma-ray attenuation corresponding to the shielding layers and their adopted thicknesses, which were chosen as a compromise between the strong 60 keV line suppression and a good transmission at higher energies.

The correctness of the dead time given by the acquisition system was verified by a comparison of the counting rates from a ^{60}Co standard source with and with-
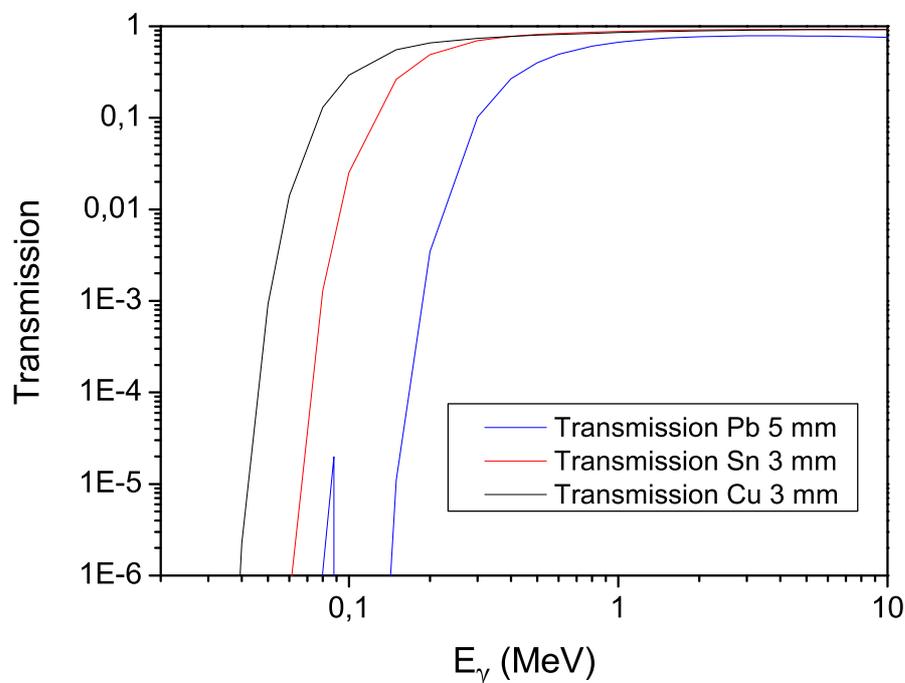
Figure 3.8: Simulated gamma-ray attenuation of the used shielding materials.

out an Am sample. The detector was additionally shielded from the side with a 10 mm thick Cu cylinder to avoid detection of scattered gamma rays. In order to get maximum count rates and thereby reasonable counting statistics, the monitor foils were placed directly on the detector cap, without the shielding layers previously mentioned. Figure 3.9 shows a picture of the detection system with part of the shielding (the Cu cylinder) together with a scheme of the setup. The whole setup was enclosed within 10 cm thick Pb walls and made accessible by sliding Pb doors with the same thickness.

3.4.2   Detector calibration

The sample activities were determined using the counts in the full energy peak of the γ-ray transition. For this it was important to know the absolute peak efficiency and the energy calibration. Concerning the energy calibration, several single and multi γ-ray standard point sources were used, such as ^{241}Am ($E_\gamma = 59.5$ keV),
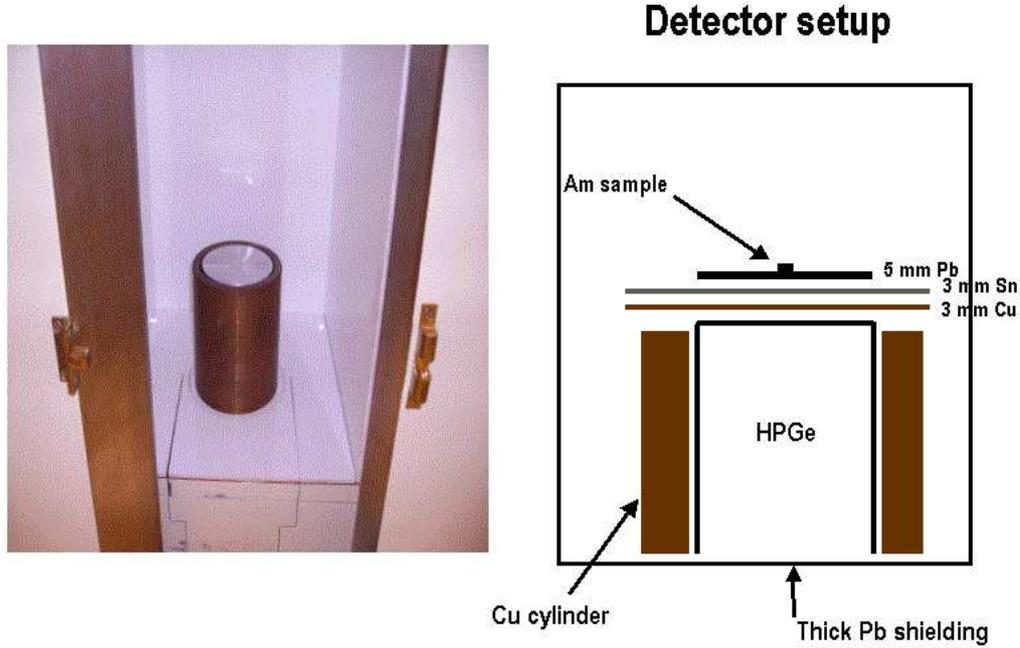
Figure 3.9: Detection setup picture and simplified scheme.

^{109}Cd (E_γ = 88 keV), ^{57}Co (E_γ = 122.1 and 136.5 keV), ^{137}Cs (E_γ = 661.66 keV), ^{54}Mn (E_γ = 834.8 keV) and ^{65}Zn (E_γ = 1115.5 keV). The calibration was done for different radial positions and detector-source distances.

The efficiency of the detection setup was determined by a Monte Carlo simulation using the code MCNP5 [55] and taking into account the entire detection geometry. The results of this simulation were compared with measured values and efficiency curves by fitting experimental points with polynomial logarithmic functions [56]:

$$\ln \epsilon = \sum_{i=0}^{n} a_i (\ln E)^i \tag{3.1}$$

The experimental full energy peak (FEP) efficiencies were measured using the same calibration sources as mentioned before, the characteristics of which are summarized in table 3.6. They were then calculated using the formula

$$\epsilon_{FEP} = \frac{N}{tAI} \tag{3.2}$$

with N the number of counts in the peak, t the measuring time, A the source activity and I the γ-ray intensity. The measuring time for each source was set so that

each peak contains more than 10^4 counts. The combined standard uncertainty of the measured values was calculated as a quadratic sum of individual uncertainties of counting statistics, standard source γ flux and experimental conditions. Figure 3.10 shows the polynomial logarithmic fit of the experimental points.

Table 3.6: Calibration sources characteristics and corresponding measured efficiencies.

Radionuclide	Energy (keV)	Intensity (%)	Measured efficiency (%)
^{241}Am	59.5409(1)	35.9(4)	2.52(5)
^{109}Cd	88.0336(1)	3.70(10)	8.89(18)
^{57}Co	122.06065(12)	85.60(17)	11.49(26)
	136.47356(29)	10.68(8)	11.24(36)
^{137}Cs	661.657(3)	85.10(20)	2.63(5)
^{54}Mn	834.843(3)	99.9760(10)	2.39(5)
^{65}Zn	1115.539(2)	56.60(22)	1.89(0.6)
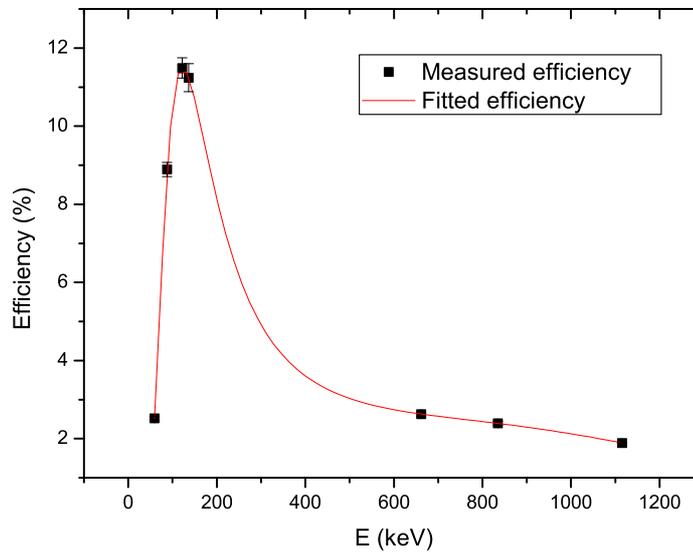
Figure 3.10: Polynomial logarithmic fit of the measured detector efficiency.

Concerning the geometry description in the MCNP simulation, we used the specifications provided by the supplier : we used here the 100 % HPGe coaxial

detector ORTEC model 38-P40712A. The detector construction has been checked by means of radiography, which shows that there were no displacements during transport and installation. The detector geometry parameters of the simulation have been optimized in order to obtain agreement between measurements and simulations within the uncertainty limits of 2-3 %.

The correction factors and uncertainties estimations related to this activity measurement, either coming from the efficiency calculation or from the detection itself (photon absorption, disk shape of the samples, coincidence summings of gamma rays, etc.) are further explained in the next chapter concerning the data analysis.

3.4.3 Activity measurement

Figure 3.11 shows typical spectra obtained for the sample activity measurement. These spectra correspond to the measurement of sample activity before and after irradiation. The increased background under the peaks in the higher energy part concerns Compton events from the ^{24}Na activity produced by the ^{27}Al(n,α) reaction on the container and Al$_2$O$_3$ matrix.
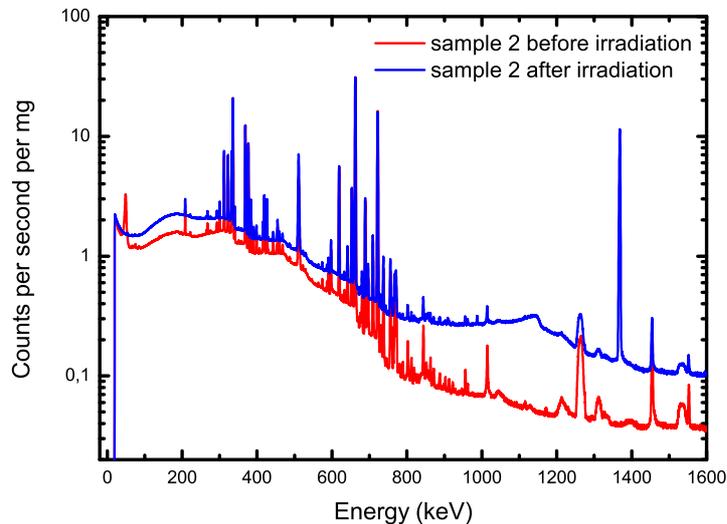
Figure 3.11: Comparison of typical americium activity spectra measured before and after the irradiation.

For the two main gamma rays emitted in the decay of ^{240}Am figure 3.12 clearly shows that the peak corresponding to the energy of 888.85 keV is contaminated by the natural activity of the sample itself while the gamma-ray with 987.79 keV is free from interference by the sample activity. The intensities of both the 888.85 and 987.79 keV gamma lines were measured as a function of the cooling time after irradiation. Fitting the corresponding half life confirmed that the 987.79 keV gamma-line was free of interference since the measured decay curve closely corresponded to that of ^{240}Am. As anticipated this was not the case for the 888.85 keV gamma-ray.
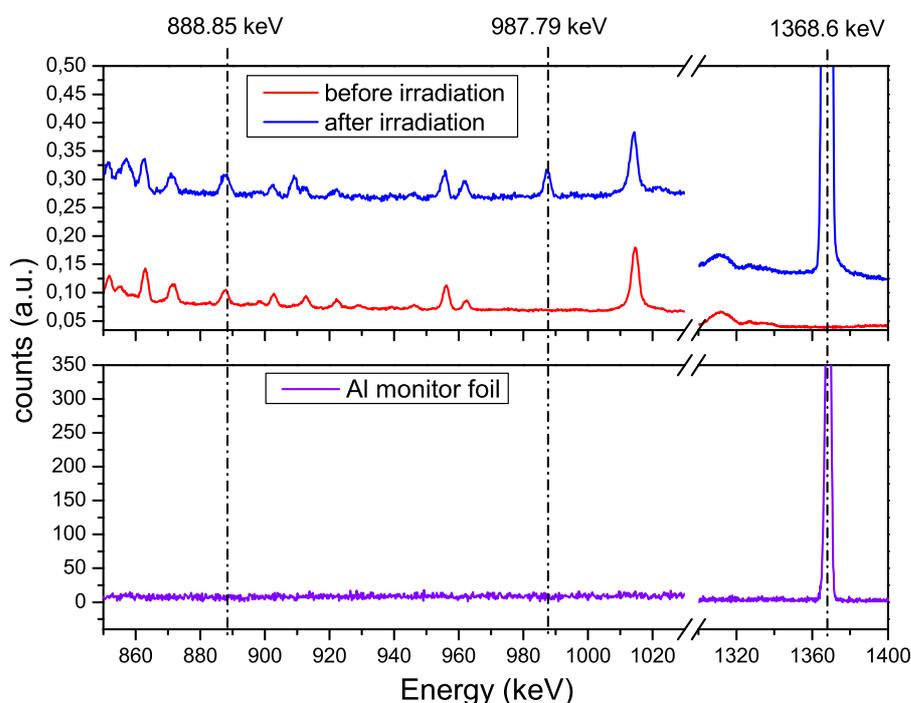
Figure 3.12: Zoom of the typical activity spectra obtained for the Am sample and Al monitor foil in the relevant energy range.

Chapter 4

The ^{241}Am(n,2n)^{240}Am reaction cross section: analysis and results

4.1 Data analysis procedure

The reaction cross section is here determined by measuring the ^{240}Am induced activity. The production rate of this nuclide is given by:

$$\frac{dN(t)}{dt} = \int_E n\sigma(E)\Phi(E,t)dE - \lambda N(t) \tag{4.1}$$

where $N(t)$ is the number of product nuclei, n the number of target nuclei that is assumed not to vary during the irradiation, σ the reaction cross section, λ the decay constant and $\Phi(E,t)$ the time and energy dependent neutron flux. In the ideal case of a constant mono-energetic flux where

$$\Phi(E,t) = \Phi_0\delta(E - E_0) \tag{4.2}$$

solving equation (4.1) with the initial condition $N(t = 0) = 0$ gives at the irradiation time t_r the number of activated nuclei

$$N_r = N(t_r) = \frac{n\sigma\Phi_0}{\lambda}f_r \tag{4.3}$$

with

$$f_r = 1 - e^{-\lambda t_r} \tag{4.4}$$

the irradiation time factor.

For the second step of the experiment, i.e the activity measurement, we can write the number of events S registered in the HPGe detector during the successive measurement sessions, as illustrated in figure 4.1, as

$$S = \sum_i S_i = \lambda N_r I \epsilon f_\Sigma \qquad (4.5)$$

with

$$f_\Sigma = \frac{1}{\lambda} \sum_i e^{-\lambda t_{d_i}}(1 - e^{-\lambda t_{m_i}}) \qquad (4.6)$$

the time factor taking into account the different measurements that last a time t_{m_i} and start after the time t_{d_i} relative to the end of irradiation, I the γ-ray emission probability (or intensity) and ϵ the absolute peak efficiency of the detector for the
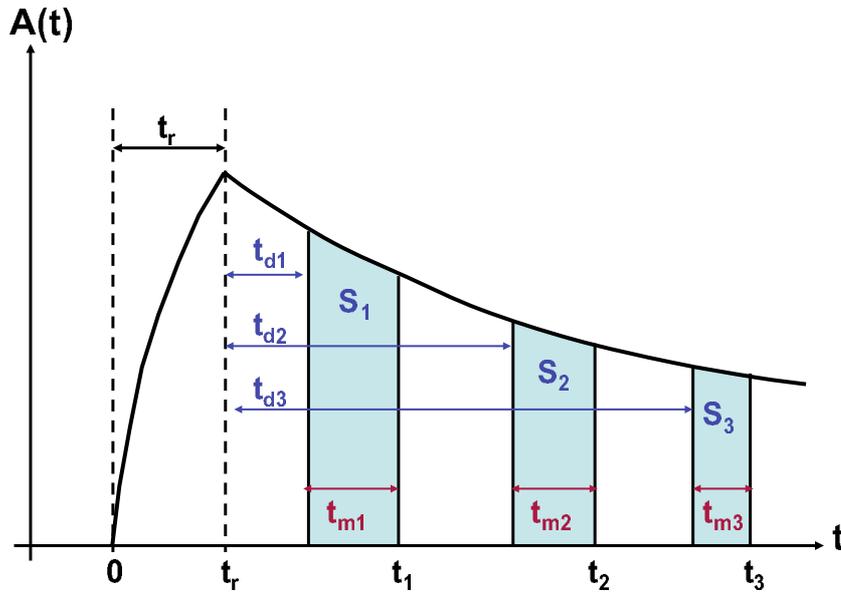
Figure 4.1: Schematic view of the successive activity measurements following an irradiation as a function of time.

By substituting N_r from equation (4.3), we get

$$S = n\sigma\Phi_0 f_r I \epsilon f_\Sigma \qquad (4.7)$$

The induced activity measurements were achieved in several successive sessions for two main reasons. First, it permitted us to calculate the half life and verify its correspondance to the one of ^{240}Am. Then, it was necessary to interrupt the measurements at different intervals to be able to measure the induced activities

of the monitor foils. Measuring in such successive sessions enabled both this and the accumulation of good statistics for the americium sample.

The ^{241}Am(n,2n) reaction cross section was determined relative to the ^{27}Al(n,α)^{24}Na monitor cross section calculated with the same formulas applied to aluminium. Equation (4.7) shows explicitly how the ratio of observed counts $S_{\mathrm{Am}}/S_{\mathrm{Al}}$ is proportional to the cross section ratio $\sigma_{\mathrm{Am}}/\sigma_{\mathrm{Al}}$ and inversion of the expression leads to the following expression for the americium cross section:

$$\sigma_{\mathrm{Am}} = \sigma_{\mathrm{Al}} \frac{S_{\mathrm{Am}}}{S_{\mathrm{Al}}} \frac{\left[I\epsilon f_{\Sigma} f_r n \Phi_0\right]_{\mathrm{Al}}}{\left[I\epsilon f_{\Sigma} f_r n \Phi_0\right]_{\mathrm{Am}}} \tag{4.8}$$

For an actual experiment, corrections are needed to account for deviations from the ideal case both for the irradiations and for the activity determinations. Such corrections are further detailed in the next paragraph and are taken into account in the cross section calculation as a product of several correction factors C_k applied to americium and aluminium. therefore the cross section was finally determined using the expression:

$$\sigma_{\mathrm{Am}} = \sigma_{\mathrm{Al}} \frac{S_{\mathrm{Am}}}{S_{\mathrm{Al}}} \frac{\left[I\epsilon f_{\Sigma} f_r n \Phi_0\right]_{\mathrm{Al}}}{\left[I\epsilon f_{\Sigma} f_r n \Phi_0\right]_{\mathrm{Am}}} \cdot \prod_k \frac{C_{k,\mathrm{Am}}}{C_{k,\mathrm{Al}}}. \tag{4.9}$$

4.2 Corrections calculations

4.2.1 Corrections related to the irradiation process

For an actual experiment corrections are needed to account for deviations from the ideal case both for the irradiations and for the activity determinations. The corrections C_k appear in equation (4.9) and were described in considerable detail for measurements at IRMM in references [57, 58, 59, 60]. They are applied for both the americium sample and the aluminium monitors and are either calculated in a rigorous way or small enough to be treated as a perturbation.

Determination of Φ_0

For the irradiations, deuteron straggling in the target, the angle dependence of the neutron yield and energy, the close geometry and multiple scattering of the neutron result in energy distributions of the primary component of the flux that differ

for the monitor foils and the sample because of the flux attenuation between their different distances from the neutron source. This may be accounted for by simple means in very light weight arrangements [59] or by more elaborate modeling using Monte Carlo simulations. The latter is essential for substantial sample masses and sizes [58].

Here, the ratio of the flux $\Phi_{0,Al}/\Phi_{0,Am}$ for the primary neutron component was determined by simulations of the flux attenuation using MCNPX [61]. A detailed description of the irradiation geometry was made for each irradiation energy, including the targets, the sample, the monitor foils and the sample holder. The neutron source description, i.e. the energy and angular distribution of the incident neutron flux, was determined using a special feature of EnergySet. This code can actually be coupled to the SRIM software [62] in order to produce a file describing the neutron distribution at the exit of the target in the adequate format corresponfing to the MCNPX source input. This enables to take into account the target characteristics, the deuteron straggling in the target and the angle and energy dependence of the neutron flux.

The shape of the flux attenuation with distance r is assumed to be in A/r^b, with $b = 2$ corresponding to the ideal case of a point source. The flux ratio is then equal to $(r_{Am}/r_{Al})^b$, with the two distances well known. From the simulation of the setup geometry, we can get the neutron flux as a function of the distance r from the target. Fitting this with the assumed function gave a factor b describing the flux attenuation ranging from 1.78 to 1.84, depending on the neutron energy. Figure 4.2 shows the fit of the flux attenuation in the case of the solid Ti/T target with $E_n = 17.9$ MeV.

Flux fluctuation correction

The impact of fluctuations of the deuteron beam current during the two days long irradiations were evaluated using the number of neutrons recorded by a BF$_3$ counter every minute (see figure 3.6). If we divide the total irradiation time t_r into m small time intervals Δt, the contribution for one single bin will be proportional to $\Phi_i(1 - e^{-\lambda\Delta t})$, and the induced decay proportional to $e^{-\lambda(m-i)\Delta t}$. The correction factor C_{flux} is then calculated as

$$C_{\text{flux}} = \frac{\bar{\Phi}(1 - e^{-\lambda t_r})}{\sum_{i=1}^{m} \Phi_i(1 - e^{-\lambda\Delta t})e^{-\lambda(m-i)\Delta t}} \quad (4.10)$$

where $\bar{\Phi} = \sum \Phi_i/m$ is the average flux during the irradiation. The value of this correction factor ranges from 0.1 to 8.3% for the Am sample and from 0.7 to 31% for the Al foils, as can be seen in table 4.1, and is strongly depending on the beam
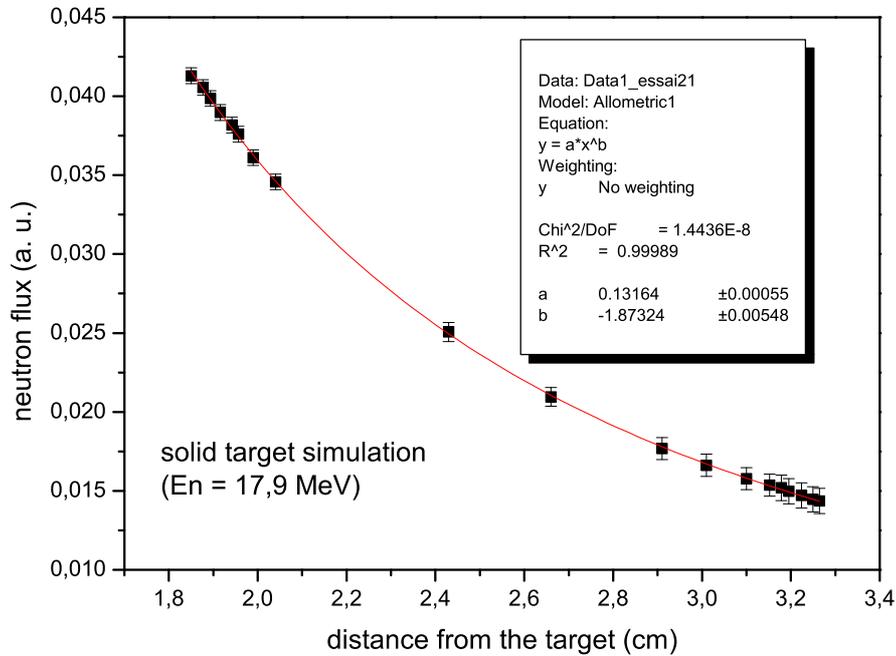
Figure 4.2: Flux attenuation fit, case of the solid Ti/T target with $E_n = 17.9$ MeV.

stability condition during the two-day long irradiations. Since the time bins are very small, the correction can be considered exact and the associated uncertainty can be neglected.

Low energy neutrons correction

While a proper choice of the structural materials for the entrance window and the beam stop as well as the quality of the deuterium gas help to obtain a clean neutron spectrum, background corrections from lower energy neutrons are unavoidable [63]. Actually these neutrons, mainly coming from secondary target reactions, were here evaluated using previously measured time-of-flight spectra of the neutron beam [60] combined with the so-called spectral index method [64]. A cutoff energy E_c for each investigated secondary target reaction is defined below the quasi-monoenergetic neutron peak energy. The position of this cutoff varies depending on the incident deuteron energy and the reaction in question. The intensities of low energy neutrons vary depending on the irradiation history of the

target (deuterium build-up, oxidation, carbon deposits, tritium loss). Therefore, the time-of-flight spectrum is divided in several groups for which the intensities relative to the primary neutrons are adjusted on the basis of the activities found in the monitor foils. Figure 4.3 shows the previously measured Time-Of-Flight spectra corresponding to the use of the Ti/T solid target with deuteron energies of 2, 3 and 4 MeV.
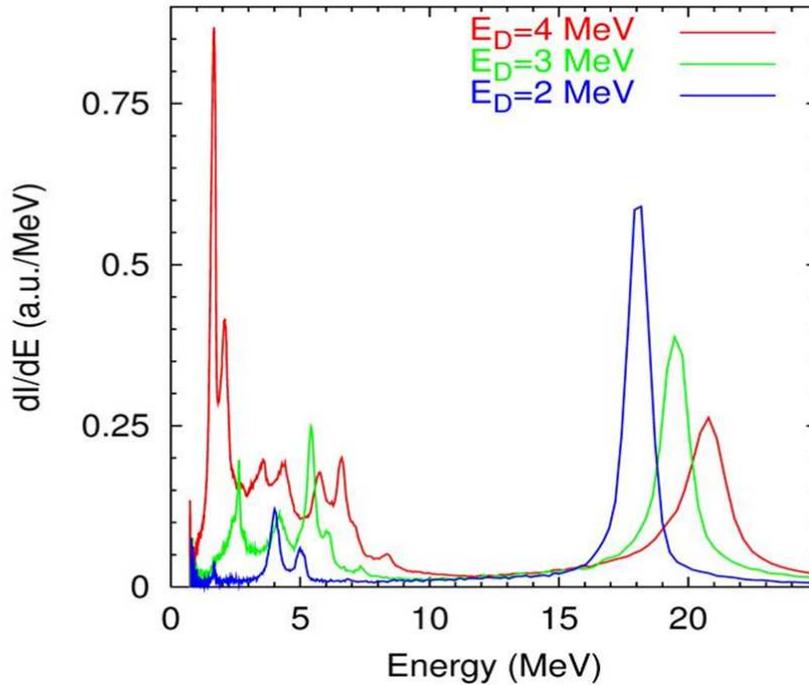
Figure 4.3: Previously measured TOF spectra for deuterons with 2, 3 and 4 MeV hitting the Ti/T solid target.

The correction factor C_{low} is then calculated by forming the ratio of the sample activities produced by neutrons below the cutoff energy versus those produced by the entire neutron spectrum [57]. Both of these yields are calculated by integrating the product of the spectrum shape with assumed cross sections for the considered reactions (see figure 3.7. The correction factor is then derived from the expression

$$C_{\text{low}} = 1 - \frac{\int_0^{E_c} \Phi(E)\sigma(E)dE}{\int_0^{\infty} \Phi(E)\sigma(E)dE}. \tag{4.11}$$

The integrals were solved numerically by interpolating the neutron spectrum and the excitation function to the same energy grid.

The values of this correction factor are shown in table 4.1 and range from 0.0 to 11.5% for the Am sample and from 0.0 to 17% for the Al foils. It is important to note that this factor varies in the same way for both the Am sample and the Al foils. Thus the ratio of the factors ranges only from 0.0 to 6%.

Table 4.1: Flux fluctuation C_{flux} and low energy neutrons C_{low} correction factors for each neutron energy.

Energy	C_{flux}		C_{low}	
(MeV)	Am	Al	Am	Al
8.34	0.9974	0.9925	1	1
9.15	1.0731	1.3117	1	1
13.33	0.9168	0.8288	1	1
16.10	1.0749	1.2335	1	1
17.16	0.9987	0.9878	0.998	0.997
17.90	0.969	0.933	0.998	0.997
19.36	1.0061	1.0157	0.941	0.926
19.95	0.9822	0.9433	0.922	0.891
20.61	0.9938	0.982	0.885	0.832

Case of the gas target

In the case of the irradiations using a gas target, i.e for the two lower energy points, we calculated the background subtraction by simply comparing the gas-in and gas-out induced activities using the formula

$$C_{\text{gas}} = 1 - \frac{A_{\text{out}} t_{\text{out}} q_{\text{in}} m_{\text{in}} (1 - e^{-\lambda t_{in}})}{A_{\text{in}} t_{\text{in}} q_{\text{out}} m_{\text{out}} (1 - e^{-\lambda t_{out}})}. \tag{4.12}$$

with A the measured activity, t the irradiation time, q the integrated beam current and m the sample mass.

The corresponding correction was very small and neglected for the cross section calculation. In addition, an estimate of the deuteron breakup contribution was made using the energy distribution and intensity data of reference [65]. This too turned out to be negligible on account of the low deuteron energy and the reaction thresholds.

4.2.2   Corrections related to the activity measurement

Most of the corrections related to the activity measurement have been lumped together in the detection efficiency estimation by Monte Carlo simulation. Corrections for photon absorption, including the disk shape of the samples and monitor foils, were calculated using the same MCNP5 simulation of the detection geometry. These corrections have been incorporated in the efficiency ϵ and were estimated to 0.2% and 1.3% respectively.

Coincidence summings of gamma rays also occurred for some of the monitor reactions, and had to be corrected for using well-known methods described in reference [66] and detailed knowledge of individual gamma ray decay schemes obtained from ref. [67]. This correction is as high as 25.4% for the ^{27}Al(n,α) ray at 1368.6 keV, 0.3% for the ^{27}Al(n,p) ray at 843.8 keV, 13.5% for the ^{58}Ni(n,p) ray at 810.8 keV, 0.4% for the ^{93}Nb(n,2n) ray at 934.4 keV and 9.9% for the ^{56}Fe(n,p) ray at 846.8 keV.

4.3   Estimation of the uncertainties and their correlations

This section will present the method we employed to estimate all the uncertainties and correlations coming from each term of equation (4.9) used to calculate the cross sections σ_{Am}. This formula can be seen as a function of k independent parameters a_k:

$$\sigma_{\text{Am}} = f(a_k) = \prod_k a_k \tag{4.13}$$

The theoretical formulation of the 9 x 9 covariance matrix for our 9 cross section measurements is then:

$$\mathbf{C}_{\sigma_{Am}} = \sum_k \left[\left(\frac{\partial \sigma_{Am}}{\partial a_k} \right) \mathbf{C}_{a_k} \left(\frac{\partial \sigma_{Am}}{\partial a_k} \right)^T \right] \tag{4.14}$$

The goal will then be the determination of each covariance components $\mathbf{C}_{a_k}$.

In practice, this was done as follows. First, we identified the factors a_k in equation (4.9), lumping strongly correlated terms together in a single factor a_k, independent from the other factors so that eq. (4.14) holds. Then for each factor a_k we determined the total uncertainty for all 9 energy points as detailed in section 4.3.1 and we evaluated the correlations between each of our 9 energy points, as explained in section 4.3.2. It is important to mention that the term "correlation" in

section 4.3.1 refers to the correlations between the terms of formula (4.9) at one given energy, whereas the "correlations" in section 4.3.2 refer to the correlations between the different energy points.

4.3.1 Uncertainties calculation

All possible uncertainties have been evaluated, and table 4.2 only shows the ones above 0.1%. The major uncertainty comes from the detected counts S_{Am}, ranging from 1.3 to 6.3%, and S_{Al}, ranging from 0.7 to 2%. This can be explained by the low count rate due to both a large background from the ^{241}Am natural activity and a decreasing reaction cross section with energy. We used six different Am samples for nine energy points. The uncertainty of 0.3% on the americium mass was taken into account. The Al samples, with an uncertainty on the mass of 0.1%, were different for all energy points. The uncertainties for the aluminium cross section σ_{Al} were taken from reference [46].

The negligible uncertainties (below 0.1%) correspond to the uncertainty on the γ-ray intensity for aluminium I_{Al}, the decay constant λ propagated to the corresponding time factors f_{Σ} and f_r of the Al monitor reaction, and for the ratio $C_{flux,Am}/C_{flux,Al}$. The relative flux ratio $\Phi_{0,Al}/\Phi_{0,Am}$ was estimated within good agreement both with an analytical approximation and with Monte Carlo simulations and its uncertainty was also neglected.

The total uncertainties of the measured cross sections shown in table 4.3 were obtained by summing up all the individual uncertainties according to the law of error propagation for independent multiplicative variables. It is then important to identify the possibly correlated terms from equation (4.9) at one given energy. All of the terms previously mentioned are uncorrelated, thus the only correlations will come from f_{Σ} and f_r for americium, $C_{low,Am}$ and $C_{low,Al}$ and finally ϵ_{Am} and ϵ_{Al}. Here is a summary of the different distinctions to be made for a proper uncertainty calculation:

neglected uncertainties: I_{Al}, $(f_{\Sigma}f_r)_{Al}$, $\Phi_{0,Al}/\Phi_{0,Am}$, $C_{flux,Am}/C_{flux,Al}$.

uncorrelated terms: σ_{Al}, S_{Am}, S_{Al}, I_{Am}, n_{Am}, n_{Al}.

correlated terms: $(f_{\Sigma}f_r)_{Am}$, $\epsilon_{Am}/\epsilon_{Al}$, $C_{low,Am}/C_{low,Al}$.

The contribution of the uncertainty on λ for Am to the corresponding time factors f_{Σ} and f_r was taken into account using the error propagation law for both of these terms. The resulting uncertainty on their product is then slightly higher because of the covariance, since a 100% correlation was estimated between them,

due to the fact that the uncertainty is coming from the one on λ, which is the same for f_Σ and f_r. The resulting total uncertainty on $(f_\Sigma f_r)_{\text{Am}}$ is ranging from 0.4 to 0.9% for the different energy points because of the different irradiation and decay times.

We have estimated the uncertainty on the ratio $C_{\text{low,Am}}/C_{\text{low,Al}}$ at 0.3 to 1.4% depending on the energy. This uncertainty mainly originates from the knowledge of the low component of the neutron spectrum, which is in common for $C_{\text{low,Am}}$ and $C_{\text{low,Al}}$ at one certain energy. That is why a strong correlation of 80% was chosen in order to get a relevant estimate of the uncertainty on the ratio.

For the ratio of the efficiencies $\epsilon_{\text{Am}}/\epsilon_{\text{Al}}$, the uncertainty on each efficiency was estimated at 3%, based on the comparison of Monte Carlo simulations and point source measurements. A correlation between these two efficiencies had to be considered due to the fact that the same geometry description was used for the HPGe detector. That is why a correlation of 50% appeared to be a reasonable choice, giving back a total uncertainty on the ratio of 3%.

Table 4.2: Principal sources of uncertainty and their estimated magnitudes in %.

	Neutron energy (MeV)								
	8.34	9.15	13.33	16.1	17.16	17.9	19.36	19.95	20.61
σ_{Al}	1.9	1.9	1.6	2	2	2.2	3.1	4.1	5.4
S_{Am}	5.0	4.0	2.5	2.1	1.5	1.3	6.3	1.4	5.7
S_{Al}	1.0	1.0	1.0	1.0	1.0	0.7	2.0	1.0	1.6
I_{Am}	1.2	1.2	1.2	1.2	1.2	1.2	1.2	1.2	1.2
n_{Al}	0.1	0.1	0.1	0.1	0.1	0.1	0.1	0.1	0.1
n_{Am}	0.3	0.3	0.3	0.3	0.3	0.3	0.3	0.3	0.3
$\epsilon_{\text{Al}}/\epsilon_{\text{Am}}$	3.0	3.0	3.0	3.0	3.0	3.0	3.0	3.0	3.0
$(f_\Sigma f_r)_{\text{Am}}$	0.9	0.6	0.4	0.6	0.6	0.7	0.6	0.6	0.6
$\dfrac{C_{\text{low,Am}}}{C_{\text{low,Al}}}$			0.3	0.3	0.3	0.3	1.3	1.4	1.4

4.3.2 Correlation estimation between the energy points

This section will now explain the correlations between the different energy points, which constitutes the second step after the estimation of the correlations between the terms of equation (4.9) for one energy. The sources of correlation will then be different from the ones detailed in the previous paragraph. The best example concerns the correlation between the masses of the Am sample: since we used 6 different samples for the 9 energy points, we had to introduce a 100% correlation

for n_{Am} between the points where the same sample had been used. A correlation for σ_{Al} between the different energies was also taken into account, using the values given in reference [46].

On the contrary, the detected counts S_{Am} and S_{Al} were obviously considered uncorrelated, as was the Al masses since we used different foils for the 9 measurements. The other uncorrelated term is the ratio $C_{low,Am}/C_{low,Al}$, since the TOF spectra used for the calculation were totally different from one energy to another.

All the other terms were considered as fully correlated between the different energies. This is the case for the intensity of the americium gamma ray I_{Am}, the efficiency ratio $\epsilon_{Am}/\epsilon_{Al}$ and the product $(f_\Sigma f_r)_{Am}$, since the way of determining them was exactly the same for all the energies. This gives us the following summary of correlated and uncorrelated terms between the different energies:

fully correlated terms: I_{Am}, $(f_\Sigma f_r)_{Am}$, $\epsilon_{Am}/\epsilon_{Al}$.

partially correlated terms: σ_{Al}, n_{Am}.

uncorrelated terms: n_{Al}, S_{Am}, S_{Al}, $C_{low,Am}/C_{low,Al}$.

The final covariance matrix, giving the correlation between the energy bins, was thus calculated by combining all the partial covariance matrices of the elements detailed above. The uncorrelated uncertainties contribute in a diagonal matrix, whereas the fully and partially correlated ones will contribute in full matrices detailed in appendix B. The diagonal elements for each of them correspond to the uncertainties given in table 4.2. The final covariance matrix has been split up in a vector of diagonal uncertainties, ranging from 4.4 to 8.8%, and a correlation matrix, both of them given in table 4.3 and calculated with the formula

$$Corr(x, y) = \frac{Cov(x, y)}{\sqrt{Var(x)}. \sqrt{Var(y)}} \tag{4.15}$$

4.4 TALYS calculations

A new modeling of the ^{241}Am(n,2n) reaction cross section was achieved in collaboration with the CEA/DAM from Bruyères-le-châtel. Our experimental points were used for a new parametrization using the TALYS code [12]. TALYS is a computer-code system for the prediction and analysis of nuclear reactions that involve neutrons, photons, protons, deuterons, tritons, ^{3}He and α-particles, in the 1 keV - 200 MeV energy range. Consistent calculations of all open channels above

the resonance region are possible with this modern tool associated to a comprehensive parameter library. TALYS is built on a suite of three fundamental nuclear reaction models: optical model + statistical model + pre-equilibrium model.

For this work, the optical-model calculations (of Bruyères-le-Châtel) were performed using [68, 69, 70] phenomelogical dispersive optical model potentials for neutrons and protons validated over the 1 keV - 200 MeV energy range. These potentials are not implemented in TALYS, but read as external input. Due to the fact that ^{241}Am is a deformed nucleus in its ground state, coupled-channels calculations, involving the first five states of the ground state rotationnal band and the first three states of the lowest octupolar band as the coupling scheme [70], were achieved. At this stage, it is interesting to emphasize, that the resulting total, reaction, and direct inelastic cross sections as well as neutron and proton transmission coefficients are the primordial ingredients required for the next step calculation: the statistical compound nucleus emissions (taking into account a pre-equilibrium component).

According to the neutron incident energy, the ^{241}Am(n,2n) reaction cross section results from a balanced contribution of these two processes (compound and pre-equilibrium). Moreover as previously written, these two neutron emission processes are in competition with all other open channels that can occur in the studied energy range from ^{241}Am(n,2n) reaction threshold ($E_{threshold}^{n,2n} = 6.67$ MeV) up to 21 MeV: capture, inelastic, fission and three neutron emission. This means that we have to define the right cross section magnitudes of all these channels. The calculated capture cross section was fitted to the available experimental data, by overruling the default renormalization to the s-wave strength function. Even if this channel has been taken into account, its contribution for the present study is not crucial (less than 2 millibarns). In this before mentioned energy range, the ^{241}Am(n,n') inelastic is the sum of three contributions: direct (from optical model calculations), compound and pre-equilibrium. In fact, the compound inelastic component becomes rapidly negligible with increasing incident neutron energy: it contributes up to 50% to the inelastic cross section at $E_{threshold}^{n,2n}$, and it represents around 1% only, just 2 MeV above $E_{threshold}^{n,2n}$.

Finally, to estimate the pre-equilibrium contribution, the default TALYS parameters for the pre-equilibrium model were retained. For the fission channel, the implemented TALYS model (partly improved at Bruyères-le-Châtel [70]) based on the Hill-Wheeler expression for the transmission coefficient for one, two, and three barriers was used. The total fission transmission coefficient is obtained by summing the individual Hill-Wheeler terms over all allowed (good J^π quantum numbers) discrete transition states and, for the continuum, integrating them using the appropriate fission level densities. If the excitation energy of the compound nucleus (or of the residual nucleus contributing to the multi-chance fission) is

lower than the barrier heights, fission transmission coefficients display a resonant structure due to the presence of nuclear excited levels in the second or third well (the so-called class II or III states) of the potential energy surface. In fact, it is more difficult to deal with the fission channel in a consistent way. Indeed the fission parameters have to be adjusted previously for the first chance fission before adjusting those of second chance fission (n,F= n,f + n,nf). And at higher energies we have to take into account the third chance fission (n,F= n,f + n,nf + n,2nf) and also the ^{241}Am(n,3n) mechanism. The calculation of the ^{241}Am(n,2n) reaction cross section is a certain challenge due to the fact that the cross sections of all processes are totally embedded together. Nevertheless, as compared on Fig 4.4, the new TALYS calculations from Bruyères-le-Châtel agree accurately with our present measurements.

4.5 Results discussion

Our results for the ^{241}Am(n,2n)^{240}Am reaction cross section are given in table 4.3 and compared with existing measurements and the new model calculation in figure 4.4. Also shown are the estimates from references [17, 18, 19], the ENDF/B-VII, JENDL-3.3 and BROND-2.2 evaluated data files. The first column in table 4.3 gives the neutron energy and its spread in parentheses, the second column gives the measured cross sections and the total uncertainty is given in the third column. The correlation matrix is given in the last column.

Of the nine cross sections obtained in this work three can be compared with data from earlier measurements. These three data points at the neutron energies of 8.34, 9.15 and 13.33 MeV are in excellent agreement with the recent data from Tonchev *et al.* [24]. The present result at E_n = 9.15 MeV can further be compared with the data from Perdikakis *et al.* [23] and is in similar good agreement. The point at E_n = 13.33 MeV agrees well with the data from Filatenkov *et al.* [21] and is within two standard deviations below the data from Lougheed *et al.* [22]. Unfortunately, the 7 MV Van de Graaff accelerator at IRMM does not allow measurements with neutrons in the energy range between 10 to 13 MeV, so it is not possible to contribute to an understanding of the differences between references [23, 24].

Above 15 MeV no other data are available and the six data points obtained here are the first experimental evidence for the excitation curve of this cross section. The data show a smooth behavior, although for E_n = 19.95 MeV a somewhat high value was obtained when compared to the two neighboring energies of 19.36 and 20.61 MeV.

Table 4.3: The ^{241}Am(n,2n)^{240}Am cross sections obtained from this work, with their total uncertainties and the degree of correlation between the different energy points.

Energy (MeV)	σ_{Am} (mb)	Unc. (%)	Correlation matrix (x100)								
8.34(15)	96.8	6.5	100								
9.15(15)	162.9	5.7	35	100							
13.33(15)	241.8	4.6	37	42	100						
16.10(15)	152.4	4.6	38	43	53	100					
17.16 (3)	116.1	4.4	40	45	57	58	100				
17.90(10)	105.7	4.4	41	45	57	59	84	100			
19.36(15)	89.5	8.2	21	24	30	31	39	39	100		
19.95 (7)	102.1	5.8	30	34	44	45	58	59	51	100	
20.61 (4)	77.9	8.8	20	22	29	30	40	42	39	65	100

As already mentioned, the consistent physics modeling of the calculation described in the previous section has led to excellent agreement with the new data (figure 4.4, curve labeled TALYS). A similar effort was made recently for the ENDF/B-VII evaluation [17] using another code system but the same database. Again very good agreement is shown with the present data. Of the two earlier evaluations JENDL-3.3 [18] agrees reasonably well, overshooting the data somewhat above 15 MeV and below 9 MeV, while BROND-2.2 [19] only is close to the present work above 18 MeV, showing significantly higher values than most of the data in the entire range. It is gratifying to find that consistent physics modeling and an adequate amount of data for competing channels to tune model parameters by, allows predictions for the ^{241}Am(n,2n) cross section that agree so well with experiment. In this respect it must be noted that all calculations were made before the present data and that of Tonchev *et al.* [24] were available.
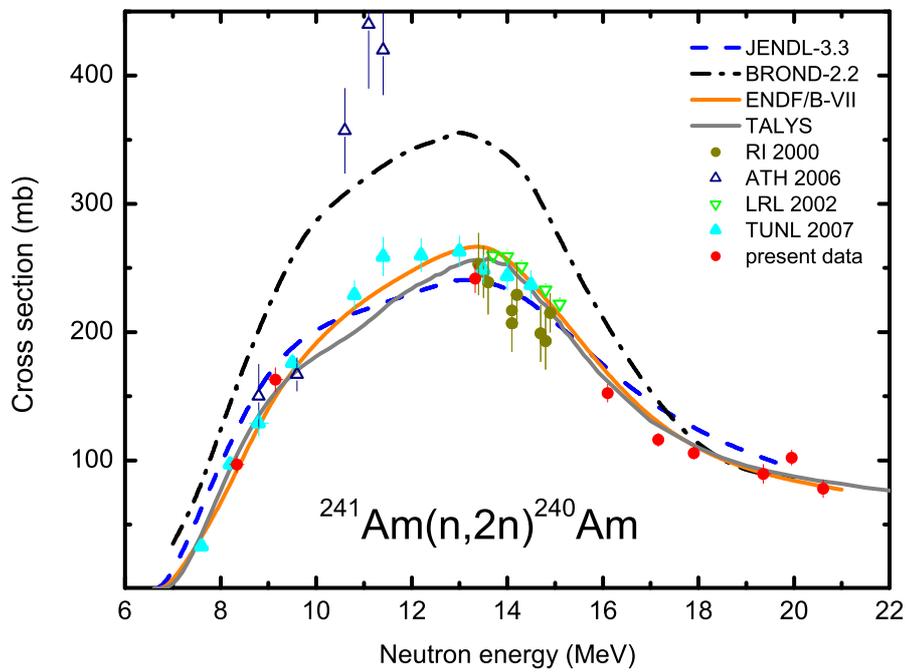
Figure 4.4: The experimental ^{241}Am(n,2n) cross sections obtained at IRMM compared with previous data and evaluations.

Chapter 5

The ^{241}Am(n,tot) reaction cross section: experimental procedure

In the so-called resolved resonance region (RRR), which is the energy range where the nuclear level spacing is larger than the Doppler and experimentally broadened natural level widths, a very good resolution in neutron energy is needed to resolve the resonance structure of the cross section. Such high resolution measurements are usually performed at pulsed white neutron beams using accelerators, combined with the Time-Of-Flight (TOF) neutron energy measurement technique. The GEel LINear Accelerator (GELINA) of the IRMM provides a pulsed white neutron spectrum with an extremely good time resolution for transmission and capture measurements.

The ^{241}Am(n,tot) and ^{241}Am(n,γ) reaction cross sections were measured at this facility during several measurement sessions between March 2007 and December 2008. The following chapter will present the total cross section measurement, whereas the next one will detail its data reduction and analysis.

5.1   Principle of the transmission measurement

The principle of the transmission measurement is the easiest among the nuclear reaction cross section measurements. An incident neutron beam with a flux $\Phi_1(E)$ hits a sample with a thickness of n atoms per barn and is attenuated by interaction of the neutrons with the sample. The outgoing flux $\Phi_2(E)$ is related to the incoming one by the total neutron cross section $\sigma_t(E)$ via the formula

$$\Phi_2(E) = \Phi_1(E)e^{-n\sigma_t(E)} \tag{5.1}$$

The *transmission factor* $T(E)$ is then defined as

$$T(E) \equiv \frac{\Phi_2(E)}{\Phi_1(E)} = e^{-n\sigma_t(E)} \qquad (5.2)$$

In practice, the simultaneous measurement of both $\Phi_1(E)$ and $\Phi_2(E)$ being very difficult, the fluxes are measured alternatingly with measurement cycles of sample in and out of the beam (see figure 5.1). Each cycle lasts about 20 min to guarantee a stability between the in and out measurements on a several days long measurement. The transmission is then written as the ratio of the time-integrated incident neutron fluxes during the in and out measurements:

$$T(E) = N_T \frac{\int_{\Delta t_{in}} \Phi_{in}(E,t)dt}{\int_{\Delta t_{out}} \Phi_{out}(E,t)dt} \qquad (5.3)$$

where the integrals run over all in and out measurement cycles. N_T stands for the normalisation factor. A precise knowledge of the detection efficiency is not required since the transmission factor is obtained via the ratio of sample in and sample out measurements. In the following sections, the neutron production as well as the measurement of the neutron fluxes and the normalisation factor will be explained.
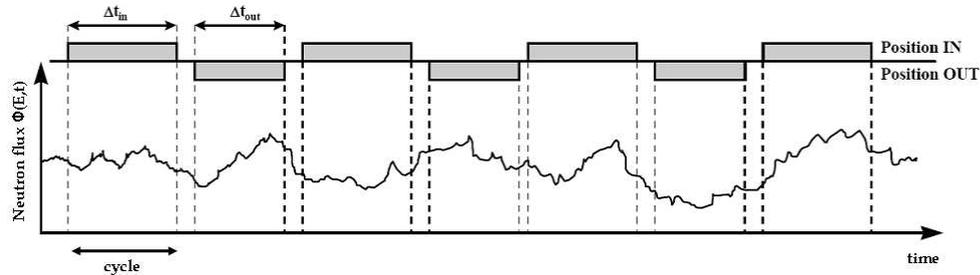
Figure 5.1: Scheme of the successive measurement cycles in a transmission measurement.

5.2 The Time-Of-Flight facility GELINA

5.2.1 Description of the neutron production facility

GELINA is a multi-user facility providing a pulsed white neutron source with a neutron energy range from subthermal to 20 MeV. It comprises four major ele-
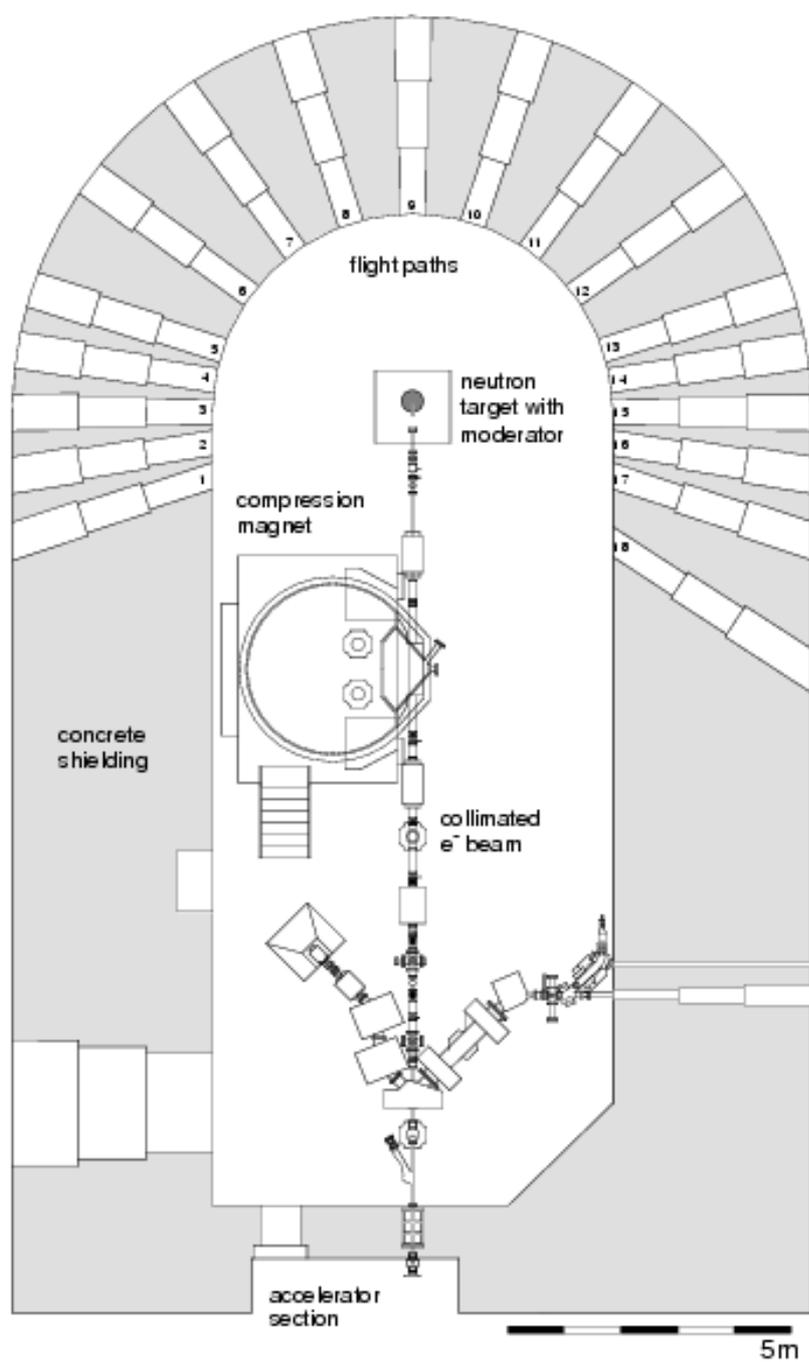
Figure 5.2: Scheme of the GELINA target hall.

ments: a linear electron accelerator, a post-accelerating beam compression magnet system, a mercury-cooled rotary uranium target and several flight paths.

Intense pulsed electron beams, at repetition rates from 40 to 800 Hz and with peak currents up to 12 A in a 10 ns time interval, are accelerated to a maximum energy of 150 MeV in a linear electron accelerator. The post-acceleration beam compression consists of a special 360° deflection magnet located in the target hall (see figure 5.2). This magnet compresses a 10 ns pulse with 12 A maximum intensity into a 1 ns pulse with 120 A maximum intensity with negligible beam loss. According to their energy and under the influence of an intense magnetic field (about 0.37 T), the incoming bunches are deflected along different trajectories. The first micropulse, having the highest energy, travels along the largest trajectory (6 m) and the last micropulse along the smallest one (3 m). After one lap inside the magnet, they leave the system at the same time toward the neutron source.

The accelerated electrons produce intense Bremsstrahlung radiation (called γ flash) in a mercury-cooled rotary uranium target (see figure 5.3) which in turn, by photonuclear reactions, produce neutrons. Heavy material such as uranium is used because the probability that electrons loose energy by Bremsstrahlung is roughly proportional to Z^2. Moreover, uranium was especially chosen because its neutron yield per incident electron is more than a factor two larger than for tantalum, used in other laboratories such as ORELA [71]. In this uranium target bombarded with 100 MeV electrons, the electron to neutron conversion rate reaches about 9%.
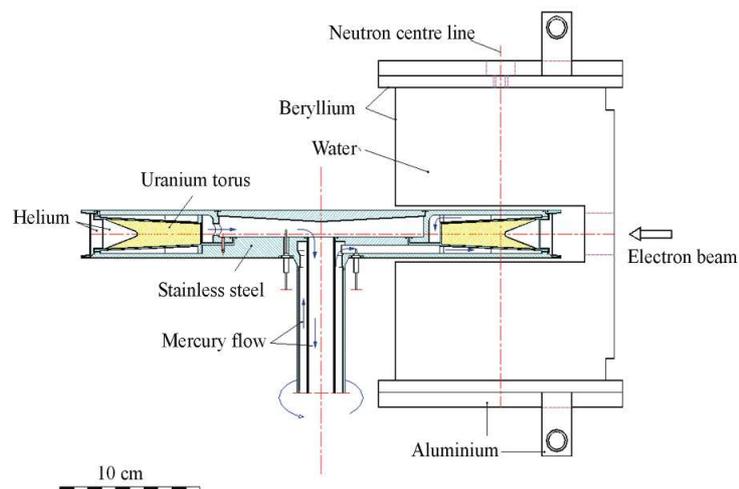
Figure 5.3: Scheme of the rotary uranium target and the Be canned water moderator.

To have a significant number of neutrons in the energy range below 100 keV, two 36 mm water moderators in a beryllium canning are placed above and below the target. At thermal energy the distribution is characterized by a Maxwellian peak, and the partially moderated neutrons have an approximate 1/E energy dependence, as illustrated in figure 5.4.
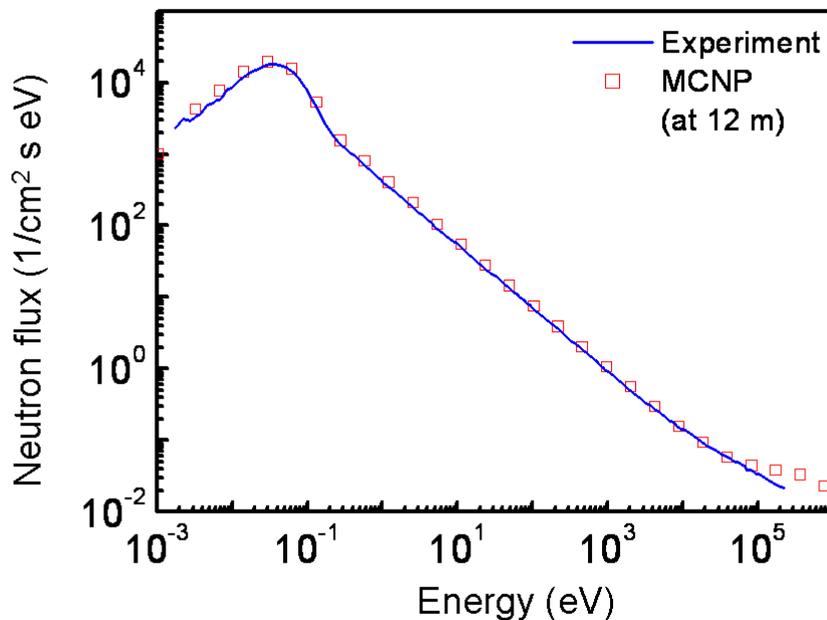
Figure 5.4: Moderated neutron spectrum at flight path 5 (12 m) [72].

By using collimators and shadow bars, moderated or non-moderated neutron beams are selected for the eighteen flight paths symmetrically arranged around the uranium target. Figure 5.5 shows the location of the transmission and capture measurement cabins along the corresponding flight paths.

5.2.2   Time-Of-Flight method

The determination of the neutron energy is based on the Time-Of-Flight method which correlates the detected events to the energy of the neutrons by measuring the time elapsed since the generation of the neutron burst. The neutron energy is given as a function of the flight time T_n and the effective flight path length L_n.
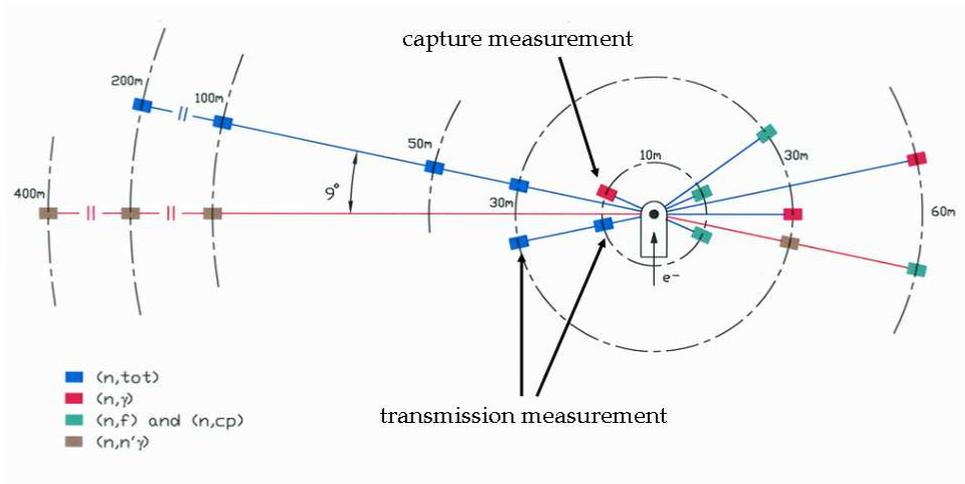
Figure 5.5: Scheme of the 10 GELINA flight paths.

This gives in the non-relativistic case:

$$E_n = \frac{1}{2}m_n\left(\frac{L_n}{T_n}\right)^2 \tag{5.4}$$

with m_n the neutron mass. If we express L_n in meters, T_n in μs and E_n in eV, equation (5.4) can be written numerically as

$$E_n = \left(72.298\frac{L_n}{T_n}\right)^2 \tag{5.5}$$

The corresponding energy resolution of the spectrometer is then

$$\frac{\Delta E_n}{E_n} = 2\sqrt{\left(\frac{\Delta T_n}{T_n}\right)^2 + \left(\frac{\Delta L_n}{L_n}\right)^2} \tag{5.6}$$

or, using the same units as previously mentioned

$$\frac{\Delta E_n}{E_n} = \frac{2}{L_n}\sqrt{\frac{E_n}{5227.039}\Delta T_n^2 + \Delta L_n^2} \tag{5.7}$$

It depends on the time resolution ΔT_n and on the uncertainty on the effective distance travelled by the neutron ΔL_n. The very short pulse duration of 1 ns in combination with the very long flight paths of up to 400 m results in the extremely high energy resolution of the GELINA TOF facility.

In TOF measurements the approximation of Gaussian distributed uncertainties on time and distance is not sufficient. Instead more accurate distributions are used and convoluted, resulting in the so-called resolution function. The resolution function is the probability that a neutron detected at a time of flight t has energy E_n, and has six main components:

- the intrinsic shape of the neutron pulse

- the source material and geometry

- the effects of the moderation of the initial fast neutrons

- the angle of the flight path normal to the surface of the source

- the neutron detector, its surroundings and electronics

- the timing channel width

The shape of the final resolution function results from the convolution of these six main processes, which is described in detail in ref. [73].

5.3 Experimental setup

5.3.1 Flight path description

The transmission measurements were performed at flight path No.2 of GELINA, a flight path that views the moderator at an angle of 9°. The chosen flight path length was 26.45 m. A detailed description of the experimental arrangement is shown in figure 5.6. The beam diameter was limited to approximately 1.5 cm, using a combination of Li-carbonate, copper and nickel collimators. The ^{241}Am sample was positioned at a distance of around 9 m from the neutron producing target, in an automatic sample changer operated by the data acquisition system. Some filters, the description and functionality of which will be detailed in the next section, were placed just before the sample.

Downstream from the filters and the sample, the neutron beam was further collimated and finally detected by a Li-glass scintillator placed at 26.45 m from the uranium neutron producing target. In this way the small solid angle subtended by the detector permits to detect only the neutrons which did not interact with the sample. The Li-glass was placed in an aluminium canning and viewed by two photomultipiers (PM) placed perpendicularly to the neutron beam axis. The aluminium canning was covered with a thin teflon foil to reflect the light to the entrance window of the PM.
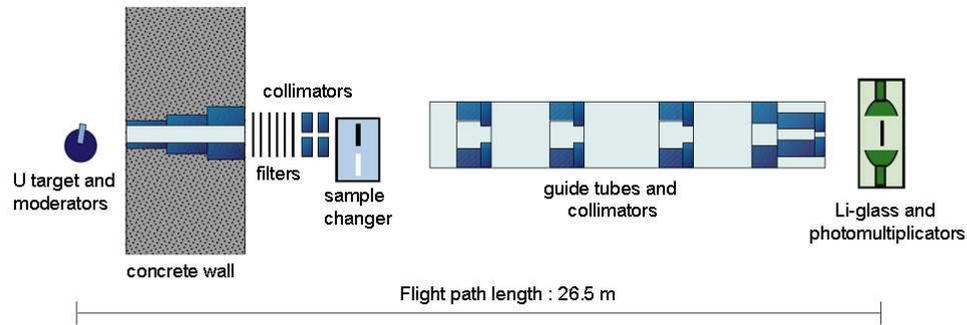
Figure 5.6: Scheme of the transmission measurement flight path.

5.3.2 Filter setup

Different filters were placed in the beam just before the americium sample, permanently or not, and could serve several purposes. Black resonance filters, such as Na, Co and Ag, were used to absorb nearly all the neutrons in a given energy region. In that way, any count rate observed in this particular energy range can be attributed to the background. The energy dependent background can then be interpolated between the different black resonance regions. The Na and Co filters remained permanently in the beam during the whole measurement, since the energy of their black resonance is much higher than the energy range of interest for the americium ones.

On the contrary, the Ag and Cd filters were placed in the neutron beam for a few background measurement cycles only, in order to have an estimate of the background at lower energy. The black resonance of cadmium at 0.2 eV allowed to get an estimation of the background in this whole lower energy region by removing completely all low energy neutrons, and among them any overlap neutrons coming from the previous pulse.

Pb and Bi filters were placed permanently in the neutron beam to reduce the influence of the gamma flash on the detection system. For the March 2007 measurement session, only the Bi filter was used for this purpose, and it was found that the attenuating thickness was not sufficient. This is one of the reasons why another measurement session was achieved in July 2008, using a much thicker Pb filter along with Bi one in order to get rid of the gamma flash influence on the detection system. Table 5.1 presents the different filters used for the transmission measurement together with their respective thicknesses and their black resonance energy.

Table 5.1: Energy and thickness of the different filters used for the transmission measurement.

Type of filter	Element	Energy (eV)	Thickness (mm)
Non permanent	Cd	0.2	1
black res. filter	Ag	5.19	0.21
Permanent	Co	132	0.2
black res. filter	Na	2850	9.1
Permanent	Bi		10
γ flash filter	Pb		9.9

5.3.3   Sample description

We used the same unique sample for both the transmission and capture measurements. This latter was prepared using the same special method described in chapter 3 for the (n,2n) measurement. The only differences are the mass of americium, which is 10 times bigger (324.5 mg), and the yttrium oxide matrix, instead of the alumina one used for the other samples. The total weight was 3.369 g, for a thickness of 3.3 mm and a diameter of 22.3 mm.

The americium-yttria composite was encapsulated into an aluminium container having the same shape as shown in figure 3.2. For this sample too, the geometry was checked by X-ray radiography and the americium content determined by calorimetry. Table 5.2 summarizes the characteristics of this sample. Two blank samples were also prepared by the JRC-ITU in Karlsruhe with exactly the same amount of yttria but without the americium oxide. They were used during the March 2007 measurement session, the goal being to get rid of the yttrium total cross section component in the transmission factor.

Table 5.2: Characteristics of the sample used for the transmission and capture measurements.

Weight (g)	Diam. (mm)	Thickn. (mm)	Y_2O_3 content (g)	^{241}Am content (mg)	Calculated ^{241}Am (wt%)
3.369	22.298	3.328	3.000	324.5±2.6	9.623

5.4   Neutron detectors

The measurement of the transmission factors $T(E)$ involves two different neutron detectors. The neutron flux $\Phi_{out}(E)$ incident upon the sample and the neutron flux $\Phi_{in}(E)$ transmitted by the sample are measured with a Li-glass detector. The normalisation factor N_T is provided by two BF$_3$ neutron detectors positioned in the target hall, the so-called central monitors.

5.4.1   Lithium glass detector

The lithium glass detector is an inorganic scintillator used to record the arrival time of the neutron in this TOF experiment. It was chosen for this purpose because it has a good timing resolution (typically 50-75 ns).

In our transmission measurement, neutrons were detected with a 4 inch diameter and 0.5" thick Li-glass (NE 905) placed in an aluminium canning and viewed by two EMI 9823 KQB photomultipliers placed perpendicularly to the neutron beam axis. Figure 5.7 shows a scheme of this kind of detector in the case of a 0.25" thick Li-glass. The detection of neutrons is based on the (n,α) reaction on ^{6}Li:

$$^6Li + n \longrightarrow \alpha + {}^3H \qquad Q = 4.78\ MeV \tag{5.8}$$
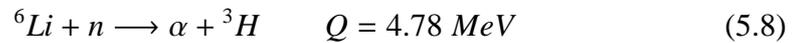
The lithium is enriched to 95% in ^{6}Li, and small amounts of cerium are added to be used as a scintillation medium. Alpha particles going through the detector generate electron-hole pairs. The free electrons migrate through the crystal until they drop into an impurity site. The de-excitation of the cerium occurs very quickly with the emission of photons. The light aluminium canning plated with barium sulfate is designed to reflect the light to the entrance window of the PMs.

The full energy peak of the (n,α) reaction is the neutron response of the detector. In order to measure the neutron flux incident upon the detector, a hardware window was selecting the events corresponding to the (n,α) reaction for the first measurement session in March 2007. A coincidence between the two PMs was also imposed. After a full upgrade of the detection setup, such an online discrimination was replaced for the July 2008 measurement by an off-line analysis of the detector response. This means that during the second measurement session, any event occuring in the Li-glass detector and above a certain threshold for the electronics was recorded.
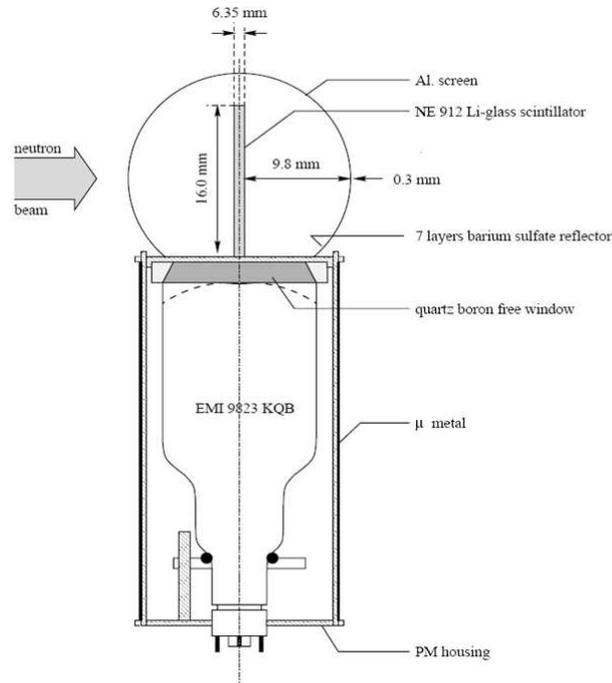
Figure 5.7: Scheme of a 0.25" thick Li-glass detector coupled with a photomultiplier.

5.4.2 Central Monitors

The total neutron output is continuously monitored by two BF_3 proportional counters placed at two different positions around the target hall, the central monitors (CM). These monitors measure the energy-integrated neutron flux. Their output is used to monitor the stability of the accelerator and to normalize the spectra to the same total neutron intensity.

Each detector is a tube measuring 2.54 cm in diameter and 63.2 cm in length (see figure 5.8). They are filled at 1 atm with a gas highly enriched in ^{10}B. The neutron detection is based on the ^{10}B(n,α) reaction, which is considered as a standard structureless cross section from thermal energy up to 200 keV.

$$^{10}B + n \longrightarrow \begin{cases} ^7Li + \alpha & Q = 2.792 \ MeV \quad \text{(ground state)} \\ ^7Li^* + \alpha & Q = 2.310 \ MeV \quad \text{(excited state)} \end{cases} \quad (5.9)$$
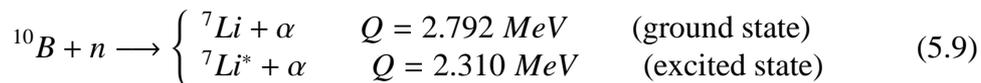
The reaction product ^{7}Li may be left either in its ground state or mainly in its excited state with the emission of a 0.48 MeV gamma ray.

The CM detects a fraction of the neutrons produced by the uranium target, and thus delivers a number proportional to the total neutron flux. Due to its energy
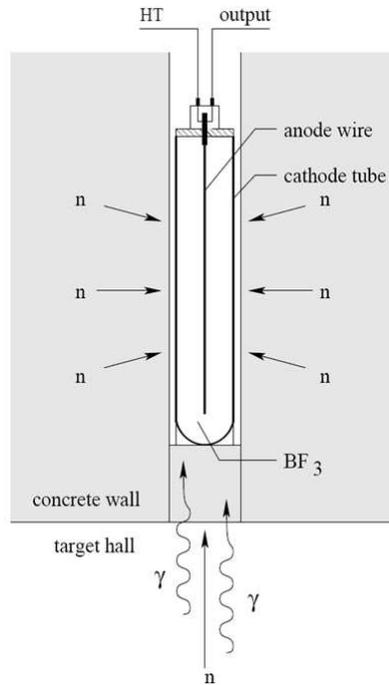
Figure 5.8: Scheme of the central monitor placed in the wall of the target hall.

dependent efficiency, a BF_3 tube mainly responds to the slow neutron component. That is why the neutrons emitted by the target-moderator assembly are partially moderated by the concrete before reaching the detector.

The background contribution is mainly due to gamma rays found together with the neutron flux. It is possible to separate gamma from neutron induced events, as most of γ-ray interactions result in low amplitude pulses. A mere amplitude discrimination enables to eliminate these contributions without sacrificing neutron efficiency.

5.4.3   Electronic setup

Description of the electronic setup

Each detector signal is divided along two different chains of electronics: one determines the pulse height according to the energy absorbed in the detector (slow signal) and the other consists of fast electronic which determines the arrival time t_n relative to the start time of the neutrons t_0.

fast signal: the anode pulse of both PMs is transmitted to a Constant Fraction Discriminator (CFD) to create fast logic signals for a coincidence unit. Whenever two pulses are present within a 30 ns coincidence window, a coincidence pulse is sent to the Fast Time Coder (FTD). This FTD, which was developed at the IRMM [74], determines with a precision of 0.5 ns the TOF of the detected neutron from the time difference between the start signal t_0, given at each electron burst, and the stop signal t_n from the coincidence unit. This time difference is converted into a channel number and sent to the data acquisition system via an interface (Modular Multi-Parameter Multiplexer (MMPM) [75]) especially developed at IRMM. By selecting only coincident pulses a significant improvement of the signal-to-noise ratio in the TOF spectrum was obtained. The FTD is reinitialized at each impulsion from the electron beam by a Pretrigger signal P_t.

slow signal: after preamplification and amplification, the slow signal is sent to an Analogue to Digital Converter (ADC), where the pulse heights are converted into channel numbers.

Together with these time spectra we also recorded the response of two CM installed in the target hall. The γ flash of GELINA was used as a reference for measuring both the actual timing of the electron burst and the overall time resolution of the detection chain.

For the July 2008 measurement session, an upgrade of the entire data acquisition system was made, replacing the analog acquisition by digitizers. The chain of electronics was then rather simplified, since we used the fast signal for both the t_0 and TOF acquisition. Instead of histograms, the data were recorded in list mode files, conserving all the information for each event occuring in the PMs above a certain threshold. Therefore the window for the selection of the (n,γ) events and the coincidence discrimination were removed. The proper background analysis to identify the (n,γ) events was achieved off-line during the data reduction. Such a system permits much more flexibility during the data analysis and the understanding of the background, but necessitates a much bigger storage memory space, since the amount of information recorded is significantly bigger.

Timing signal and accordion

In a transmission measurement, the position of the γ flash $t_{\gamma,m}$ is observed in the TOF spectrum with a delay t_{offset} as regards with the true value $t_\gamma = L/c$. This additional delay is due to the time interval between t_0 and the beam impact, the finite speed of light, the detection process and the cable lengths. The order of

magnitude of t_{offset} is about 100 μs. The exact flight time t of a neutron detected by the acquisition system at time t_n is then given by:

$$t = (t_n - t_0) - (t_{\gamma,m} - t_0) + t_\gamma = t_n + t_\gamma - t_{\gamma,m} \tag{5.10}$$

Figure 5.9 summarizes the timing signal sequence of the transmission measurement.
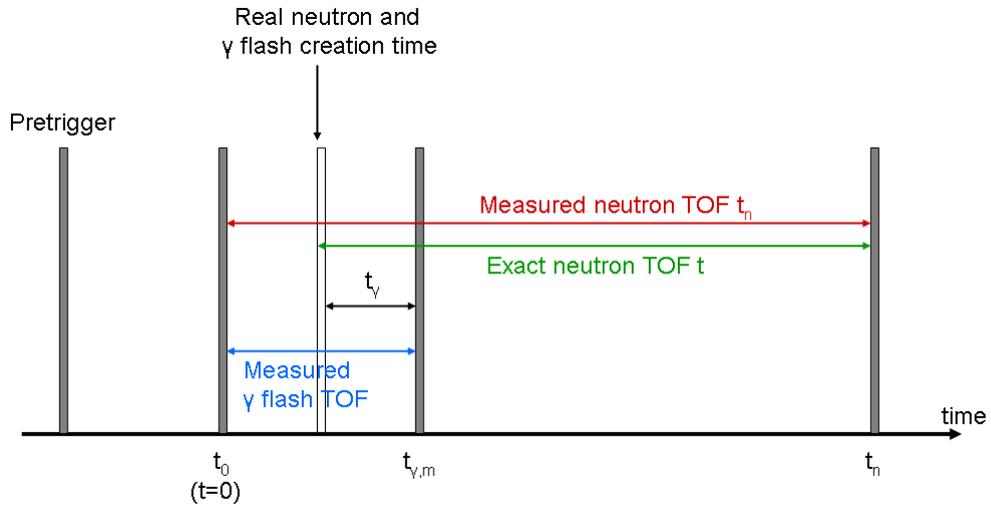
Figure 5.9: Representation of the timing signal sequence for a transmission measurement.

The number of channels available for the coding of the flight time of a neutron is 2^{23} channels, but to cover the entire neutron energy region below 100 keV in a reasonable number of channels, the TOF spectrum has to be divided into several regions. This time discretisation is called *accordion*. In each of these regions, the channel width Δt_i must be large enough to map the TOF spectrum with acceptable resolution, focusing on the region of the resonances of interest. Therefore, the flight time t_n given by the acquisition system is defined as the time elapsed from the initial channel to the center of channel n:

$$t_n = \sum_{i=1}^{n-1} \Delta t_i + \frac{1}{2}\Delta t_n \tag{5.11}$$

5.5 Measuring sequences

The transmission measurements were achieved during two sessions, in March 2007 and July 2008. Each session comprises different measurement sequences due to the alternating positions of the different filters and the running conditions of the accelerator. Table 5.3 summarizes the measurement sequences we achieved with their corresponding filter conditions.

Table 5.3: Measuring sequences of the transmission measurements.

Measurement session	Sequence	Number of cycles	Filters					
			Cd	Ag	Co	Na	Bi	Pb
March 2007	am070313	238		X	X	X	X	
	am070319	160		X	X	X	X	
	am070321	112	X		X	X	X	
	am070326	117	X		X	X	X	
	am070328	87			X	X	X	
	am070413	15			X	X	X	
	am070416	334			X	X	X	
July 2008	am080703a	14			X	X	X	X
	am080704	14			X	X	X	X
	am080707	191			X	X	X	X
	am080710	35	X		X	X	X	X
	am080711	20		X	X	X	X	X
	am080714	19		X	X	X	X	X
	am080714a	50			X	X	X	X

Chapter 6

The ^{241}Am(n,tot) reaction cross section: data reduction and analysis

In this chapter will be presented the process of the data reduction using the program codes AGL and AGS (Analysis of Geel Spectra [76]) especially developped at IRMM, as well as the data analysis with the program REFIT [77]. AGL was used to treat the list mode data from the July 2008 measurement and reconstruct the TOF spectra. AGS was then employed on both March 2007 and July 2008 raw spectra to derive the transmission factor.

   A first analysis of the reduced data using REFIT is then detailed, bearing in mind that final reliable results will only be possible after a simultaneous analysis with the capture measurement, this latter being not included in this PhD work.

6.1   Data reduction

6.1.1   Data sorting with AGL

This first step of the raw data treatment only concerns the July 2008 measurement session, where the data were recorded in list mode file. The software package AGL was especially developed at IRMM to analyse list mode data taken with the new acquisition system and to prepare the input data for the AGS package for the further data reduction steps presented in the next paragraph.

   The big advantage of this new acquisition system is to control off-line the TOF spectra reconsitution by separating the neutron events from the background in the most accurate way. Picture 6.1 shows the amplitude spectra obtained from

the two PMs (black and red curves) and their summed signal (green curve) for the sample in position. The full energy peak of the (n,α) reaction corresponding to the neutron events is roughly located between channels 120 and 800 for each PM. Defining such a window appears to be much more convenient on the summed signal from the two PMs, since the (n,α) peak limits are clearer. That is why we chose in practice to keep the events corresponding to a defined window between channels 250 and 1024 of the green curve. Such a cut was achieved on-line for the March 2007 measurement, by determining the window thresholds in a rough way with an oscilloscope at the beginning of the measurement session. This method was of course much less precise, and we had no control on eventual fine tuning of the threshold during the experiment.
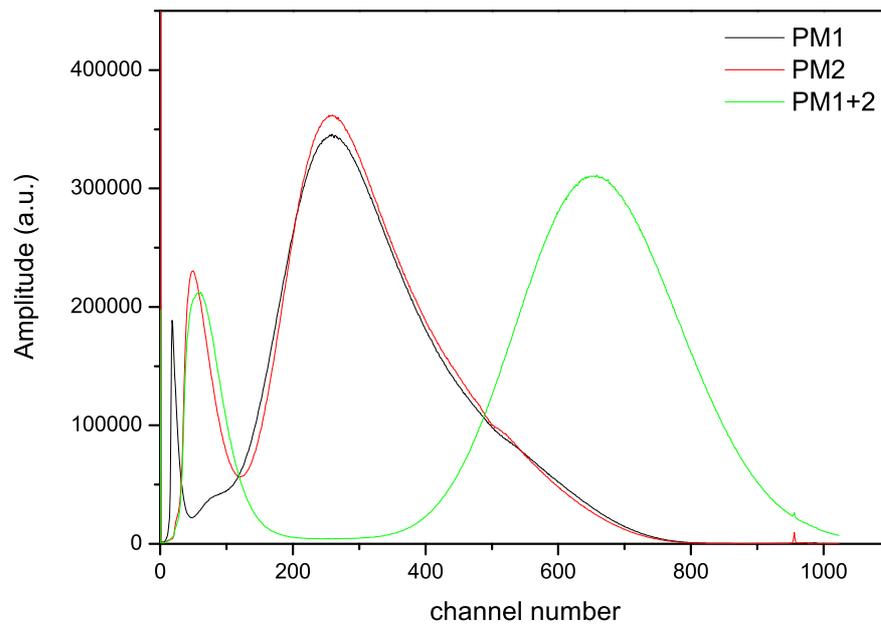
Figure 6.1: Amplitude spectra from the PMs obtained for the am080707 measurement session.

In order to improve the accuracy of the cut, we plotted the PM1 amplitude spectrum versus the one from PM2 in a 3D plot, so as to visualize the regions to be precisely cut. Figure 6.2 shows such a plot without any cut condition in the data (i.e. all PM events from channel 0 to 1024). The orange central region corresponds to the coincident (n,α) events. It appears that the cut previously defined
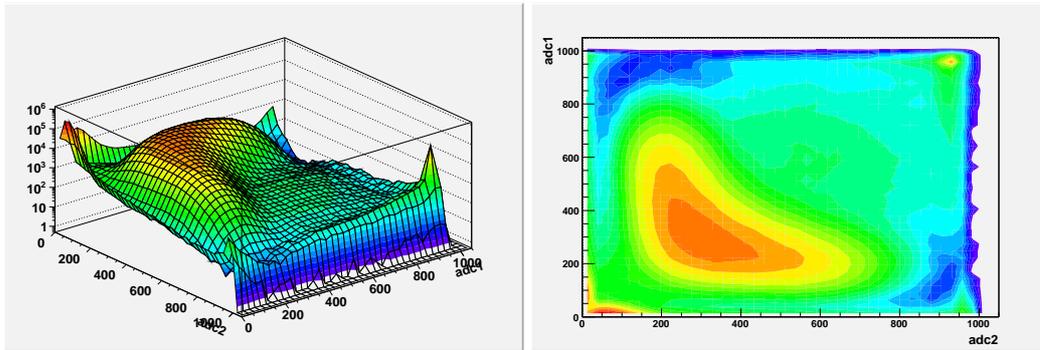
Figure 6.2: PM1 versus PM2 amplitude spectrum in the case of the am080704 measurement session, no cut condition.
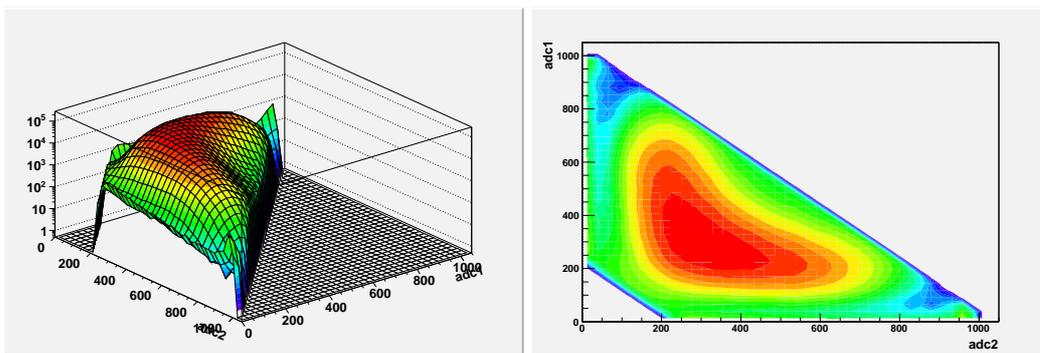
Figure 6.3: PM1 versus PM2 amplitude spectrum in the case of the am080704 measurement session, AGL cut condition.
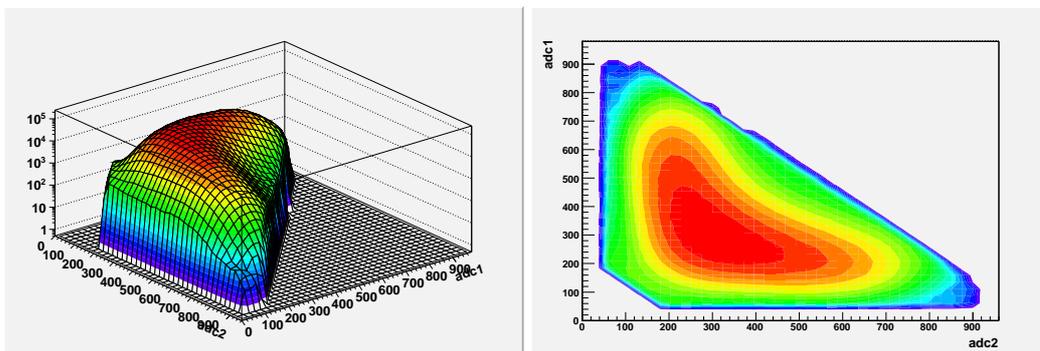
Figure 6.4: PM1 versus PM2 amplitude spectrum in the case of the am080704 measurement session, Root cut condition.

on the summed signal (shown in figure 6.3) may be improved by adding a certain threshold on each PM, in order to get rid of the events that gave a high signal in PM1 and a small one in PM2, and vice versa. These events correspond in the plot to the higher counts observed along the X and Y axes. Figure 6.4 shows this optimized cut with the three conditions corresponding to two thresholds on each PM and another window on the summed signal.

Unfortunately the software AGL does not allow to build TOF spectra taking into account these three conditions together. We could only build spectra according to one single cut condition, on either PM1, PM2, or the summed signal. That is why we developed a special script using the Root environment [78] in order to build such a spectrum and compare it with the one built with AGL according to the sole condition on the summed amplitude spectrum first mentioned. Figure 6.5 shows the reconstructed raw spectra from AGL for three different cut conditions on the summed signal and two sample positions (in and out). The different steps observed in the curves correspond to the accordion settings. In figure 6.6, which is a zoom of the previous one on the first resonance, we can clearly see the difference in the spectra when we apply the cut window keeping only the (n,α) reaction peak (AGL cut) or no cut condition at all (no cut), but the AGL and Root cuts do not show any notable difference. Yet these latter can be seen in figure 6.7 where the difference between the AGL and Root cuts in the TOF reconstructed spectra is plotted in %. This difference is less than 1% in the americium resonance region, but can reach up to 7% around the black resonances. It is depending on the ratio between the counts from the (n,α) peak and the background, and is then more visible at the bottom of the resonances in the sample in spectrum.

The low cut condition corresponds to a window from the threshold up to the lower part of the (n,α) peak. It contains events from the lower tail of the (n,α) reaction as well as events from the noise sources. This can be seen in figure 6.8 where the americium transmission is still visible on a large background. Table 6.1 summarizes the different cut conditions previously mentioned on the amplitude spectrum.

Table 6.1: Different cut conditions achieved on amplitude spectra.

	Condition on PM1	Condition on PM2	Condition on PM1+PM2
no cut	none	none	none
AGL cut	none	none	250 < channels < 1024
Root cut	50 < channels < 900	50 < channels < 900	250 < channels < 1024
low cut	none	none	channels < 250
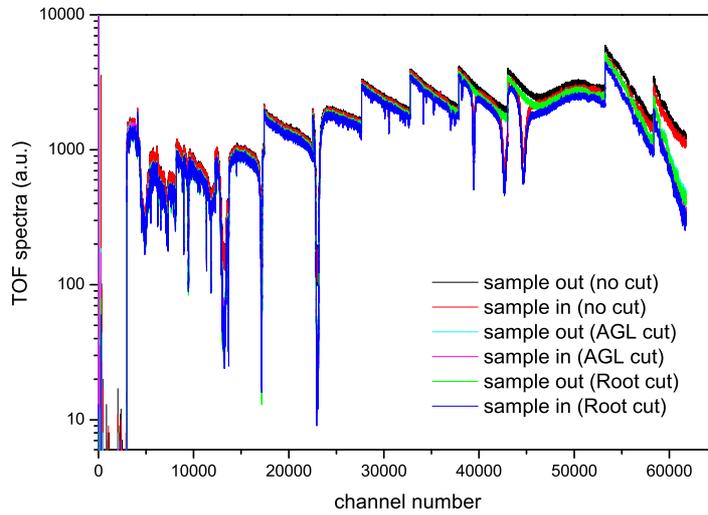
Figure 6.5: Reconstructed raw spectra for the sample in and out positions using AGL for 3 different cut conditions in the case of the am080707 measurement session.
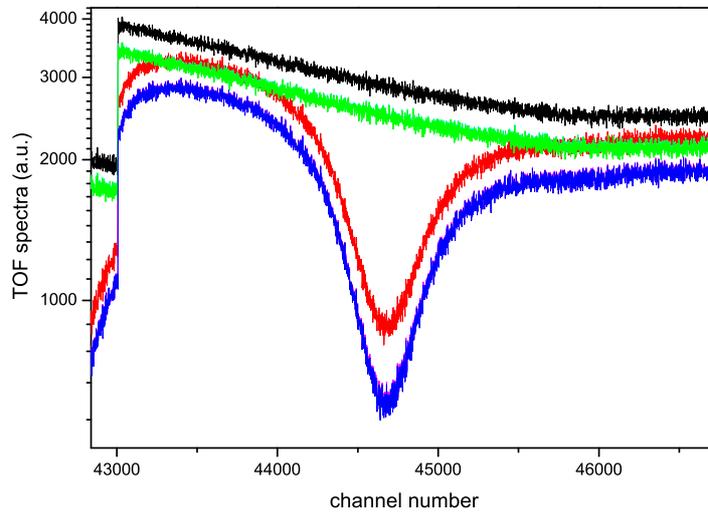
Figure 6.6: Zoom of the previous spectra around the first resonance of americium. The spectra using AGL or Root cuts nearly coincide.
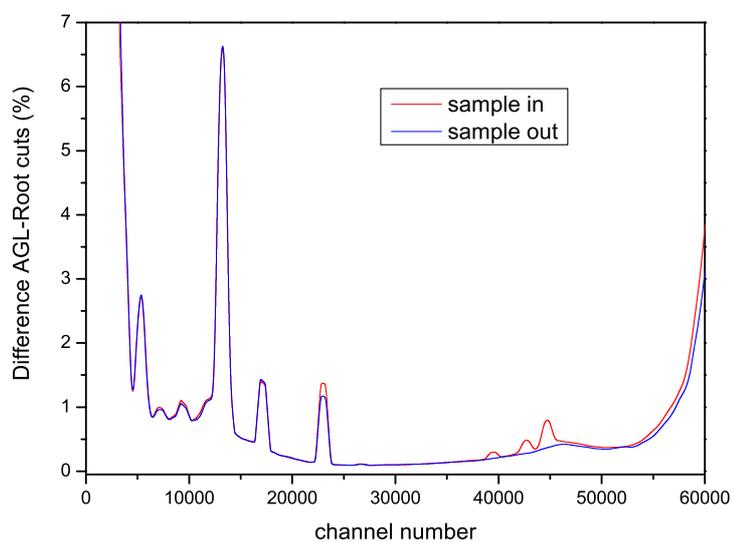
Figure 6.7: Relative difference (AGL-Root)/AGL in % between the AGL and Root cuts in the reconstructed TOF spectra regrouped per 500 channels.
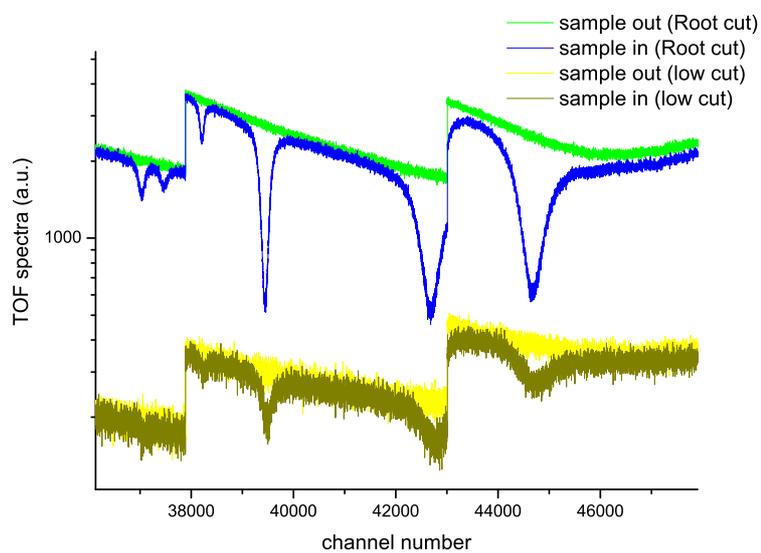
Figure 6.8: Zoom of the Root and low cut reconstructed spectra around the 3 first resonances of americium.

In the following sections, the AGL specified spectra will refer to the cut made with AGL on the summed amplitude spectrum, whereas the Root specified spectra will refer to spectra obtained with the three conditions on PM1, PM2 and the summed spectrum.

6.1.2   Data reduction with AGS

To derive the transmission factor from the raw TOF spectra, we used the data processing package AGS especially developped at IRMM [76]. This package includes the most important spectra manipulations, such as dead time correction, normalisation, background fitting and substraction and TOF-to-energy conversion.

The package also includes a full propagation of uncertainties, starting from the uncorrelated uncertainties due to counting statistics. The final transmission factor, deduced from the raw TOF spectra, includes a complete covariance matrix accounting for both uncorrelated and correlated uncertainty components.

Dead time correction

The raw TOF spectra have first to be corrected for losses due to the dead time in the detector and the electronics chain. The dead time is monitored continuously by a registration of the time interval distribution between different events. From this time interval spectrum shown in figure 6.9, we deduce a dead time of about 100 ns for a neutron event, and around $2\,\mu$s for the dead time blinding the detector after the γ flash.

Normalisation

The normalisation factor N_T from formula (5.3) accounts for differences in integrated intensities of the incident neutron beam during the in and out measurement cycles. For the normalisation to the same neutron fluence the information of two BF_3 neutron flux monitors are used: CM1 and CM3, which are counting neutrons without distinction of the energy.

After a stability check of each of them, it was found that CM3 was slightly more stable, as is shown in figures 6.10 and 6.11. The standard deviations of the mean of the distribution of the ratio values for consecutive in and out cycles are shown in table 6.2 along with the respective average values in the case of the am070313 measurement session.
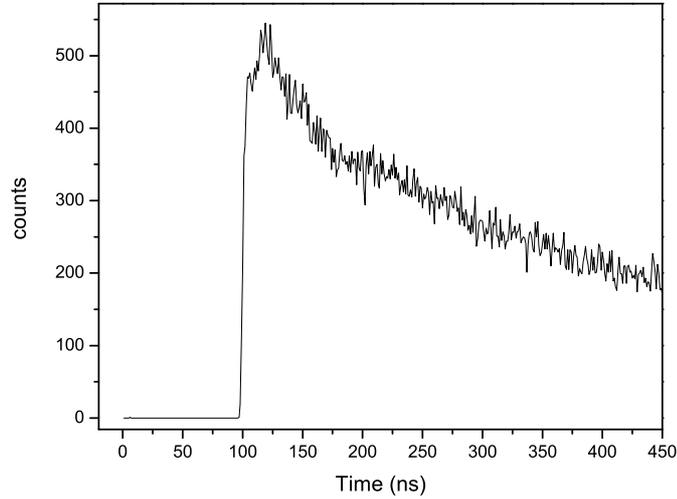
Figure 6.9: Typical time interval spectrum used for the dead time determination.

Table 6.2: Mean values of the count ratios for consecutive in and out cycles for CM1, CM3 and T_0 in the case of the am070313 measurement session.

	Mean	St. dev. of the mean
CM1	1.0568(93)	8.56×10^{-4}
CM3	1.0578(72)	6.62×10^{-4}
T_0	1.0595(142)	1.31×10^{-3}

Therefore it was the neutron counts from CM3 that was used to calculate the normalisation factor. The monitor counts M are both time and energy integrated from the monitor flux Φ_m reaching CM3 placed in the target hall. The normalisation is then calculated from the formula:

$$N_T = \frac{\iint_{\Delta t_{out}} \Phi_m(E,t)dEdt}{\iint_{\Delta t_{in}} \Phi_m(E,t)dEdt} = \frac{\sum m_{\Delta t_{out}}}{\sum m_{\Delta t_{in}}} = \frac{M_{out}}{M_{in}} \qquad (6.1)$$

This gave a normalisation value of 1.0681 for the sum over all measurement sessions without non permanent filter for the March 2007 campaign, and 0.993 for July 2008.
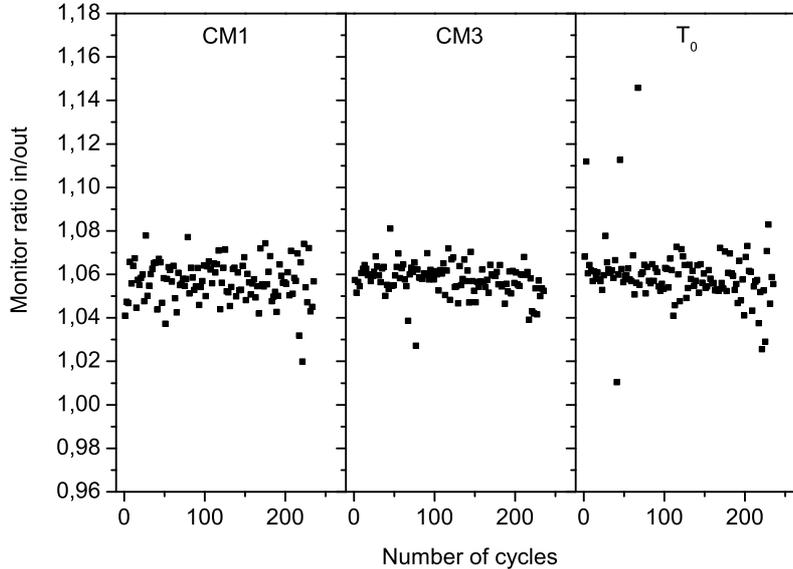
Figure 6.10: Ratio of CM and T_0 values for consecutive in and out cycles for the measurement session am070313.

Background estimation

The transmission factor is in practice obtained as the ratio of the time-integrated spectra C_{in} and C_{out}, corrected for their background contribution B_{in} and B_{out} respectively:

$$T(E) = N_T \frac{C_{in} - B_{in}}{C_{out} - B_{out}} \tag{6.2}$$

The technique used to obtain the time dependent background is based on the black resonance method. The background is indeed derived from the saturated resonance dips formed by the resonances of Na, Co, Ag and Cd, absorbing all neutrons at 2 850, 132, 5.19 and 0.2 eV respectively. The background over the whole time range is parameterised by the smooth function:

$$B(t) = a_1 + a_2 t^{a_3} + a_4 e^{-a_5 t} + a_6 e^{-a_7 t} \tag{6.3}$$

which was found to best describe the different time dependent background components due to scattered neutrons from the environment (a_1), gamma rays issued from neutron captures in the collimators and the flight path tubes ($a_2 t^{a_3}$), 2.2 MeV gammas from neutron moderation in the GELINA target ($a_4 e^{-a_5 t}$), and overlap neutrons from the previous pulse ($a_6 e^{-a_7 t}$).
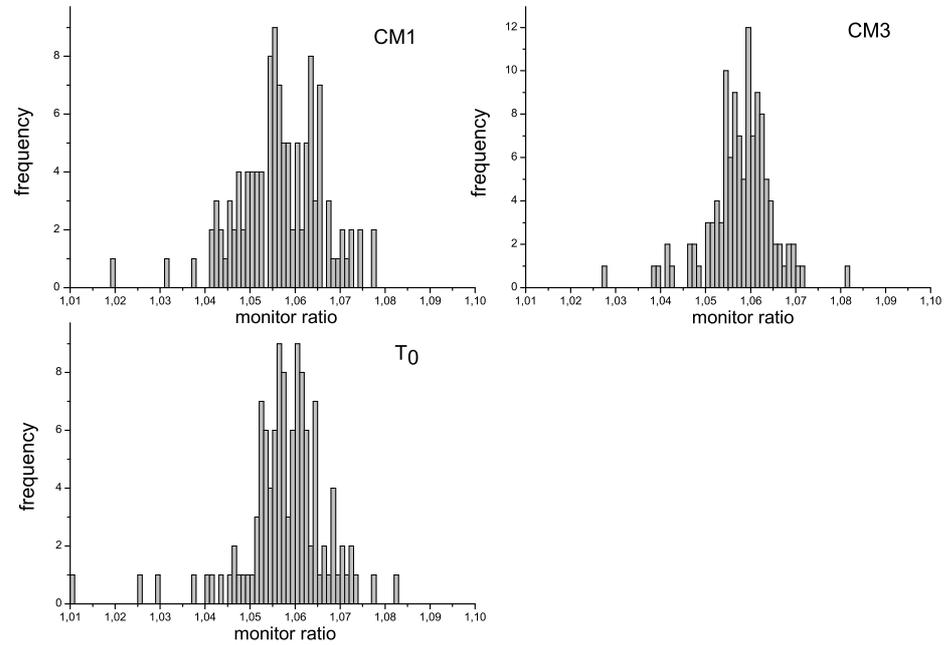
Figure 6.11: Distribution of the ratio values for CM and T_0 for the am070313 measurement session.

In practice the time parameters a_3, a_5 and a_7 were determined using the measurements with the non permanent background filters Cd (for the lower energy term especially) and Ag (for the background shape around the Am resonances). The amplitudes a_1, a_2, a_4 and a_6 were then adjusted during the background fit of the measurement with the permanent filters Na and Co, which was then used for the transmission factor calculation. Figure 6.12 and 6.13 show the first and the last step of this background estimation: a fit of the black resonances with the Cd filter and another one with only Na and Co.
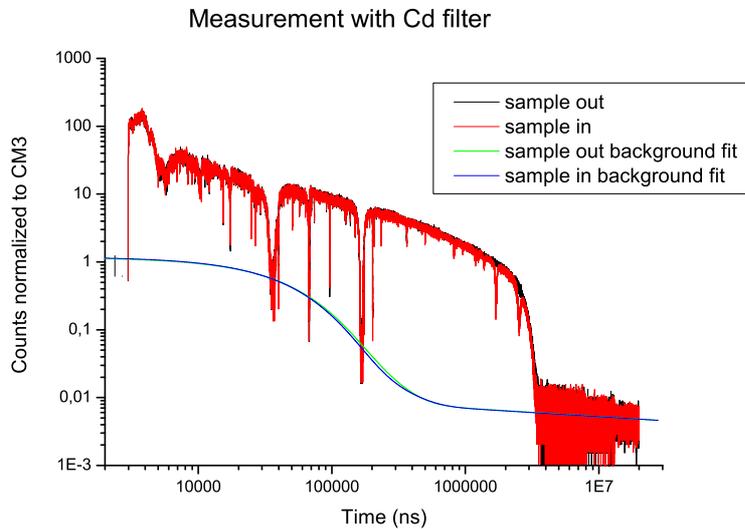
Figure 6.12: Background estimation with the Cd black resonance filter, July 2008 measurement campaign.
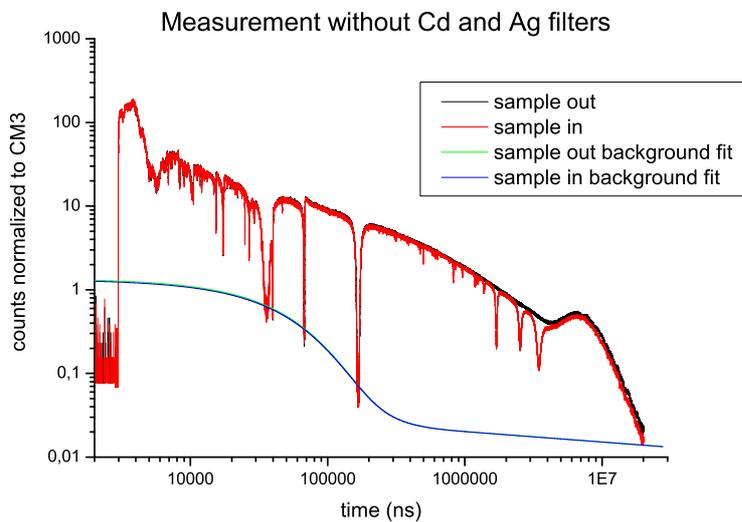
Figure 6.13: Background estimation without the non permanent filters, July 2008 measurement campaign.

Transmission ratio

The last operation achieved with AGS on the reduced data is the calculation of the transmisison ratio itself, following equation 6.2. Figure 6.14 shows the transmission obtained during the March 2007 measurement session, as well as the ones from July 2008 using the AGL and the Root cuts. The difference between the March 2007 and July 2008 measurements comes from the dummy with yttria matrix used for the March 2007 measurement session for the sample out position. The green curve is almost exactly the same than the red one, which indicates that the Root cut does not give a significant improvement to the AGL one.
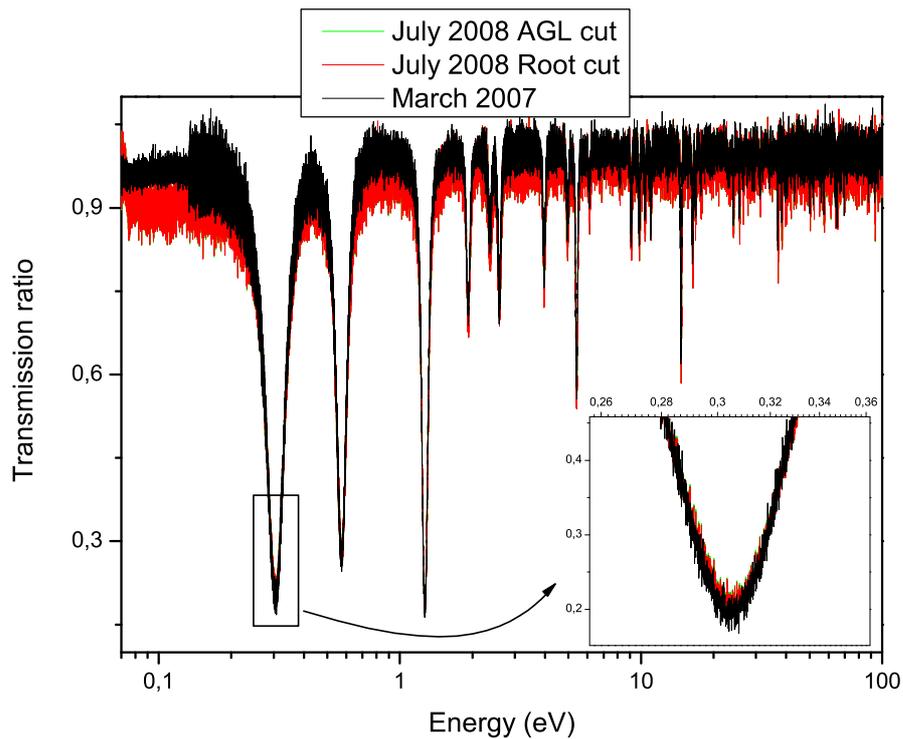
Figure 6.14: Transmission ratios obtained in the different measurement campaigns.

6.2 Resonance analysis with the REFIT code

6.2.1 Determination of resonance parameters from experimental data

In the Resolved Resonance Range, cross sections can be parameterized by the resonance parameters such as the potential scattering radius, the resonance energy, the neutron, radiation and fission widths, and the spin and parity of the resonance.

The simplest method to extract resonance parameters from measured data is the area analysis [79, 80]. For a well-isolated resonance we can define areas that can be related to the experimental observables. These areas for transmission, capture and elastic scattering are respectively:

$$A_t = \int (1 - e^{-n\sigma_t}) dE \tag{6.4}$$

$$A_\gamma = \int (1 - e^{-n\sigma_t}) \frac{\sigma_\gamma}{\sigma_t} dE \tag{6.5}$$

$$A_n = \int (1 - e^{-n\sigma_t}) \frac{\sigma_n}{\sigma_t} dE \tag{6.6}$$

If we neglect the Doppler broadening effect and consider only the resonant part of the SLBW formalism, we get the following asymptotic relations in the limit of a very thin or very thick sample [81]:

$$A_t(\text{thin}) = \frac{1}{2}\pi n\sigma_0\Gamma = 2n\pi^2 \lambda^2 g\Gamma_n \tag{6.7}$$

$$A_t(\text{thick}) = \sqrt{\pi n\sigma_0}\Gamma = 2\pi\lambda \sqrt{ng\Gamma_n\Gamma} \tag{6.8}$$

$$A_\gamma(\text{thin}) = \frac{1}{2}\pi n\sigma_0\Gamma_\gamma = 2n\pi^2 \lambda^2 g\frac{\Gamma_n\Gamma_\gamma}{\Gamma} \tag{6.9}$$

$$A_n(\text{thin}) = \frac{1}{2}\pi n\sigma_0\Gamma_n = 2n\pi^2 \lambda^2 g\frac{\Gamma_n\Gamma_n}{\Gamma} \tag{6.10}$$

where σ_0 stands for the peak total cross section of the considered resonance. It is clear from equations (6.7) and (6.8) that thick and thin sample transmission measurements yield values of Γ and $g\Gamma_n$ and will provide complementary data. When $\Gamma_n \gg \Gamma_\gamma$ the neutron width will dominate the total width, so that $\Gamma_n \simeq \Gamma$, and g and Γ_n can be determined from a combiantion of thin and thick transmission measurements. In the same way when $\Gamma_\gamma \gg \Gamma_n$ the radiation width will dominate the total width, so that $\Gamma_\gamma \simeq \Gamma$, and the radiation width will be determined together with $g\Gamma_n$. Table 6.3 summarizes the sensitivity of the different areas in the different possible cases.

Table 6.3: Resonance area sensitivity to the different resonance parameters for a thin and a thick sample.

	Area	$\Gamma_n \ll \Gamma_\gamma$	$\Gamma_n \gg \Gamma_\gamma$
A_t (thin)	$2n\pi^2 \lambda^2 g\Gamma_n$	$\simeq ng\Gamma_n$	$\simeq ng\Gamma_n$
A_t (thick)	$2\pi\lambda \sqrt{ng\Gamma_n\Gamma}$	$\simeq \sqrt{ng\Gamma_n\Gamma}$	$\simeq \sqrt{ng}\Gamma_n$
A_γ	$2n\pi^2 \lambda^2 g\frac{\Gamma_n\Gamma_\gamma}{\Gamma}$	$\simeq ng\Gamma_n$	$\simeq ng\Gamma_\gamma$
A_n	$2n\pi^2 \lambda^2 g\frac{\Gamma_n\Gamma_n}{\Gamma}$	$\simeq ng\frac{\Gamma_n\Gamma_n}{\Gamma}$	$\simeq ng\Gamma_n$

6.2.2   Resonance shape analysis with REFIT

In practice, one has to correct for the broadening due to the Doppler effect and the resolution of the spectrometer in order to get the experimental observables previously mentioned. That is why it is usually prefered to include these effects by performing a full resonance shape analysis of the data using codes such as REFIT [77] or SAMMY [82].

Both codes are based on the Reich-Moore approximation of the multi-level R-matrix formalism. These codes account for the Doppler broadening, and the transmission factor is folded with the experimental resolution. The resonance parameters together with experimental data parameters (normalisation, background, effective temperature, target thickness and homogeneity) can be determined by a least squares fit of the experimental data. The REFIT code is based on the familiar least-square method, whereas SAMMY is based on the so-called generalized least-square fitting procedure.

Experimental resolution function

To confront the experiment with the theory, the transmission data must be broadened with the Doppler effect and with the experimental resolution function of the facility. The resolution function is the distribution in time of the neutron flight time. These two elements broaden the natural width Γ_{tot} and attenuate the amplitude of the nuclear resonances. The observed total width Γ_{obs} is then determined from the natural width, the Doppler width ΔE_{dop} and the resolution width ΔE_{res}. The observed width at half maximum may be estimated from the quadratic sum of these contributions assuming that they are approximately Gaussian in shape and independent:

$$\Gamma^2_{obs} = \Gamma^2_{tot} + \Delta E^2_{res} + \Delta E^2_{dop} \tag{6.11}$$

The neutron energy resolution function for a TOF measurement is composed

of several functions convoluted together. The main components are the intrinsic shape of the neutron pulse, the source material and geometry, the timing channel width, the angle of the flight path normal to the surface of the source, and the neutron detector with its surroundings and electronics. Most of these components are simple functions of time or energy and can be represented by a few parameters. The experimental resolution function of the GELINA facility is fully described in ref. [73], where a detailed description of the analytic formulas implemented by M. Moxon in REFIT is given.

Doppler broadening

At lower energies, the Doppler broadening will be the dominating effect. In order to take this into account, the theoretical cross sections are averaged over the thermal motion of the target nuclei. Doppler-broadened cross sections σ_D are obtained by convoluting the unbroadened cross section σ with the scattering function $S(E', E)$ as is explained in section 2.4. The Doppler broadening calculations are usually based on the free gas model, however the use of a more realistic model derived from the Lamb's harmonic crystal model [37] is recommended when atoms are bound in a crystal lattice, like in our case.

We used here the Dopush option in REFIT, that was implemented using subroutines developed by Naberejnev [83]. These routines require the phonon distribution in the solid under investigation, which is then introduced in the $g_C(E, t)$ function from equation (2.39). Such distributions were calculated using the GULP software (General Utility Lattice Program) [84]. This latter gives the phonon density spectrum by fitting and optimizing interatomic potentials to experimental values.

Different functional forms for two-body interatomic potentials can be found in the the literature: Buckingham, Lennard-Jones or Morse potentials, etc. Due to a lack of experimental data on thermal properties of AmO_2, we used the calculated UO_2 phonon spectrum instead, assuming comparable behaviors [85]. Our GULP calculations were based on a Buckingham potential with parameters from ref. [86]. Figure 6.15 shows the UO_2 phonon spectrum that we obtained, together with its projection on oxygen and uranium. This latter was the input spectrum used by REFIT for the fits of the first americium resonances.

Figures 6.16 and 6.17 clearly show the improvement made in the fit with the use of the crystal lattice model (Dopush option) instead of the free gas model for the first americium resonances. The bottom of the resonances is better fitted, as can be seen with the disappearance of a shape in the residuals. Such an evidence of the influence of the Doppler model used in the resonance shape analysis at such
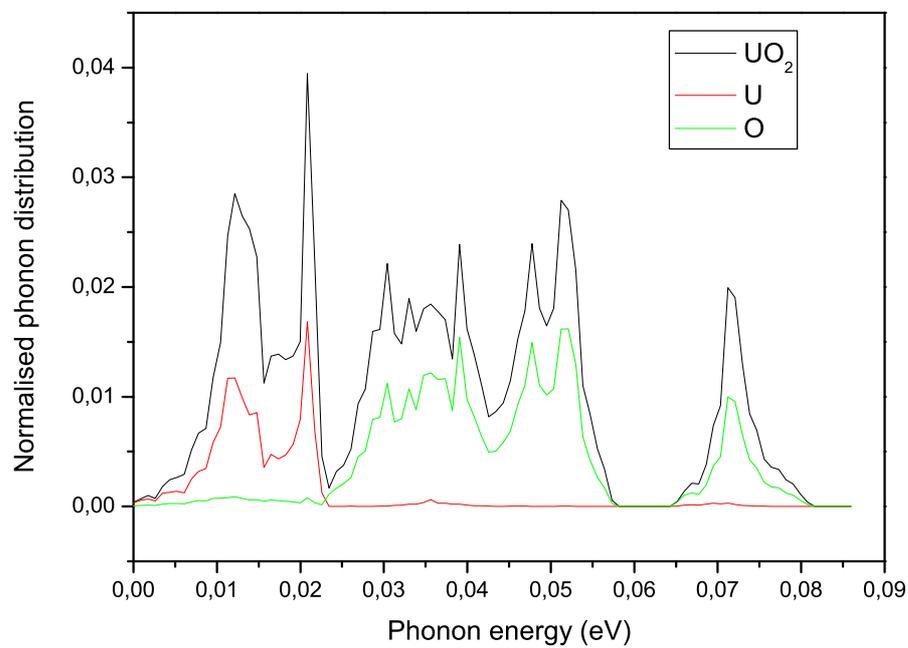
Figure 6.15: Phonon spectra for UO$_2$ calculated with GULP.

low energies confirm the results already presented in ref. [87] in the case of the ^{237}Np lower energy resonances.
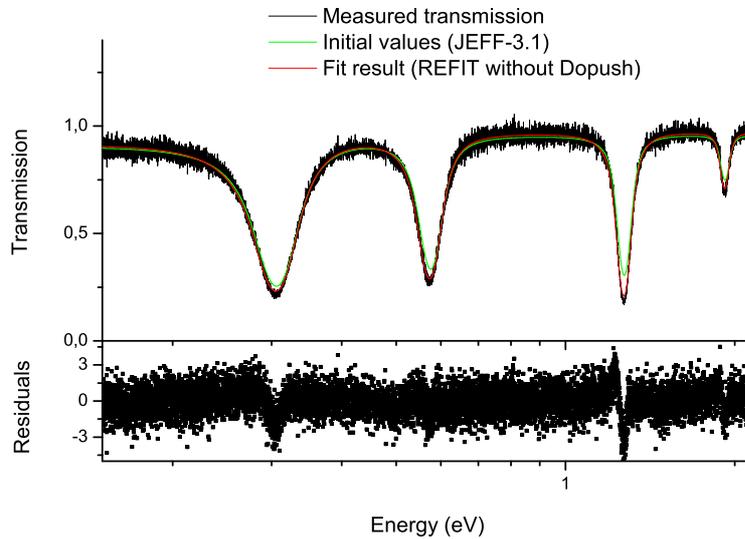
Figure 6.16: Fit of the first americium resonances (E, Γ_γ, Γ_n) with REFIT using the free gas model for Doppler broadening, case of the March 2007 measured transmission factor.
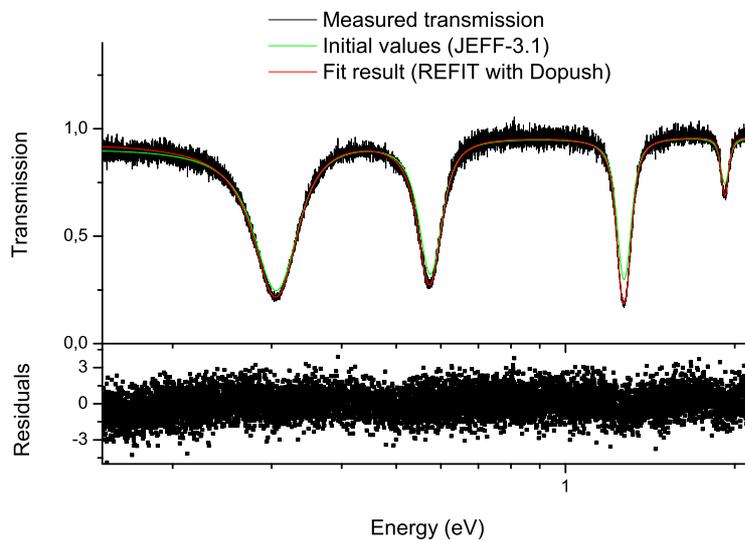
Figure 6.17: Fit of the first americium resonances (E, Γ_γ, Γ_n) with REFIT using the Dopush option for Doppler broadening, case of the March 2007 measured transmission factor.

Preliminary results

The analysis was focused on the 3 first resonances at 0.3, 0.57 and 1.27 eV respectively, since the sample thickness was especially foreseen for this purpose. Figure 6.18 shows an extended energy range of the measurement up to 100 eV. For this plot, only the normalisation and the first resonance energy were fitted. We can see that any fit of a resonance beyond a few tens of eV will be hardly possible.
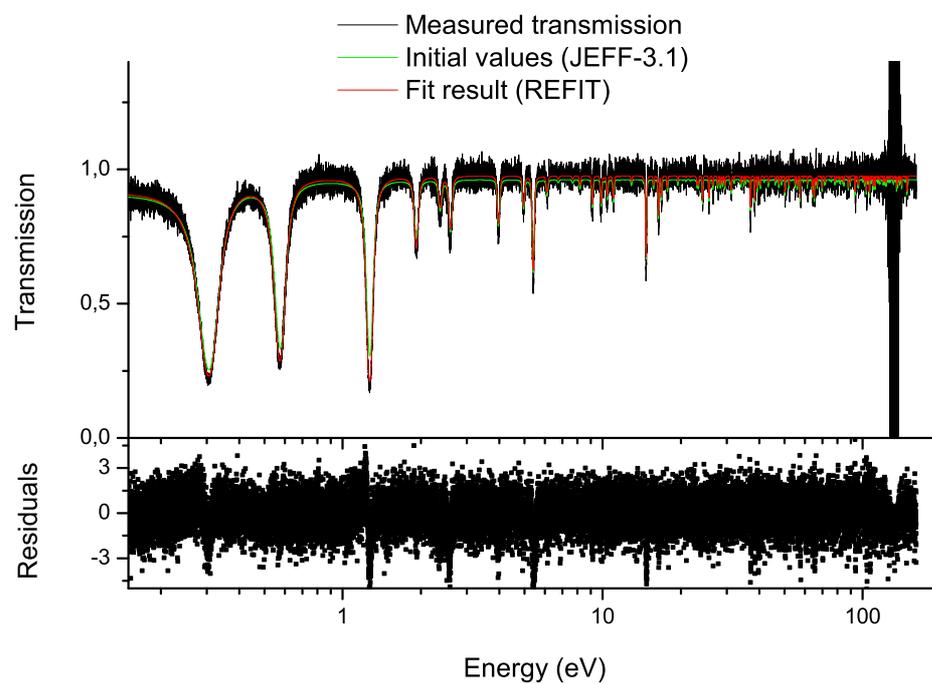
Figure 6.18: Plot of the extended energy range of the transmission measurement up to 100 eV.

Figures 6.19, 6.20 and 6.21 present some fits of the 3 first resonances achieved in two different conditions. All measured data presented here are coming from a data reduction on an AGL cut raw data from the July 2008 measurement session.

On the left hand side are presented fits where the normalisation, the resonance energy E and the neutron width Γ_n were fitted, since our type of measurement is supposed to be mainly sensitive to this last quantity (see table 6.3). The value of 9.3 fm for the interaction radius a_c was taken from the JEFF-3.1 library. The fit results on the right hand side present the same fits but where the radiation width Γ_γ
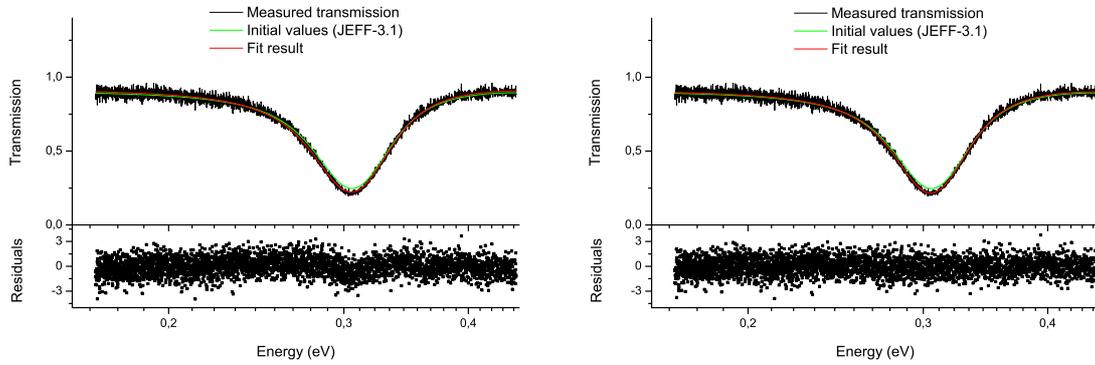
Figure 6.19: Fit result of the 1st americium resonance.
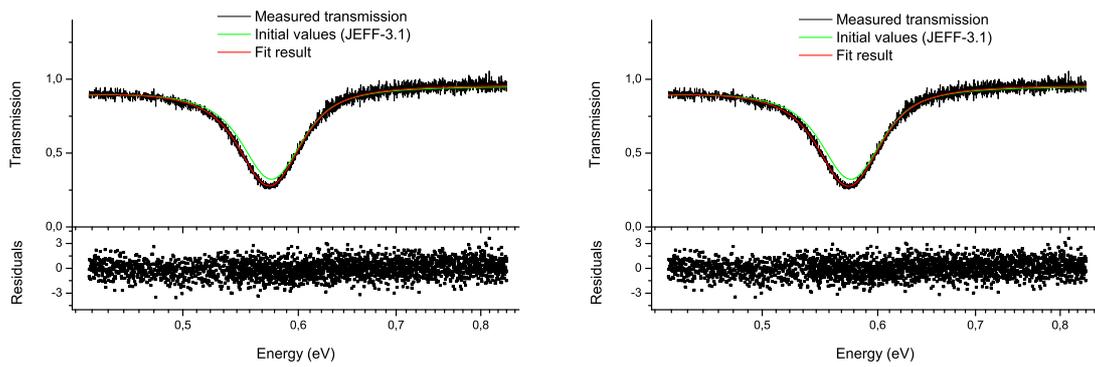
Figure 6.20: Fit result of the 2nd americium resonance.
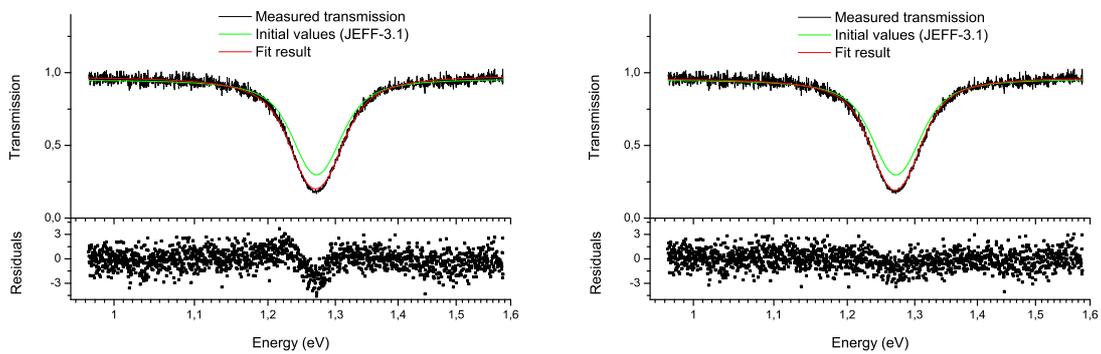
Figure 6.21: Fit result of the 3rd americium resonance.

was fitted together. We can see that this slightly improves the fit quality, especially for the 3rd resonance. The fit results are summarized in table 6.4. It is important to mention that these values remain preliminary, since a simultaneous analysis with the capture measurement will be necessary to get more accurate results.

Table 6.4: Our results for different fitting conditions of the 3 first resonances of americium.

	E (eV)	Γ_γ (meV)	Γ_n (μeV)
Resonance 1			
JEFF-3.1	**0.306849**	**43.530**	**61.440**
Fit 1	0.306246(41)		66.771(112)
(χ^2=1.1215)			
Fit 2	0.306281(42)	41.527(131)	64.924(170)
(χ^2=1.0427)			
Resonance 2			
JEFF-3.1	**0.576365**	**40.670**	**132.00**
Fit 1	0.574290(64)		150.86(36)
(χ^2=1.0183)			
Fit 2	0.574188(67)	40.835(195)	151.78(46)
(χ^2=1.0058)			
Resonance 3			
JEFF-3.1	**1.273296**	**48.440**	**290.30**
Fit 1	1.272079(86)		392.50(84)
(χ^2=1.4766)			
Fit 2	1.272134(91)	43.867(255)	374.26(1.13)
(χ^2=1.2317)			

Our transmission measurement is plotted together with previous measurements and libraries in figure 6.22. The evaluations for the JENDL3.3 and ENDF/B-VII libraries were based on the measurements from references [25, 26], and seem to underestimate the total cross section of the first resonances of americium. Our measurement seems to confirm the new reevaluation for the total cross section made by O. Bouland [88] for the JEFF-3.1 library towards a higher value of the cross section. In this sense, our measurement better agrees with the previous one from [28].
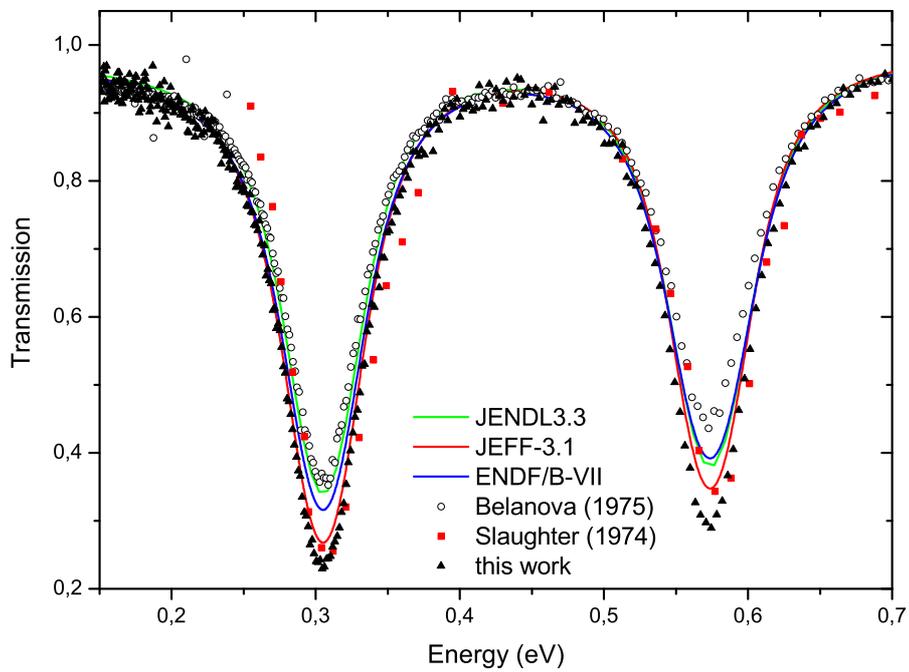
Figure 6.22: Comparison between our total cross section measurement and previously existing data and libraries.

Chapter 7

Simulation of new C_6D_6 detectors for capture cross section measurements at GELINA

This chapter will present the simulation of a new design of C_6D_6 detectors that are planned to be used at GELINA for capture cross section measurements. It will briefly explain the capture measurement principle and focus on the work done on the simulation of the C_6D_6 detectors. The measurement of the ^{241}Am(n,γ) reaction cross section was achieved at GELINA from October to December 2008, but its description and data analysis are not part of this PhD work.

7.1   Principle of the capture measurement

The principle of the capture measurement relies on the detection of the gammas emitted during the interaction between the neutron beam and the sample. The incident neutron flux needs to be known, either by previous measurements, or more accurately by a simultaneous measurement. The capture measurement is then related to the neutron capture cross section $\sigma_\gamma(E)$ via the capture yield $Y(E)$, which is defined as the number of capture events $N_c(E)$ per incident neutron $\Phi(E)$. The capture yield is expressed as:

$$Y(E) = N_Y \frac{N_c(E)}{\Phi(E)} \equiv (1 - e^{-n\sigma_t})\mu \frac{\sigma_\gamma(E)}{\sigma_t(E)} \tag{7.1}$$

with N_Y the normalisation factor and μ the multiple scattering correction. In practice $N_c(E)$ and $\Phi(E)$ are measured simultaneously with two C_6D_6 detectors and a boron chamber respectively.

In such a neutron capture reaction, the compound system decays to its ground state through the emission of one or several γ-rays in cascade. It is thus essential for the efficiency of a radiative neutron capture detector to be independent of the particular γ-ray cascade (i.e. independent of the shape and multiplicity of the gamma spectrum). Moreover, its sensitivity to scattered neutrons should be as low as possible, and the detector should have a very good time resolution.

To achieve these goals, two classes of detectors can be considered: the total absorption detector and the total energy detector. The total absorption detectors rely on the collection of all gamma rays emitted in a capture event. It has to be a 4π-detector surrounding the sample with a 100% detection efficiency for all gammas, independent of the energy. It is usually a liquid scintillator of large volume, its main drawback being its sensitivity to scattered neutrons inducing an important background contribution.

The technique applied at GELINA is the use of the total energy detection principle using the Pulse Height Weighting Technique (PHWT) with C_6D_6 detectors. This principle is based on the use of a low efficiency detection system with a γ-ray detection efficiency ϵ_γ that is assumed to be proportional to the γ-ray energy E_γ:

$$\epsilon_\gamma = kE_\gamma \tag{7.2}$$

If the γ-ray detection efficiency is very small ($\epsilon_\gamma \ll 1$), such that only one γ-ray out of the capture cascade is registered at a time, the efficiency ϵ_c of a capture event can be expressed as:

$$\epsilon_c = \sum_i \epsilon_{\gamma i} = k \sum_i E_{\gamma i} = kE^* \tag{7.3}$$

Under these conditions the detection efficiency ϵ_c is directly proportional to the total energy released in the capture event E^*, which is the sum of the neutron binding S_n and kinetic E_n energies in the center of mass.

An efficiency for a capture event is thus obtained that is independent of the decay cascade and hence of the resonance. The required proportionality is obtained by applying the PHWT by means of the so-called weighting function $WF(E_d)$:

$$\epsilon_{\gamma i} = \sum_{E_d} R_d(E_d, E_\gamma)WF(E_d) = kE_{\gamma i} \tag{7.4}$$

with E_d the energy of the pulse height spectrum and $R_d(E_d, E_\gamma)$ the response function of the detection system, which is the number of γ-rays $N_{\gamma i}(E_d, E_\gamma)$ observed at a given pulse height energy normalised to the number of capture events $N_c(E_\gamma)$:

$$R_d(E_d, E_\gamma) = \frac{N_{\gamma i}(E_d, E_\gamma)}{N_c(E_\gamma)} \tag{7.5}$$

The response function is mathematically manipulated to achieve the proportionality between the detection efficiency and the γ-ray energy. This technique is based on an original suggestion by Maier-Leibnitz which was first applied by Macklin and Gibbons [89] and fully explained in [90].

7.2   Simulation of the new C$_6$D$_6$ detectors

At GELINA, so far, a set of maximum four C$_6$D$_6$ detectors is used. In view of the proven suitability for the determination of high accuracy capture results this will remain the system of choice. However, for the study of enriched and possibly radioactive isotopes, it was found that we need to maximise the detection efficiency in order to cover a wider range of cases of interest to various applications. Therefore a new design of C$_6$D$_6$ detectors was built, combining a very low sensitivity to neutrons with a substantial increase of the detection efficiency. This will allow to carry out measurements on nuclides for which only small quantities of sample material are available.

Effective use of the detectors requires their precise characterisation for both γ-ray and neutron sensitivity. Here, results of Monte Carlo simulations using MCNP will be shown in comparison with measured response functions using calibrated sources and test measurements at GELINA.

7.2.1   Detector geometry

These new detectors are composed of two parts: a 2.8 L aluminium container filled with C$_6$D$_6$ and an EMI 9823KQB photomultiplier connected to it through a boron free quartz window. The Al container is a truncated 5-sided 12.5 cm high pyramid. A μ-metal shield covers the PM to provide an electromagnetic insulation. Deuterated benzene with a D/H ratio of 114 was used as scintillator material.

Figure 7.1 shows the modelled geometry as designed in the MCNP input file, using the VisEd 3D viewer included in the MCNP5 package [55], along with a picture of the detector. This figure shows up to which details the detectors were modelled in the simulations, and especially the design of the PM including the cylindrical glass tube with its several sections and the metal dynodes.
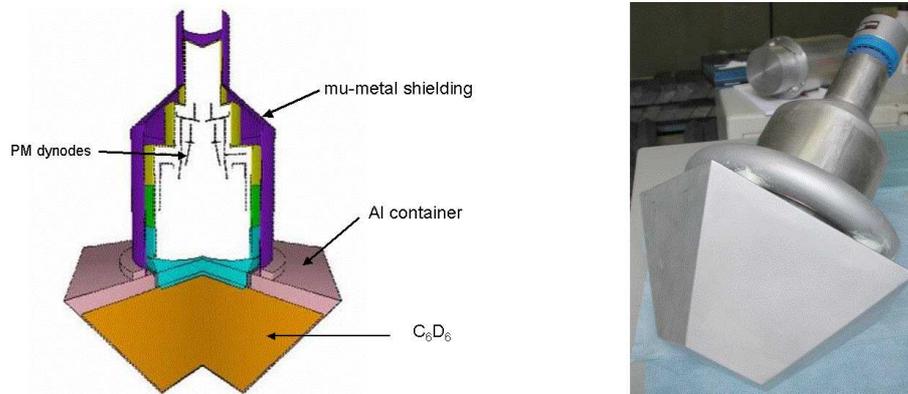
Figure 7.1: MCNP picture of the detectors.

7.2.2   Simulated detector responses

Gamma-ray efficiency

The F8 pulse height tally of MCNP5 was used to track photon and electron in-
teractions along the path of the photon emitted by a monoenergetic point source
placed at 9 cm from the detector, since this distance will correspond to the setup
where these detectors will first be used. An event was considered as detected
if the calculated energy deposition in the scintillators was exceeding a threshold
of 150 keV. The integral of the deposited energy normalized to the quantity of
incident energy defines the total gamma efficiency at one precise energy $\epsilon_\gamma(E_\gamma)$.

Figure 7.2 shows on the left the simulated response to different monoener-
getic sources, together with the results obtained from the calculations of the total
gamma efficiency on the right. We observed that the ratio new/previous design for
the total gamma efficiency is a bit less than the expected value of 4 coming from
the ratio of the scintillators volume. Besides, we can also notice that the gamma
efficiency is definitely not proportional to the incident energy, which confirms the
need of the weighting function described before.

Neutron sensitivity

The neutron sensitivity of C_6D_6 detectors is defined as the probability that a neu-
tron entering the assembly creates a signal relative to the γ-ray detection prob-
ability. The consequences of this important background source, mainly coming
from the neutron scattering in the sample, have been illustrated by Koehler *et al.*
[91] in the example of a high resolution TOF measurement on ^{88}Sr, and further
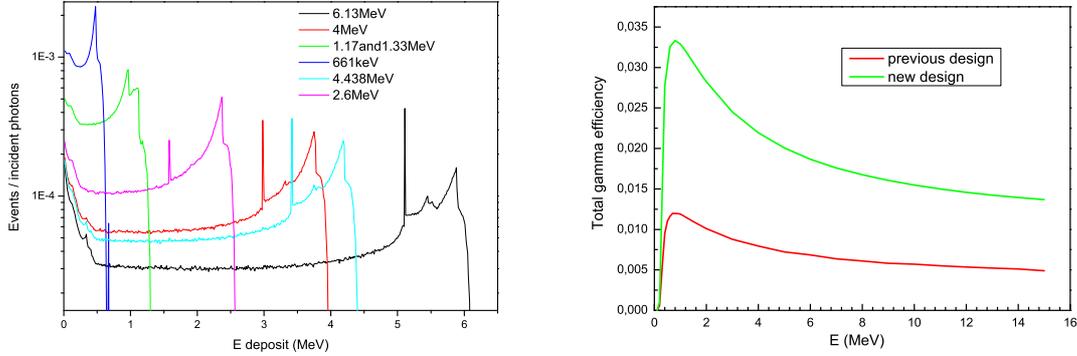
Figure 7.2: Simulated response to different monoenergetic sources for the new C$_6$D$_6$ detector together with the comparison of calculated total gamma efficiencies for the new and previous detector designs.

investigated by Plag *et al.* [92], who discussed in detail the various components contributing to the neutron sensitivity and reported on a C$_6$D$_6$ detector with the lowest neutron sensitivity that has ever been achieved. A. Borella *et al.* benchmarked the entire device in ref. [90]. This sensitivity of the detection system to neutrons plays an important role for all resonances with a neutron width much larger than the radiation width, which is the case for light nuclei and for heavier ones close to shell closures.

The same tally as for the gamma efficiency calculations was used for the MCNP simulations, tracking the photon and electron interactions along the path of the neutron emitted from a point source. We also kept the minimum threshold of 150 keV to define a detected event in the scintillators. Several monoenergetic neutron sources were simulated, covering the energy range from 0.1 eV to 1 MeV with equidistant steps on a logarithmic scale. In order to have the same neutron probability for each step, the neutron flux distribution for each interval was modified with a $1/E$ shape. Each detector response, consisting in the distribution of the energy deposited in the scintillators, was integrated and normalised to the detection probability for a 4 MeV γ-ray, so as to get the neutron sensitivity $\epsilon_n/\epsilon_\gamma$ [90, 92].

The neutron sensitivity of the previous and the new geometry are compared in figure 7.3 in the case of one detector placed in a 4 detectors setup. We observe that these neutron sensitivities are of the same order of magnitude. Thus the improvement of the gamma efficiency by a factor 4 was not accompanied by an increase of the neutron sensitivity. Moreover, the contribution of fluorine present in

the Teflon of the previous detector has disappeared, as can be seen with the lower
neutron sensitivity above 100 keV for the new detector. The new detection system
on the whole also seems to be less sensitive to components resonance structures,
as we can observe with the lack of resonance structure in the spectrum concerning
the 45 and 131.4 eV Mo resonances, as long with its other resonances between
300 and 700 eV. This is partially explained by the fact that the molybdenum is
only present in the μ-metal composition, and the shielding of the new detector is
slightly smaller (10% less in terms of volume).
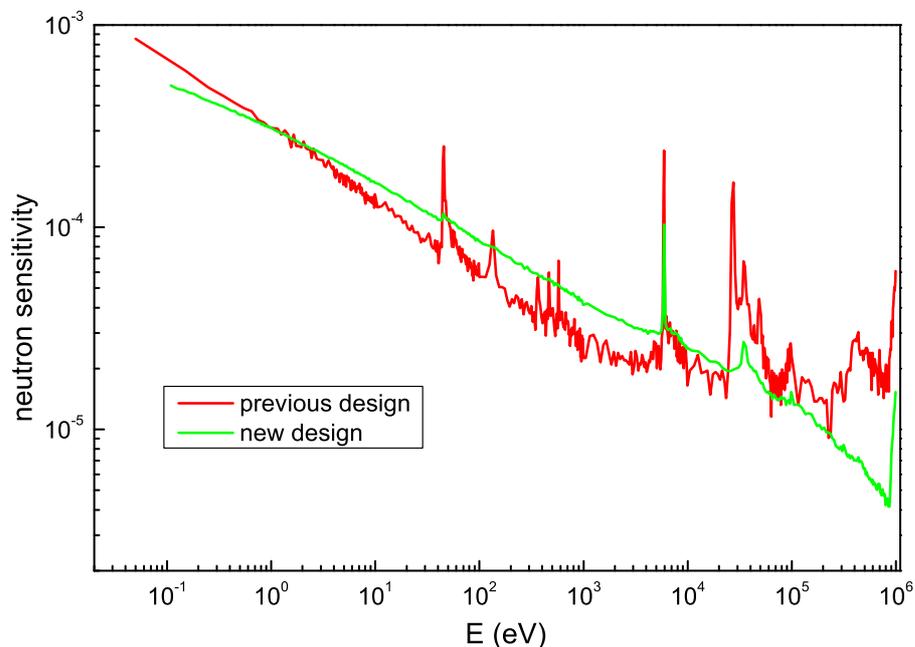
Figure 7.3: Simulated neutron sensitivity for 1 detector among the 4 detectors
setup.

Figure 7.4 shows the relative contribution of the different components as a
function of neutron energy. This illustrates the strong impact of materials such as
the 1 mm thick μ-metal shielding and the presence of ^{10}B fraction in the glass tube
of the PM at low energies. The 5.9 and 35 keV Al resonances are also strongly
visible in the neutron sensitivity. The inelastic scattering threshold for aluminium
is responsible for the significant raise in its contribution at 1 MeV neutron energy.
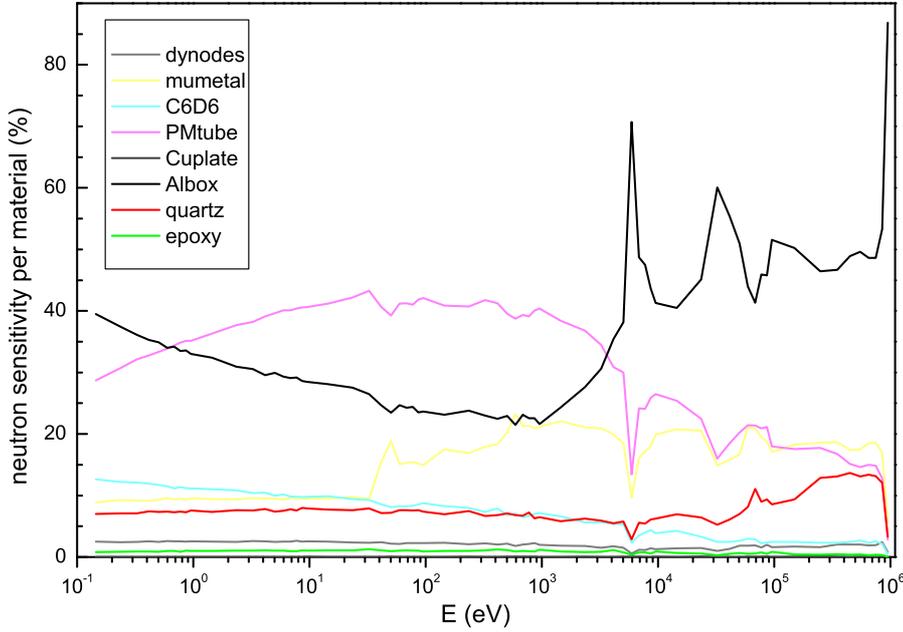
Figure 7.4: Relative contribution of each component material to the detector neutron efficiency.

7.2.3   Comparison with experimental measurements

Experimental measurements were performed with a capture detection setup installed at the 10 m flight path station at GELINA and consisting of 4 C$_6$D$_6$ detectors, as is illustrated in figure 7.5. The final response function $R_d(E_d, E_\gamma)$ was obtained by a convolution of the simulated response $R_e(E_e, E_\gamma)$ with a Gaussian function $G(E_d - \mu(E_e))$ representing the amplitude resolution of the detector [90]:

$$R_d(E_d, E_\gamma) = \int R_e(E_e, E_\gamma) G(E_d - \mu(E_e)) dE_e \tag{7.6}$$

with

$$G(E_d - \mu(E_e)) = \frac{1}{\sqrt{2\pi}\sigma_\mu} e^{-\frac{(E_d - \mu(E_e))^2}{2\sigma_\mu^2}} \tag{7.7}$$

The simulated response $R_e(E_e, E_\gamma)$ represents the transfer of γ-ray energy E_γ in energy E_e which is deposited within the detector. The conversion of E_e into the

observed energy E_d is defined by the relationship $\mu(E_e)$ and a resolution broadening σ_μ, which are functional forms of E_e and $\mu(E_e)$ respectively. To determine this functional relationship of the mean value and the variance together with the free parameters a similar procedure as discussed in ref. [93] was applied. The experimental response for well-known monoenergetic γ-rays was compared with the simulated ones obtained from equations (7.6) and (7.7). The free parameters in the expressions for $\mu(E_e)$ and $\sigma^2(E_e)$ were determined by a least squares fitting procedure using experimental observed response functions. In order to determine the functional forms, it is sufficient to fit the upper portion of the measured spectrum.
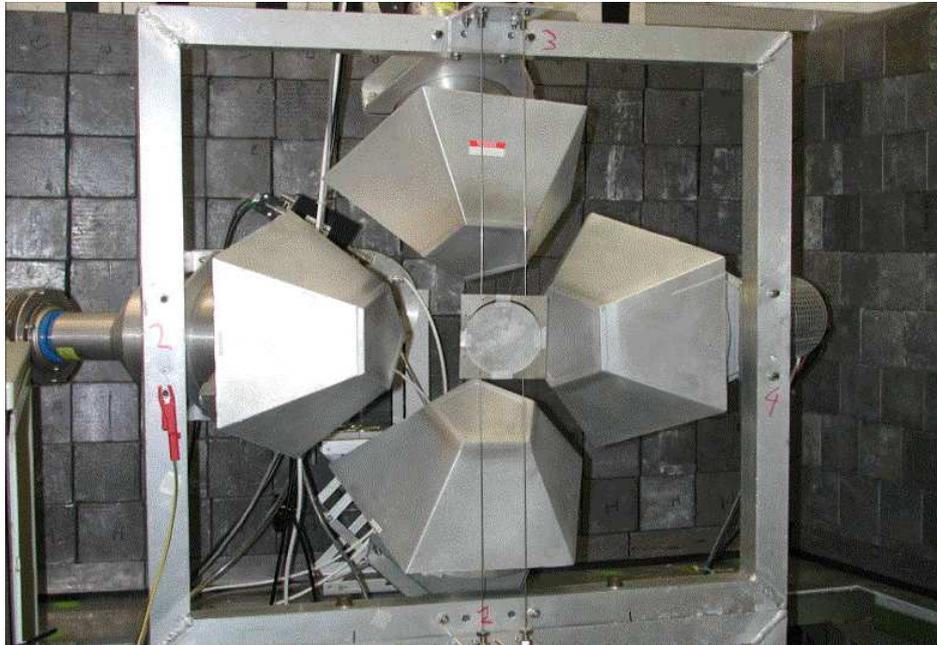
Figure 7.5: Picture of the 4 detectors setup.

Experimental responses for monoenergetic γ-ray calibration sources such as ^{137}Cs (661 keV) and ^{60}Co (1.17 and 1.33 MeV) were compared with the simulated ones. We also compared the measurement of γ-rays from the ^{232}Th decay chain to the simulation, where the gamma lines from ref. [94] were used with their respective emission probabilities. We observed a very good matching for these 3 cases in the whole energy region, which indicates that the absolute detection efficiency in the high energy is very well reproduced by the simulations. Figure 7.6 shows these comparisons between our simulations and the experimental measurements mentioned above.
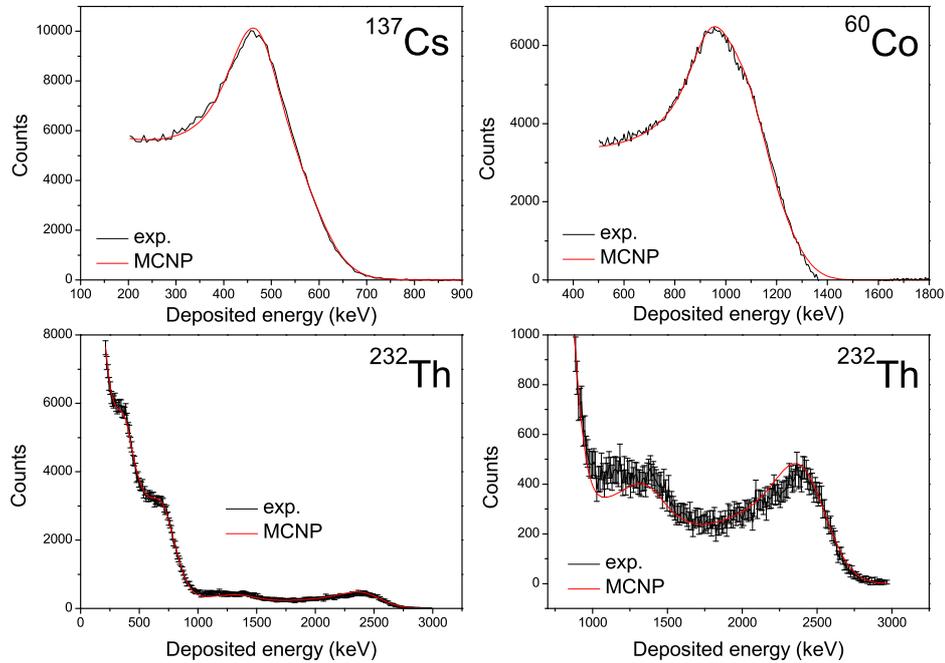
Figure 7.6: Experimental and simulated responses of the new C_6D_6 detector for monoenergetic γ-ray calibration sources.

7.3 Outlook

The upgrade of the capture cross section measurement setup running at GELINA is still ongoing. The new C_6D_6 detectors, based on a new truncated pyramid geometry, have been installed in a 4 detectors array to perform preliminary calibration test and measurements in order to compare their characteristics with Monte Carlo simulations. The simulations concerning total gamma efficiency and neutron sensitivity demonstrated the improved performance, with a neutron sensitivity identical to the one of the previous detectors, but a gamma efficiency 3 times higher. Moreover, a very good matching concerning the response to monoenergetic gamma calibration sources was achieved.

Meanwhile, the ^{241}Am(n,γ) capture measurement was achieved from October to December 2008 with a setup of two old C_6D_6 detectors with a cylindrical design. The data reduction and analysis, though not included in this work, will constitute the next important step in the analysis of the first americium resonances, giving more accurate values for the resonance parameters through a simultaneous

analysis of the transmission and capture measurements. Figure 7.7 illustrates an
example of the raw data we obtained for this capture measurement for one of the
C_6D_6 detectors.
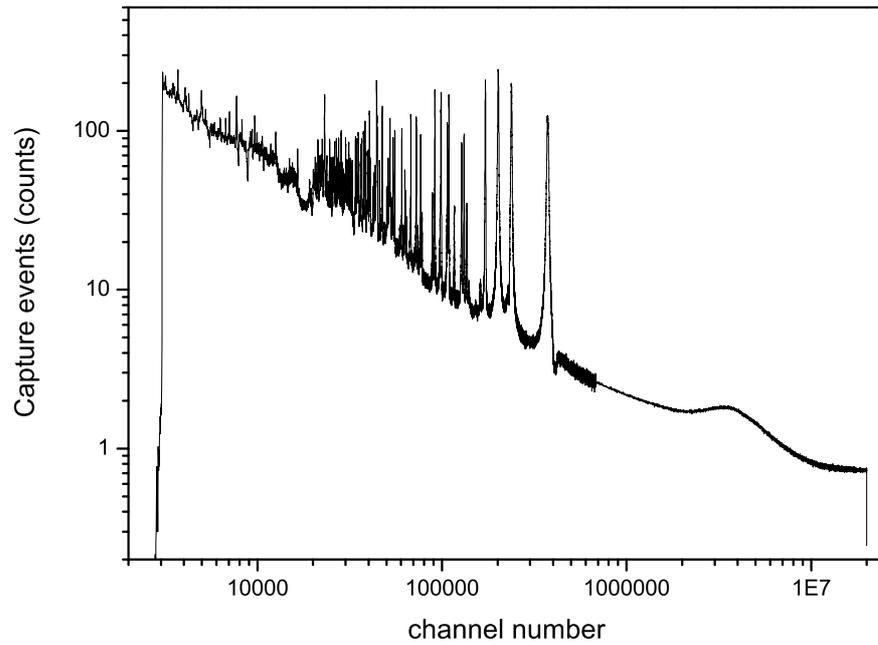
Figure 7.7: Raw ^{241}Am(n,γ) data from one of the C_6D_6 detectors.

Conclusion

In the context of the use of nuclear energy as a sustainable energy source, reducing the uncertainties on nuclear data is among the priority tasks to achieve in order to obtain trustable results in the study of future nuclear reactors. In particular, the accurate knowledge of the neutron reactions on ^{241}Am is of major importance concerning the study of innovative nuclear fuel with a significant quantity of minor actinides.

The scope of this work was to measure the ^{241}Am(n,2n)^{240}Am and ^{241}Am(n,tot) reaction cross sections with the highest accuracy. The measurements took place at the IRMM, where the two available neutron facilities, the electron linear accelerator GELINA and the Van de Graaff accelerator, were used as the neutron sources.

First, the ^{241}Am(n,2n)^{240}Am reaction cross section was measured at the Van de Graaff accelerator, which delivered monoenergetic neutrons ranging from the reaction threshold of 6.7 MeV to about 21 MeV. Such neutrons were produced using a deuterium gas target and a solid state Ti/T target, both hit by a deuteron beam produced by the Van de Graaff. Americium-alumina samples especially designed for this measurement were irradiated during four measurement sessions between February 2007 and March 2008.

The activation technique was employed to measure the (n,2n) reaction cross section. Following the irradiation, the induced activity was measured by standard gamma spectrometry, and the reaction cross section was deduced via the activation formula. The data correction for experimental effects mainly consisted in the estimation of the presence of lower energy neutrons in the beam during the irradiation, and the accurate estimation of the detection efficiency by Monte Carlo simulations concerning the gamma spectrometry. Up to 9 energy points were measured from the reaction threshold to 21 MeV, with 5 points in the energy range above 15 MeV, which constitute the first measurement for this reaction at these energies. A very good agreement was found both with already existing data below 15 MeV, and with neutron data libraries such as JEFF-3.1 and ENDF/B-VII.

A special effort was made for the estimation of the uncertainties and the correlations between our experimental points, with a detailed identification of the possible correlation sources. Our experimental results were used to parameterize new theoretical calculations of the (n,2n) cross section with the TALYS code. These results are accepted for publication in Phys. Rev. C.

The second measurement achieved in this work is the transmission measurement, which corresponds to the ^{241}Am(n,tot) reaction cross section measurement. For this latter, we used the neutron source GELINA, which delivers a white neutron flux the energy of which is determined via the Time-Of-Flight method. This transmission measurement took place at the 26.45 m cabin, with the irradiation of an americium-yttria sample during two sessions, in March 2007 and July 2008. The sample we used was also especially designed for this measurement, with an adequate thickness to get the best accuracy on the two first americium resonances at 0.3 and 0.57 eV.

The data reduction led to the determination of the experimental transmission factor, which is the ratio between measurement cycles with the sample in and out of the neutron beam. For this measurement, the data correction for experimental effects mainly consisted in the estimation of the background using the black resonance technique. A major upgrade of the whole data acquisition system occurred between the two transmission measurement sessions. The new list mode acquisition system gives more flexibility for the off-line data reduction, and its advantages are discussed in this work.

A preliminary analysis of the transmission data was done using the REFIT code for resonance shape analysis. These results tend to confirm the tendancy from the recent reevaluation of the cross section in the JEFF-3.1 library to a higher value at the resonances, but they have yet to be completed with an analysis of the capture reaction cross section. This measurement of the ^{241}Am(n,γ) reaction cross section was achieved following the transmission one from October 2007 to December 2008, but is not part of this work.

The characteristics of new C_6D_6 detectors for capture measurements was alo investigated by Monte carlo simulations using the MCNP5 code. The study focused on their gamma efficiency and their neutron sensitivity. The results were compared to the performances of the old detector cylindrical design, which has been used for the americium capture measurement.

Appendix A

Sample preparation method comparison
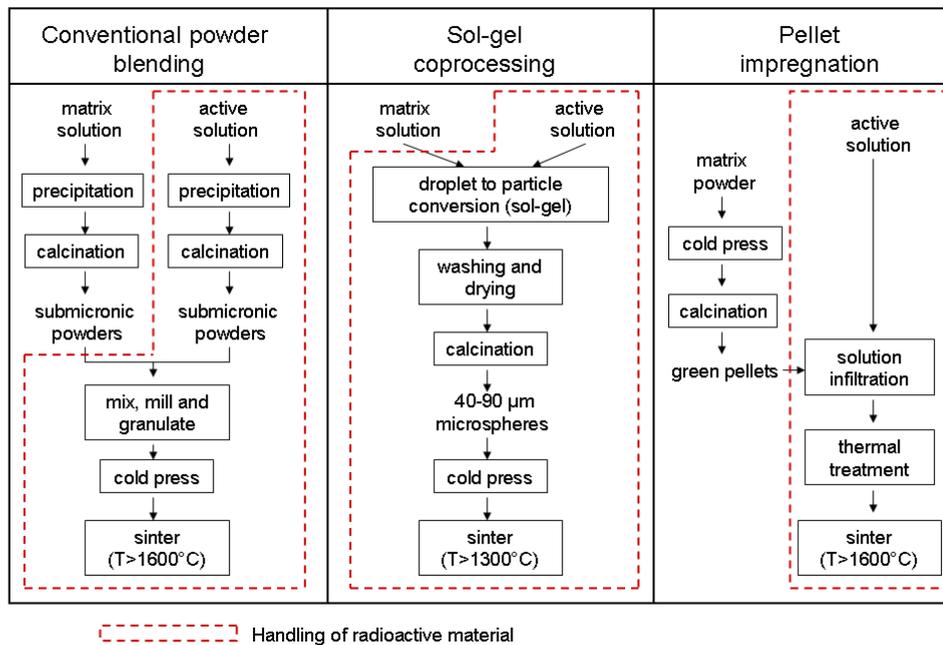
Figure A.1: Comparison between the conventional powder blending method and the sol-gel process for samples elaboration [95].

Appendix B

Calculation of the covariance matrices

Here will be presented the details of the calculation of the covariance matrices concerning the uncertainties linked to the terms of the activation formula (4.9) rewritten here:

$$\sigma_{\text{Am}} = \sigma_{\text{Al}} \frac{S_{\text{Am}}}{S_{\text{Al}}} \frac{\left[I \epsilon f_\Sigma f_r n \Phi_0 \right]_{\text{Al}}}{\left[I \epsilon f_\Sigma f_r n \Phi_0 \right]_{\text{Am}}} \cdot \prod_k \frac{C_{k,\text{Am}}}{C_{k,\text{Al}}}.$$

The result of our cross section measurement is a set of 9 cross sections at 9 corresponding independent energy points, together with a 9 x 9 total covariance matrix $\mathbf{C}$. The uncertainty of every term needed to calculate the cross section has a contribution $\mathbf{A}_i$ to this final covariance matrix. Since we have a product in eq. (4.13) it is convenient to divide the matrix elements of $\mathbf{C}$ by $\sigma_{Am,(i,j)}$ to obtain a matrix $\mathbf{C'}$ so we can use relative values.

$$\mathbf{C'} = \sum_i \mathbf{A'}_i \tag{B.1}$$

with $\mathbf{A'}_i$ the relative covariance matrices.

Uncorrelated uncertainties will contribute with a diagonal matrix, whereas correlated ones will contribute with a full matrix. Based on the correlation explanations from chapter 4, here will be expressed the covariance matrices corresponding to the non neglected uncertainty sources, which are repeated here:

fully correlated terms: I_{Am}, $(f_\Sigma f_r)_{\text{Am}}$, $\epsilon_{\text{Am}}/\epsilon_{\text{Al}}$.

partially correlated terms: σ_{Al}, n_{Am}.

uncorrelated terms: n_{Al}, S_{Am}, S_{Al}, $C_{\text{low,Am}}/C_{\text{low,Al}}$.

B.1   Uncorrelated uncertainties

Each covariance matrix will be in this case a diagonal matrix with the corresponding variances.

Covariance matrix for the counting statistics S_{Am} and S_{Al}

$$
\mathbf{A'_1} = \begin{pmatrix}
5^2 + 1^2 & & & & & & & & & 0 \\
& 4^2 + 1^2 & & & & & & & & \\
& & 2.5^2 + 1^2 & & & & & & & \\
& & & 2.1^2 + 1^2 & & & & & & \\
\vdots & & & & 1.5^2 + 1^2 & & & & & \vdots \\
& & & & & 1.3^2 + 0.7^2 & & & & \\
& & & & & & 6.3^2 + 2^2 & & & \\
& & & & & & & 1.4^2 + 1^2 & & \\
0 & & & & \cdots & & & & & 5.7^2 + 1.6^2
\end{pmatrix}
$$

Covariance matrix for the Al foils masses n_{Al}

$$
\mathbf{A'_2} = \begin{pmatrix}
0.1^2 & \cdots & 0 \\
\vdots & \ddots & \vdots \\
0 & \cdots & 0.1^2
\end{pmatrix}
$$

Covariance matrix for the ratio $C_{low,Am}/C_{low,Al}$

$$
\mathbf{A'_3} = \begin{pmatrix}
0 & & & & \cdots & & & 0 \\
& 0 & & & & & & \\
& & 0.3^2 & & & & & \\
& & & 0.3^2 & & & & \\
\vdots & & & & 0.3^2 & & & \vdots \\
& & & & & 0.3^2 & & \\
& & & & & & 1.3^2 & \\
& & & & & & & 1.4^2 \\
0 & & & & \cdots & & & 1.4^2
\end{pmatrix}
$$

B.2 Partially correlated uncertainties

Covariance matrix for σ_{Al}

The correlations between the energy points concerning the $^{27}Al(n,\alpha)^{24}Na$ reaction cross section σ_{Al} were taken from reference [46] together with the values themselves. Each element of the covariance matrix is calculated via the formula

$$Cov(x, y) = Corr(x, y).\ \sqrt{Var(x)}.\ \sqrt{Var(y)} \tag{B.2}$$

This gives the following covariance matrix:

$$
\mathbf{A'_4} = \begin{pmatrix}
1.9^2 & & & & & & & & \\
0.43 \times 1.9^2 & 1.9^2 & & & & \cdots & & & \\
0 & 0 & 1.6^2 & & & & & & \\
0 & 0 & 0.06 \times 1.6 \times 2 & 2^2 & & & & & \\
0 & 0 & 0.09 \times 1.6 \times 2 & 0.12 \times 2^2 & 2^2 & & & & \\
0 & 0 & 0.09 \times 1.6 \times 2.2 & 0.12 \times 2 \times 2.2 & 2 \times 2.2 & 2.2^2 & & & \\
0 & 0 & 0.11 \times 1.6 \times 3.1 & 0.11 \times 2 \times 3.1 & 0.4 \times 2 \times 3.1 & 0.4 \times 2.2 \times 3.1 & 3.1^2 & & \\
0 & 0 & 0.11 \times 1.6 \times 4.1 & 0.11 \times 2 \times 4.1 & 0.4 \times 2 \times 4.1 & 0.4 \times 2.2 \times 4.1 & 1 \times 3.1 \times 4.1 & 4.1^2 & \\
0 & 0 & 0.11 \times 1.6 \times 5.4 & 0.11 \times 2 \times 5.4 & 0.4 \times 2 \times 5.4 & 0.4 \times 2.2 \times 5.4 & 1 \times 3.1 \times 5.4 & 1 \times 4.1 \times 5.4 & 5.4^2
\end{pmatrix}
$$

Covariance matrix for the Am foils masses n_{Am}

The correlation between the energy points is 100% when the same sample was used, and 0% otherwise, which gives the following covariance matrix:

$$
\mathbf{A'_5} = \begin{pmatrix}
0.3^2 & & & & & \cdots & & & \\
0 & 0.3^2 & & & & & & & \\
0 & 0.3^2 & 0.3^2 & & & & & & \\
0 & 0.3^2 & 0.3^2 & 0.3^2 & & & & & \\
0 & 0 & 0 & 0 & 0.3^2 & & & \vdots & \\
0.3^2 & 0 & 0 & 0 & 0 & 0.3^2 & & & \\
0 & 0 & 0 & 0 & 0.3^2 & 0 & 0.3^2 & & \\
0 & 0 & 0 & 0 & 0 & 0 & 0 & 0.3^2 & \\
0.3^2 & 0 & 0 & 0 & 0 & 0.3^2 & 0 & 0 & 0.3^2
\end{pmatrix}
$$

B.3 Fully correlated uncertainties

In this section all correlations between the energy points are estimated to 100%, which gives the following covariance matrices:

Covariance matrix for I_{Am}

$$
\mathbf{A}_6' = \begin{pmatrix} 1.2^2 & \dots & 1.2^2 \\ \vdots & \ddots & \vdots \\ 1.2^2 & \dots & 1.2^2 \end{pmatrix}
$$

Covariance matrix for $(f_\Sigma f_r)_{Am}$

$$
\mathbf{A}_7' = \begin{pmatrix}
0.9^2 & & & & & & & & & \dots \\
0.9 \times 0.6 & 0.6^2 & & & & & & & \\
0.9 \times 0.4 & 0.6 \times 0.4 & 0.4^2 & & & & & & \\
0.9 \times 0.6 & 0.6^2 & 0.4 \times 0.6 & 0.6^2 & & & & & \\
0.9 \times 0.6 & 0.6^2 & 0.4 \times 0.6 & 0.6^2 & 0.6^2 & & & & & \vdots \\
0.9 \times 0.7 & 0.6 \times 0.7 & 0.4 \times 0.7 & 0.6 \times 0.7 & 0.6 \times 0.7 & 0.7^2 & & & \\
0.9 \times 0.6 & 0.6^2 & 0.4 \times 0.6 & 0.6^2 & 0.6^2 & 0.7 \times 0.6 & 0.6^2 & & \\
0.9 \times 0.6 & 0.6^2 & 0.4 \times 0.6 & 0.6^2 & 0.6^2 & 0.7 \times 0.6 & 0.6^2 & 0.6^2 & \\
0.9 \times 0.6 & 0.6^2 & 0.4 \times 0.6 & 0.6^2 & 0.6^2 & 0.7 \times 0.6 & 0.6^2 & 0.6^2 & 0.6^2
\end{pmatrix}
$$

Covariance matrix for $\epsilon_{Am}/\epsilon_{Al}$

$$
\mathbf{A}_8' = \begin{pmatrix} 3^2 & \dots & 3^2 \\ \vdots & \ddots & \vdots \\ 3^2 & \dots & 3^2 \end{pmatrix}
$$

B.4   Total covariance matrix

Summing all the covariance matrices detailed above gives the total covariance matrix:

$$
\mathbf{C} = \begin{pmatrix}
40.96 & & & & & \cdots & & & \\
12.53 & 31.51 & & & & & & & \\
10.8 & 10.77 & 20.61 & & & & & & \\
10.98 & 10.89 & 10.96 & 20.41 & & & & & \\
10.98 & 10.8 & 10.97 & 11.28 & 18.25 & & & & \vdots \\
11.16 & 10.86 & 11.04 & 11.39 & 15.26 & 18.15 & & & \\
10.98 & 10.8 & 11.23 & 11.48 & 13.37 & 13.59 & 65.9 & & \\
10.98 & 10.8 & 11.4 & 11.7 & 14.08 & 14.47 & 23.51 & 32.77 & \\
11.07 & 10.8 & 11.63 & 11.99 & 15.12 & 15.7 & 27.54 & 32.94 & 77.21
\end{pmatrix}
$$

and by applying equation (4.15), we get the final correlation matrix given in table 4.3 along with our results.

Bibliography

[1] Thorium Report Committee. *Thorium as an energy source - Opportunities for Norway*. 2008.

[2] IAEA (International Atomic Energy Agency), Power Reactor Information System (PRIS), http://www.iaea.org/programmes/a2/, 2009.

[3] Documentation CEA. *Mémento sur l'énergie - Edition 2006*.

[4] The Generation IV International Forum (GIF), http://www.gen-4.org/, 2009.

[5] P. Reuss. *Neutron Physics*. EDP Sciences, 2008.

[6] Documentation CEA. *ELECNUC Les Centrales Nucléaires dans le monde - Edition 2006*.

[7] Stéphanie Sala. *Réduction de la radiotoxicité des déchets nucléaires à vie longue: études théoriques et stratégiques de la transmutation des AM et des PF dans les réacteurs électronucléaires*, PhD Thesis. 1995.

[8] Physics and Safety of Transmutation Systems, A Status Report, OECD 2006, NEA No. 6090, 2006.

[9] http://www.developpement-durable.gouv.fr/energie/nucleair/f1e_nuc.htm.

[10] H. Takahashi and H. Rief. *Proceedings of Specialist's Meeting on Accelerator-Based Transmutation*, PSI Zurich, 1992.

[11] La R-D en France sur la séparation et la transmutation des radionucléides à vie longue, OECD 2006, NEA No. 6211, 2006.

[12] A.J. Koning, S. Hilaire, and M.C. Duijvestijn. Talys-1.0. In *Proceedings of the International Conference on Nuclear Data for Science and Technology - ND2007, Apr. 22 - 27, 2007, Nice, France*, volume 1, page 211. EDP Sciences, 2008.

[13] A. J. Koning and M. C. Duijvestijn. *New nuclear data evaluations for Ge isotopes.* Nucl. Instr. and Meth. in Phys. Res. B 248:197, 2006.

[14] http://www.nea.fr/html/dbdata/hprl.

[15] V. McLane. *EXFOR Basics, A Short Guide to the Nuclear Reaction Data Exchange Format.* Technical report, IAEA 2005, http://www-nds.iaea.org/exfor/exfor.htm.

[16] The JEFF-3.1 nuclear data library. Organisation for Economic Co-operation and Development, Nuclear Energy Agency, JEFF Report 21, NEA No.6190, isbn 92-64-02314-3, 2006.

[17] M. B. Chadwick, P. Obložinský, and M. Herman *et al.* ENDF/B-VII.0: Next generation evaluated nuclear data library for nuclear science and technology. *Nuclear Data Sheets*, 107:2931, 2006.

[18] K. Shibata, T. Kawano, T. Nakagawa, O. Iwamoto, J. Katakura, T. Fukahori, S. Chiba, A. Hasegawa, T. Murata, H. Matsunobu, T. Ohsawa, Y. Nakajima, T. Yoshida, A. Zukeran, M. Kawai, M. Baba, M. Ishikawa, T. Asami, T. Watanabe, Y. Watanabe, M. Igashira, N. Yamamuro, H. Kitazawa, N. Yamano, and H. Takano. Japanese Evaluated Nuclear Data Library Version 3 Revision-3: JENDL-3.3. *J. Nucl. Sci. Technol.*, 39:1125, 2002.

[19] A. I. Blokhin *et al.* Current status of Russian evaluated neutron data libraries. In *Conference on Nuclear Data for Science and Technology* - Tennessee, USA, page 695, 1994.

[20] M. Herman. *ENDF-6 Formats Manual*, Technical report BNL-NCS-44945-05-Rev, Brookhaven National Laboratory, 2005.

[21] A. A. Filatenkov and S. V. Chuvaev. Measurement of cross sections for the reactions ^{241}Am(n,2n) and ^{241}Am(n,3n). *Phys. At. Nucl.*, 63(9):1504–1510, 2000.

[22] R. W. Lougheed, W. Webster, M. N. Namboodiri, D. R. Nethaway, K. J. Moody, J. H. Landrum, R. W. Hoff, R. J. Dupzyk, J. H. McQuaid, R. Gunnink, and E. D. Watkins. ^{239}Pu and ^{241}Am (n,2n) cross-section measurements near En=14Mev. *Radiochim. Acta*, 90(12):833–843, May 2002.

[23] G. Perdikakis, C. T. Papadopoulos, R. Vlastou, A. Lagoyannis, A. Spyrou, M. Kokkoris, S. Galanopoulos, N. Patronis, D. Karamanis, C. Zarkadas, G. Kalyva, and S. Kossionides. Measurement of the ^{241}Am(n,2n) reaction cross section using the activation method. *Phys. Rev. C*, 73(2):067601, June 2006.

[24] A. P. Tonchev, C. T. Angell, M. Boswell, A. S. Crowell, B. Fallin, S. Hammond, C. R. Howell, A. Hutcheson, H. J. Karwowski, J. H. Kelley, R. S. Pedroni, and W. Tornow. Measurement of the ^{241}Am(n,2n) reaction cross section from 7.6 to 14.5 Mev. *Phys. Rev. C*, 77:054610, May 2008.

[25] Y. V. Adamchuck, V. F. Gerasimov, and B. V. Efimov. In *Proceedings of the first UN Conference on the Peaceful Uses of Atomic Energy, Geneva 1955*, page 216, 1955.

[26] T. S. Belanova, A. G. Kolesov, and V. M. Nikolaev. *Atom. Ener.*, 38:33, 1974.

[27] S. Kalebin, V. S. Artamonov, and R. N. Ivanov. *Atom. Ener.*, 40:373, 1976.

[28] G. G. Slaughter, J. A. Harvey, and R. C. Block. ORNL Report 3085, 1961.

[29] N. Bohr. Neutron capture and nuclear constitution. *Nature*, 137:344–348, 1936.

[30] J. Chadwick. *Nature*, 129:312, 1932.

[31] F. H. Fröhner. *Evaluation and Analysis of Nuclear Resonance Data*. NEA, JEFF Report 18, 2000.

[32] C. W. Reich and M. S. Moore. *Physical Review*, 111:929, 1958.

[33] G. Breit and E. Wigner. Capture of slow neutron. *Physical Review*, 49:519, 1936.

[34] W. Solbrig. *Am. Journal of Physics*, 29:257, 1961.

[35] D. G. Naberejnev, C. Mounier, and R. Sanchez. The influence of crystalline binding on resonant absorption and reaction rates. *Nucl. Sci. and Eng.*, 131:222, 1999.

[36] V. Gressier, D. G. Naberejnev, and C. Mounier. The impact of the harmonic crystal model on the neutron resonance parameters of ^{237}Np. *Annals of Nuclear Energy*, 27:1115, 2000.

[37] W. E. Lamb. Capture of neutrons by atoms in a crystal. *Physical Review*, 55:190, 1939.

[38] B. Singh and E. Browne. *Nuclear Data Sheets*, 109:2439, 2008.

[39] M. S. Basunia. Nuclear data sheets for A = 237. 107:2323, 2006.

[40] C. Nästren, M. Holzhäuser, A. Fernandez, C. Brossard, F. Wastin, H. Ottmar, and J. Somers. *Fabrication of Am samples for neutron cross section measurements at JRC-IRMM Geel*, Tech. Rep. JRC-ITU-TN-2006/34, European Commission, 2006.

[41] G. Lövestam. EnergySet, EC-JRC-IRMM, http://irmm.jrc.ec.europa.eu, 2004.

[42] H. Liskien and A. Paulsen. Neutron production cross sections and energies for the reactions T(p,n)^{3}He, D(d,n)^{3}He and T(d,n)^{4}He. *Nucl. Data Tables*, 11:569–619, 1973.

[43] H. H. Andersen and J. F. Ziegler. Hydrogen stopping powers and ranges in all elements. *Pergamon Press, New York*, 1977.

[44] D. Schlegel. Monte Carlo code TARGET, PTB-6.14-98-1, Braunschweig, April 1998, private communication, 1998.

[45] A. B. Smith. Argonne National Laboratory, Report No ANL/NDM-115, http://www.td.anl.gov/reports, Argonne, 1990.

[46] M. Wagner, H. Vonach, A. Pavlik, B. Strohmaier, S. Tagesen, and J. Martinez-Rico. Evaluation of cross sections of 14 important neutron-dosimetry reactions. *Physics Data*, 13(5):34, 1990.

[47] V. McLane. Evaluated Nuclear Data File, Section B, Version VI (ENDF/B-VI), National Nuclear Data Center, Brookhaven National Laboratory, available online at http://www.nndc.bnl.gov/nndc/endf.

[48] R. B. Firestone. Nuclear data sheets for A = 24. 108:2319, 2007.

[49] P. M. Endt. Supplement to energy levels of A = 21-44 nuclei (vii). *Nucl. Phys. A*, 633:1, 1998.

[50] H. Junde. Nuclear data sheets for A = 56. 86:315, 1999.

[51] J. Blachot. Nuclear data sheets for A = 115. 104:967, 2005.

[52] C. M. Baglin. Nuclear data sheets for A = 92. 91:423, 2000.

[53] M. R. Bhat. Nuclear data sheets for A = 58. 80:789, 1997.

[54] G. Audi, A. H. Wapstra, C. Thibault, J. Blachot, and O. Bersillon. The Ame2003 Atomic Mass Evaluation. 729:337, 2003.

[55] X-5 Monte Carlo Team, *MCNP - A general Monte Carlo N-Particle Transport Code*, Version 5 (LANL, New Mexico, April 24 2003).

[56] B. Jäckel, W. Westmaier, and P. Patzelt. On the photopeak efficiency of germanium gamma-ray detectors. *Nucl. Instr. Meth. in Phys. Res.*, A261:543, 1987.

[57] A. Fessler, A. J. M. Plompen, D. L. Smith, J. W. Meadows, and Y. Ikeda. *Nucl. Sci. Eng.*, 134:171–200, 2000.

[58] P. Reimer, M. Hult, A. J. M. Plompen, P. N. Johnston, V. Avrigeanu, and S. M. Qaim. *Measurement of the $^{nat}Mo(n,x)^{94}Nb$ cross section using ultra low-level γ-ray spectrometry at HADES.* 705:265–278, 2002.

[59] P. Reimer, V. Avrigeanu, S. V. Chuvaev, A. A. Filatenkov, T. Glodariu, A. Koning, A. J. M. Plompen, S. M. Qaim, D. L. Smith, and H. Weigmann. *Reaction mechanisms of fast neutrons on stable Mo isotopes below 21 MeV.* 71:044617, 2005.

[60] P. Reimer, A. J. Koning, A. J. M. Plompen, S. M. Qaim, and S. Sudár. *Neutron induced reaction cross sections for the radioactive target nucleus ^{99}Tc.* Nucl. Phys. A 815:1, 2009.

[61] MCNPX version 2.5.f: Monte Carlo N-Particle transport code system for multiparticle and high energy applications.

[62] http://www.srim.org/.

[63] H. Klein, H. J. Brede, and B. R. L. Siebert. Energy and angle straggling effects in a D(d,n)^{3}He neutron source using a gas target. *Nucl. Instr. Meth. in Phys. Res.*, 193:635–644, 1982.

[64] D. L. Smith, A. J. M. Plompen, and V. Semkova. *Correction for low energy neutrons by spectral indexing.* Organisation for Economic Co-operation and Development, Nuclear Energy Agency, International Evaluation Co-operation, Volume-19, NEA/WPEC-19, isbn 92-64-01070-X, www.nea.fr/html/science/wpec/volume19/volume19.pdf, 2005.

[65] S. Cabral, G. Börker, H. Klein, and W. Mannhart. *Neutron Production from the Deuteron Breakup Reaction on Deuterium.* 106:308–317, 1990.

[66] K. Debertin and R. G. Helmer. *Gamma- and X-Ray Spectrometry with Semiconductor Detectors*, North Holland Publishing Company, 1988.

[67] Evaluated Nuclear Structure Data File (ENSDF), National Nuclear Data Center, Brookhaven National Laboratory, 1998.

[68] P. Romain and J.-P. Delaroche. A dispersive coupled channels analysis of nucleon scattering from ^{181}Ta and ^{182,184,186}W up to 200 Mev. In *Proceedings of the NEA Specialists' Meeting on the Nucleon-Nucleus Optical Model up to 200 MeV* - Bruyères-le-Châtel (1996), http//db.nea.fr/html/science/om200/, page 167. OECD, Paris, 1997.

[69] B. Morillon and P. Romain. *Phys. Rev. C*, 70:014601, 2004.

[70] M.J. López Jiménez, B. Morillon, and P. Romain. *Ann. Nucl. Energy*, 32:195, 2005.

[71] J.W.T. Dabbs. Neutron cross section measurements at ORELA. In *Proceedings of the International Conference on nuclear cross section for technology, Knoxville, Tennessee*, 1979.

[72] M. Flaska, A. Borella, D. Lathouwers, L. C. Mihailescu, W. Mondelaers, A. J. M. Plompen, H. van Dam, and T. H. J. J. van der Hagen. Modeling of the GELINA neutron target using coupled electron-photon-neutron transport with the MCNP4c3 code. *Nucl. Instr. and Meth. in Phys. Res. A*, 531:392–406, 2004.

[73] G. Noguère. *Mesures et analyses des sections efficaces neutroniques totales et de captures radiatives des iodes 127 et 129 de 0.5 eV à 100 keV*, PhD Thesis, 2003.

[74] S. de Jonge. *Fast Time Digitizer Type 8514 A*, IRMM Internal Report GE/DE/R/24/87, IRMM, Geel, 1987.

[75] J. Gonzales, C. Bastian, S. de Jonge, and K. Hofmans. *MMPM, Hardware description and user guide*, IRMM Internal Report GE/R/INF/06/97, IRMM, Geel, 1997.

[76] C. Bastian. AGS, a set of unix commands for neutron data reduction. In *Proceedings of the International Conference on Neutron Research and Industry, Crete, Greece, 1996*, volume 2867, page 611. Ed. G. Vourvopoulos, SPIE - The International Society for Optical Engineering, 1997.

[77] M. C. Moxon, T. C. Ware, and C. J. Dean. *REFIT-2007, A Least-Square Fitting Program for Resonance Analysis of Neutron Transmission, Capture, Fission and Scattering Data*, UKNSF(2007)P216, 2007.

[78] http://root.cern.ch/root/.

[79] D. J. Hughes. A method for rapid analysis of neutron resonances. *Journ. Nucl. Energy*, 1:237, 1955.

[80] J. E. Lynn and E. R. Rae. The analysis of neutron spectrometer resonance data. *Journ. Nucl. Energy*, 4:418–444, 1957.

[81] F. H. Fröhner, E. Haddad, W. M. Lopez, and S. J. Friesenhahn. Accuracy of resonance parameters from combined area and self-indication measurements. In *Proceedings of the International Conference on Neutron Cross Section Technology, Washington D.C., 22-24 March 1966*, pages 55–66, 1966.

[82] N. M. Larson. *Updated Users' Guide for SAMMY: Multilevel R-Matrix Fits to Neutron Data Using Bayes' Equation*, ORNL/TM-9179/R6 ENDF-364, 2003.

[83] D. G. Naberejnev. *Etude de l'influence des liaisons chimiques sur l'absorption et la diffusion de neutrons aux énergies de résonance*, ISSN 0429-3460, CEA-N-2840, 1999.

[84] J. D. Gale and A. L. Rohl. The general utility lattice program. *Mol. Simul.*, 29:291, 2003.

[85] K. Kurosaki, M. Imamura, I. Sato, T. Namekawa, M. Uno, and S. Yamanaka. Molecular dynamics studies of minor actinide dioxides. *Journal of Nucl. Sci. and Tech.*, 41:827–831, 2004.

[86] G. V. Lewis and C. R. A. Catlow. Potential models for ionic oxides. *J. Phys. C: Solid State Phys.*, 18:1149–1161, 1985.

[87] V. Gressier. *Nouvelle détermination expérimentale des paramètres de résonances neutroniques de ^{237}Np en-dessous de 500 eV*, PhD Thesis, 1999.

[88] O. Bouland and D. Bernard. Revised evaluation of the ^{241}Am isotope. In *JEFF Meeting, Paris, 2-4 May 2005, JEFDOC-1086*, 2005.

[89] R. L. Macklin and J. H. Gibbons. *Phys. Rev.*, 159:1007–1012, 1967.

[90] A. Borella, G. Aerts, F. Gunsing, M. Moxon, P. Schillebeeckx, and R. Wynants. The use of C_6D_6 detectors for neutron induced capture cross-section measurements in the resonance region. *Nucl. Instr. And Meth.*, 577:626–640, 2007.

[91] P. E. Koehler *et al. Phys. Rev. C*, 62:055803–1–15, 2000.

[92] R. Plag *et al. Nucl. Instr. And Meth. A*, 496:425–436, 2003.

[93] M. Weyrauch *et al. Nucl. Instr. And Meth. A*, 405:442–454, 1998.

[94] W. J. Lin and G. Harbottle. *J. of Radioanalytical and Nucl. Chemistry*, 157-2:367–372, 1992.

[95] D. Haas, J. Somers, A. Renard, and A. La Fuente. Feasibility of the fabrication of americium targets. In *Actinide and Fission Product Partitioning and Transmutation, Proceedings of the Fifth International Information Exchange Meeting, Mol, Belgium, 25-27 Nov. 1998*, page 197. OECD, Paris, 1998.